Università degli Studi di Padova
Dipartimento di Fisica ed Astronomia "G. Galilei"

Tesi di Laurea Magistrale in Fisica

Growth and characterization of nanostructured Au doped Zinc oxide thin films by RF Magnetron Co-Sputtering

Laureando:
Davide Stefani

Relatore:
Prof. Giovanni Mattei

Correlatore:
Prof. Leonardo Soriano de Arpe

Controrelatore:
Dr. Andrea Sanson

Anno Accademico 2014/2015

Contents

Introduction

Transition metal oxides have attained much attention in the last years due to their outstanding properties that make them attractive not only for fundamental studies, but also for a wide range of applications in nanotechnology.

The potential for flexible, lightweight, mechanically robust electronics devices on plastic substrates has motivated considerable research on new materials and improved processes for fabricating thin film transistors (TFTs). However, plastic substrates, typically limit device processing to less than 150 °C. [1] One consequence is that electronics based on Si, even amorphous Si, may be incompatible with plastic substrates. This, in part, has fueled a broad interest in organic semiconductors as an inexpensive, low-temperature class of alternative materials, especially for thin film transistors. [2] [3] However, the electronic properties of most organic semiconductors are inferior to those of amorphous Si. Further, organic materials frequently degrade in normal atmospheric conditions, requiring protection strategies. [4] In contrast, a stable inorganic semiconductor compatible with temperature sensitive substrates, and with electronic properties equivalent to amorphous Si would enable electronics on a variety of flexible substrates. Recent researches have hinted that a ZnO semiconductor can meet those requirements [5] and that a very effective way to synthetize a ZnO TFT is by radio frequency magnetron sputtering. [6]

An important class of metal oxides is transparent conducting oxides, which possess two diametrically opposite characteristics: high optical transparency in visible region and high DC electrical conductivity. A well known example has been the tin doped indium oxide (ITO) that is being widely used as transparent electrode in optoelectronic devices and displays [7]. However, the escalating cost of indium has lead to the search for low cost alternatives. Currently ZnO has been considered as a viable alternative. ZnO has a band gap of about 3.37 eV and exhibits optical transparency comparable to that of ITO in the visible region. Oxygen deficient off-stoichiometric ZnO shows n-type conductivity, which can be enhanced by doping, mainly with aluminium. [8] Aluminium doped ZnO has been used as the top transparent electrode in absorber based thin film solar cells. [9]

Some optoelectronic applications of ZnO overlap with that of GaN, another wide-gap semiconductor ($E_g \sim 3.4$ eV at 300 K) which is widely used for production of green, blue-ultraviolet, and white light-emitting devices. However, ZnO has some advantages over GaN among which are the availability of fairly high-quality ZnO bulk single crystals and a large exciton binding energy (∼60 meV). [10] ZnO also has much simpler crystal-growth

technology, resulting in a potentially lower cost for ZnO-based devices.

In this project we aim to replicate some of the results obtained in previous researches and present a preliminary attempt to create transparent and conductive thin films using ZnO doped with gold nano particles.

The first part was dedicated to tuning the equipment and optimising the growth procedure in order to synthetize ZnO films of about 200 nm thickness. We then investigated how the percentages of O_2 and Ar present in the chamber during growth influenced the properties of ZnO films. Previous works with metal oxides [11] [12] [13] [14] showed an increase in conductivity with higher quantity of oxygen, therefore we checked if zinc oxide followed that trend or not.

For the second part we installed a second magnetron which was used to dope the ZnO films with gold nanoparticles. This kind of work (RF co-sputtering) required some adaptations to our equipment. Two different series were made, the first one by manually opening and closing the Au magnetron shutter in order to regulate the gold flux to the samples, the second one by using pulsed magnetron plasma to automatically turn on/off the Au flux.

It should be noted that post-deposition annealing of RF magnetron sputtered ZnO films has been found to relieve the stress, improve the optical qualities [15] [16] [17] [18] as well as the crystalline properties and reduce their surface roughness [19] [20].

In the first chapter we will introduce the physics involved in the experiment, the second will be dedicated to the equipment and analysis techniques utilised, in the third we will present the results and their discussion.

Chapter 1

The Physics of the Experiment

1.1 General Properties of ZnO

The crystal structures observed in ZnO are wurtzite, zinc blende, and rocksalt (Fig.1.1). Under ambient conditions, the thermodynamically stable phase is wurtzite. The zinc blende ZnO structure can be stabilized only by growth on cubic substrates, and the rocksalt or Rochelle salt (NaCl) structure may be obtained at relatively high pressures. The *wurtzite* structure has a hexagonal unit cell with two lattice parameters a and c in the ratio of $c/a = \sqrt{8/3} = 1.633$ [21].

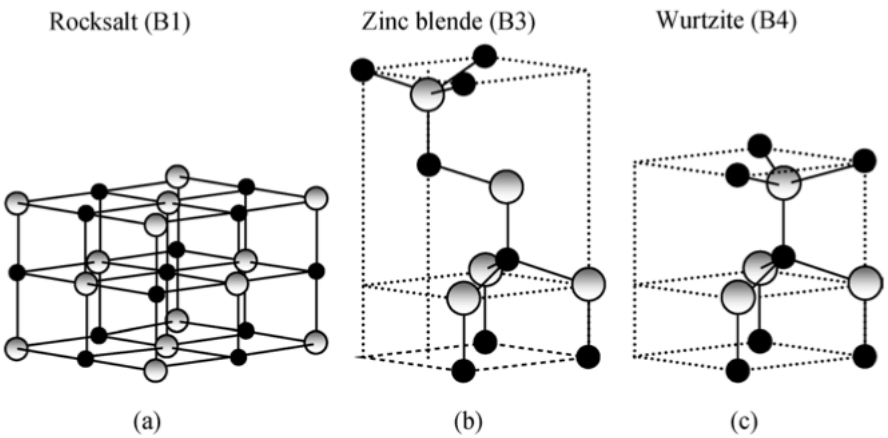

Figure 1.1: Stick-and-ball representation of ZnO crystal structures: (a) cubic rocksalt, (b) cubic zinc blende, and (c) hexagonal wurtzite. Shaded grey and black spheres denote Zn and O atoms, respectively.

ZnO is a direct and large band gap (3.37 eV), n-type semiconductor with a high melting temperature. Advantages associated with a large band gap include higher breakdown voltages, ability to sustain large electric fields, lower noise generation, and high-temperature and high-power operation. It is particularly attractive because good quality films with moderate Hall mobilities (> 1 cm^2/V s) can be made at room temperature and, thus, there is good compatibility with plastic or flexible substrate materials [22]. Moreover,

since a ZnO semiconductor is transparent in the visible and, therefore, also less light sensitive, TFTs based on ZnO may have particular advantage in electronic drivers for displays and high efficiency solar cells.

Hall mobility characterizes how quickly an electron (or a hole, if that's the case for the semiconductor being investigated) can move through a metal or semiconductor, when pulled by an electric field. Conductivity is proportional to the product of mobility and carrier concentration, so the same conductivity could come from a small number of electrons with high mobility, or a large number of electrons with a small mobility. For metals, it would not typically matter which of these is the case, since most metal electrical behaviour depends on conductivity alone. For semiconductors, on the other hand, the behaviour of transistors and other devices can be very different depending on whether there are many electrons with low mobility or few electrons with high mobility. Therefore mobility is a very important parameter for semiconductor materials. Almost always, higher mobility leads to better device performance, provided other characteristics are comparable. Semiconductor mobility depends on the impurity concentrations (including donor and acceptor concentrations), defect concentration, temperature, and electron and hole concentrations.

The large exciton[1] binding energy of ∼60 meV paves the way for an intense near-band-edge excitonic emission at room and higher temperatures, because this value is 2.4 times that of the room-temperature thermal energy ($k_B T$ = 26 meV) [9]. This could lead to efficient room-temperature exciton-based emitters, and sharp transitions facilitating very low threshold semiconductor lasers. However, a prerequisite is to prepare p-type zinc oxide, which is normally n-type. There have been many recent reports that p-type ZnO can be obtained by doping with nitrogen, phosphorous or arsenic [23] [24] [25] [26], which would enable a still broader class of electronic devices based on ZnO [27] [28]. A severe problem is that p-type conductivity is often non persistent, vanishing within days or weeks [29].

1.2 Sputtering

Magnetron sputtering has been a powerful technique for industrial applications in the last decades. Much effort has been done to improve this technique from the very basic Direct Current (DC) diode to the last pulsing discharge magnetrons [30] and Highly Ionized Power Impulse Magnetron Sputtering (HIPIMS) [31].

As compared to sol-gel and chemical-vapor deposition [32] [33] [34] [35], magnetron sputtering was preferred because of its low cost, simplicity, and low operating temperature [36] [37]. Other growth techniques which allow a fine control over the deposition procedure are molecular-beam epitaxy (MBE), pulsed-laser deposition (PLD), metal-organic

[1] An exciton is a bound state of an electron and a hole. An exciton can form when a photon is absorbed by a semiconductor, this excites an electron from the valence band into the conduction band. In turn, this leaves behind a positively-charged electron hole which provides a stabilizing energy for the electron. Excitons are the main mechanism for light emission in semiconductors at low temperature (when the characteristic thermal energy $k_B T$ is less than the exciton binding energy), replacing the free electron-hole recombination at higher temperatures.

chemical-vapor deposition (MOCVD), and hydride or halide vapor-phase epitaxy (HVPE).

1.2.1 RF Magnetron Sputtering

The sputtering process is the physical vaporization of atoms from a surface (called target) through by a momentum transfer from impinging particles (ionized atoms) with high kinetic energy. These impinging ions are directed towards the surface target material due to a high electric field generated by the potential difference between the cathode and anode of the magnetron. The atoms ejected (or *sputtered*) from the target surface have a kinetic energy of ∼10 eV, which is higher than those thermally evaporated (as in a Knudsen evaporation cell, where the energy is between 3 and 5 eV) [38], but lower than in HIPIMS (∼ 50 eV) [31] and much lower than in cathodic arc (20÷200 eV) and Pulsed Laser Deposition (PLD) which are extremely energetic ($10 \div 10^4$ eV). The sputtered atoms are neutral in charge and deposit on the substrate located at a certain distance from the target surface forming the coating.

The bombarding atoms form a plasma of low density (dependent on the geometry of the magnetron) and because this is a purely transfer momentum process, the higher the mass and kinetic energy of the impinging atoms, the higher the sputter yield.

The sputtering yield is the ratio of the number of atoms ejected to the number of incident bombarding particles and depends on the chemical bonding of the target atoms and the energy transferred by collision. [38]

$$\text{Sputtering Yield} = \frac{\text{Ejected atoms}}{\text{Incoming ions}}$$

Many models have been proposed to calculate the sputtering yield, but they will not be treated in this work due to their complexity and their theoretical nature.

For each material there is an energy threshold below which it is not possible to sputter any atom from the target.

The sputtering is driven by a plasma generated by the voltage difference between two electrodes in the presence of a low-pressure gas. A high enough DC voltage between two electrodes in a low-pressure gas can initiate a discharge by ionizing the gas atoms forming a plasma. The relation between voltage, gas density (or pressure) and electrodes distance is governed by Paschen's Law. [39] Within the plasma there are neutral and charged species (positive and negative) and their populations define the degree of ionization. At a certain voltage range, between 10^2-10^3 volts, the discharge becomes self-sustaining. If the electric field is strong enough, the free electrons travelling towards the anode gain sufficient energy to liberate a further electron when they next collide with another atom or molecule. The same then happens to the freed electrons, creating a chain reaction of electron generation; it depends on the free electrons gaining sufficient energy between collisions to sustain the avalanche. If the voltage is fixed instead, the minimum requirement is shifted to the pressure; i.e. if the pressure is below a minimum value, the discharge avalanche does not take place and the plasma cannot be initiated.

The magnetrons employed for the sputtering utilize strong electric and magnetic fields to confine charged plasma particles close to the surface of the sputter target. The secondary electrons produced in the sputtering process are trapped in these field lines by lengthening their path, greatly increasing the probability of occurrence of ionizing collisions with gaseous neutrals near the target surface. This creates a region of higher plasma density around the target. Ions created as a result of these collisions lead to a higher deposition rate, while secondary electrons help sustain the plasma at lower pressures. The sputtered atoms are neutrally charged and so are unaffected by the magnetic trap.

In the flux of sputtered particles, as a rule not only atoms, but also clusters are found. This applies in particular to the neutral species emitted. Thus in many experiments performed by keV bombardment of metals, a fraction on some 10% of the sputtered atoms are bound as dimers. The cluster abundance distribution follows the power-law decay:

$$Y_n \propto n^{-\alpha} \tag{1.1}$$

where n is the number of atoms in a cluster and the exponent α decreases with increasing sputtering yield [40]. Experimentally, α is found to be larger than 2. A transparent theoretical argument for the origin of this law is still missing. There are, however, phenomenological models that predict the power-law cluster-abundance distribution 1.1; these models are the shock-wave model ($\alpha = 2$) and the thermodynamic-equilibrium model ($\alpha = 7/3$) [41]. It has been found that large clusters are emitted late after the ions impact and originate from 'hot spots', i.e. surface regions with a temperature around or above the melting temperature of the sputtered material. A clear correlation of large cluster emission with the individual sputtering yield could be formed such that ion impact events leading to abundant sputtering give also rise to abundant cluster formation [42].

When working with low-conductivity sputtering targets a DC magnetron is not efficient because the target surface will charge positively. If the target surface potential is negative, ion impingement may initially cause sputtering but since the secondary-electron emission coefficient is less than unity, a positive surface charge develops. Ion bombardment is discouraged and then ceases, which prevents sputtering. Moreover, the charge buildup, creates the possibility of a local dielectric break-down of the insulating films, generating an arc over the target surface (unipolar arcs) as well as to neighboring hardware (bipolar arcs). Arcing prevents the stable operation of DC power supplies, particularly during the reactive sputtering of dielectric films. This problem is solved with the use of radio frequency magnetrons (RF). Typically, square or sinusoidal voltage pulses are applied to the target at the radio frequencies, where pulse magnitude, polarity, width, and off-time can all be varied. During the positive portion of the cycle, electrons are drawn to the target in order to neutralize the positive charge buildup that leads to arcs. After discharging, the target is again negatively powered and sputtered until it is time to discharge it again, etc. The reserved frequency for magnetron devices is 13.56 MHz [39].

In order to direct the positive ions to the target, this must be negatively charged, which is achieved due to the fact that electrons are much mobile than ions, following rapidly the

changing electric field. As a consequence it exists an asymmetry of the discharge current-voltage curve: the positive electrode draws more current through electrons than negative isolated electrodes draw through ions. When AC is applied to the cathode (target material) a large amount of current is drawn during the positive cycle due to electrons while in the negative cycle a small amount of charge flows. The average net current is non-zero but since the target is an insulator no charge can be transferred, therefore the target is biased with a negative charge [39].

The sputtering gas is formed commonly by noble gases such as argon due to its large mass (but heavier noble gases could be used), chemically inert behaviour, low cost and low ionization energy. Other gases can be used for sputtering: oxygen, nitrogen, methane, or hydrogen sulfide are usually selected in order to deposit oxides, nitrides or carbides. In these cases the process is named *reactive sputtering*. The compound can be formed on the target surface, in-flight or on the substrate depending on the process parameters.

However, sputtering is an inefficient process: more than 90% of the transferred energy of the bombarding atoms is released in form of heat [38], thus the refrigeration of the magnetron head where the target is located is essential, especially when the target is a ceramic oxide with a high thermal expansion coefficient and low thermal conductivity. In the case of a laboratory magnetron sputtering with water cooling, the target temperature remains below 300°C [30].

By independently powering two (or more) magnetrons of different composition simultaneously, the production of films with assorted material mixtures and graded compositions is possible. This was done in our experiment by implementing two magnetrons with a zinc oxide and a gold target respectively.

1.2.2 Thornton model

An essential feature of vapor deposited thin films is that they are formed from a flux that approaches the substrate from a limited set of directions. Consequently, the metallurgical grains tend to be columnar, defined by voided open boundaries, which is superimposed on a microstructure which may be polycrystalline (defined by metallurgical grain boundaries) or amorphous. The voided growth structure is clearly undesirable for most applications. Its occurrence is a fundamental consequence of atomic shadowing acting in concert with the low adatom mobilities that characterize low T/T_m (homologous temperature, i.e. substrate temperature T, relative to coating material melting point T_m) deposition, and its formation can be enhanced by the surface irregularities which are common to microcircuit fabrication [43].

It is useful to envision coating growth as proceeding in three general steps as indicated schematically in Fig. 1.2 The first step involves the transport of the coating species to the substrate. The second step involves the adsorption of these species onto the surface of the substrate or growing coating, their diffusion over this surface, and finally their incorporation into the coating or their removal from the surface by evaporation or sputtering. The third step involves movement of the coating atoms to their final position within the coating

by processes such as bulk diffusion. In the case of sputter deposition, the transport step is controlled by parameters such as the apparatus geometry and working gas pressure, while the diffusion steps are controlled largely by the substrate temperature, but may be significantly influenced by energetic particle bombardment [43].

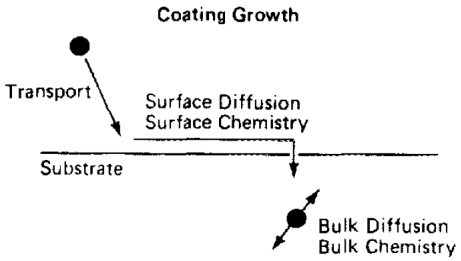

Figure 1.2: Schematic illustrations showing the steps involved in the condensation of a vapor during film growth.

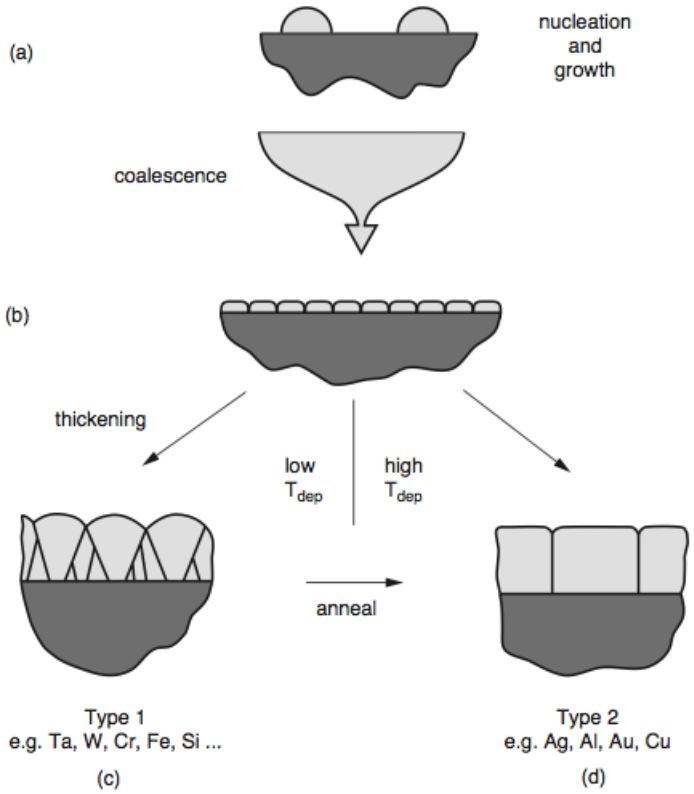

Figure 1.3: Overview of grain structure evolution during deposition of polycrystalline thin films.

Fig.1.3 outlines, in very simple form, the fundamental process through which the grain structure of polycrystalline thin films develops during film formation. Polycrystalline films are usually formed through the nucleation of isolated crystals on a substrate surface. Once formed, nuclei grow on the substrate surface and in the external phase, forming the first crystals. Lateral growth leads to impingement and coalescence of crystals, resulting in the

formation of grain boundaries and defining at least the initial grain-structure characteristics of the newly formed film. The process of coalescence of islands is driven by an elastic distortion of the islands surface which eliminate their contact boundary lowering the surface energy [44].

This nucleation, growth, impingement, and coalescence process is schematically illustrated in cross-sectional sketches in Fig.1.3a and b and Fig.1.4.

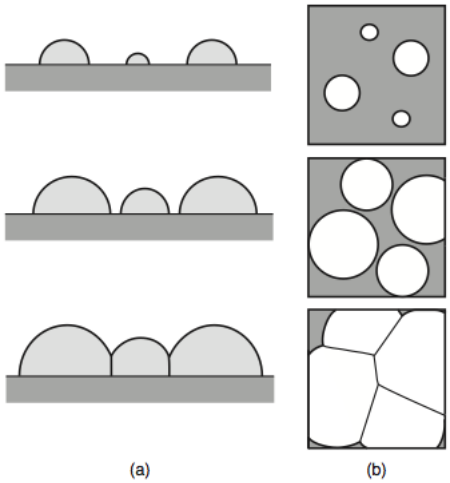

Figure 1.4: Nucleation, growth, and coalescence to form a continuous thin film

Grain structure evolution during thickening occurs in two fundamentally different ways, as schematically illustrated in Fig.1.3c, d. If the grain boundaries formed through island impingement are immobile, the grain structure resulting from the nucleation, growth, and coalescence processes is retained at the base of the film. Usually, subsequent thickening occurs through epitaxial growth on these grains and results in films with high-aspect-ratio columnar grains.

If grain boundaries are mobile during deposition, Type 2 thickening (Fig.1.3b-d) occurs and the grain size of the film increases as the film thickens. Adatoms join the grain on which they are deposited but may become incorporated in neighbouring grains through motion of boundaries in the bulk or volume of the film. The grain aspect ratios in the as-deposited films have an average value of order 1, i.e. the in-plane grain size tends to be approximately the same as and scale with the film thickness [45].

At very low temperatures at which surface self-diffusivities for adatoms are very low, surface topography present at coalescence can become accentuated during thickening as atoms arrive and remain at their arrival site. It has been shown that roughness on the surface of even thickening amorphous films can become accentuated under conditions of severely limited adatom mobility, and this stabilized roughness can result in a columnar growth mode and columnar structures [46]. This phenomenon is known as kinetic roughening.

When adatoms arrive at normal incidence to the film's surface, perturbations are stabilized and columnar structures develop in which the columns meet at regions of low density

relative to the density in the interiors of the columns. This can also lead to void formation at the column walls. When adatom mobility is finite, the scale of the minimum-sized perturbations that are stabilized increases [45]. If adatoms arrive with a range of angles off the normal to the film surface, as they do in sputter deposition, shadowing can also occur [46]. Perturbations that reach farther into the vapor phase than others tend to collect more of the atoms arriving at angles other than normal incidence. Shadowing can lead to competitive growth of columns with structures similar to those shown in Fig.1.3c but with the grain boundaries replaced by walls of low density or voided material.

The competitive polycrystalline growth illustrated in Fig.1.3c can be best understood by considering the action of adatoms with finite mobility, which, upon arriving in the vicinity of a grain boundaries diffuse to attach to grains and thus minimize the boundary curvature. Thus the competition among grains at the surface of the film can be viewed as a two-dimensional grain growth process in which the boundaries are mobile only at the surface of the film, and the mobility of the boundaries is related to the adatom diffusivities as well as to the time during which adatoms can move before being buried by newly arriving adatoms. This diffusion time is related to the deposition rate. [45]

Adatom diffusion on the substrate surface, the rate of adatom desorption, and the rate of nucleation control the grain size at impingement and are all exponentially dependent on temperature When adatom mobilities are low, grain boundary mobilities are also low, and initial grain sizes are small and tend to change only through coarsening at the surface of the growing film. Bulk, grain boundary and surface self-diffusivities for a material at given temperature, tend to be lower the higher the melting temperature of that material. This leads to the tendency to observe similar structural evolution for materials within the same materials class at similar homologous temperatures [45].

Structure-zone models have proven very useful in providing an overview of the relationship between the microstructure of vacuum deposited coatings and the most prominent deposition parameters.

- The low temperature ($T/T_m < 0.3$) *zone 1* structure was columnar, consisting of tapered units defined by voided growth boundaries of the type shown in Fig. 1.2;
- The *zone 2* structure ($0.3 < T/T_m < 0.5$)) consisted of columnar grains, which were defined by metallurgical grain boundaries and increased in width with T/T_m in accordance with activation energies typical of surface diffusion;
- The high temperature *zone 3* ($T/T_m > 0.5$) structure consisted of equiaxed grains, which increased in size in accordance with activation energies typical of bulk diffusion.

The first structure-zone model published by Movchan and Demchishin (MD) in 1969 [47] was later extended to magnetron sputtered metal films by adding an axis to account for the effect of the Ar working gas pressure.

In this model, the MD zones were associated with conditions where the physics of coating growth was dominated in turn by mechanisms associated with each of the three regions shown in Fig. 1.2

- *zone 1*: atomic shadowing during transport;

- *zone 2*: surface diffusion;

- *zone 3*: bulk diffusion.

A fourth zone consisting of a dense array of poorly defined fibrous grains was identified in the region between zones 1 and 2 and termed *zone* T since it was believed to be a transition state between the two MD zones [48].

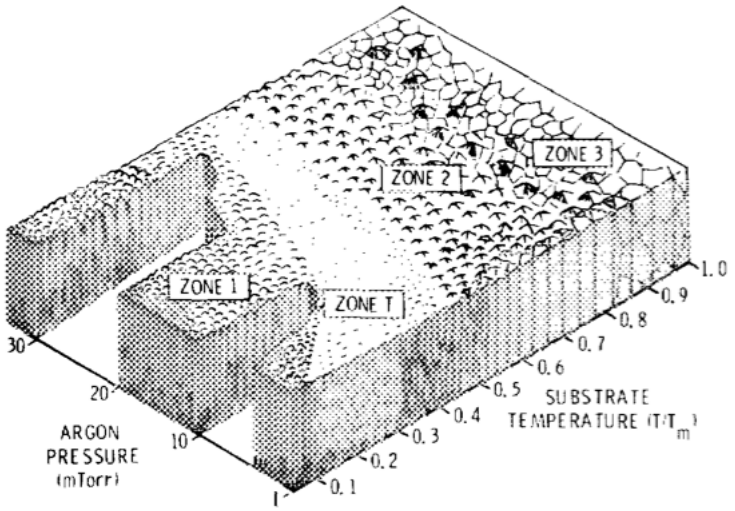

Figure 1.5: Microstructure zone diagram for metal films deposited by magnetron sputtering. T is the substrate temperature and T_m is the coating material melting point.

As a general rule, at sufficiently high temperatures bulk chemistry and diffusion dominate, so that a coating loses all memory of the earlier steps in its growth. Similarly, at intermediate temperatures, surface chemistry and diffusion can dominate over considerations such as shadowing that relate to the transport of the flux to the substrate. Thus it is in the low T/T_m regime where the coating microstructure is dependent on a plethora of parameters. These include the apparatus configuration, substrate surface morphology, and the working gas pressure, all of which influence the coating atom arrival directions and the energy and momentum delivered to the surface by the sputtered species and/or other energetic bombarding species [43].

The zone diagrams of Movchan & Demchishin and Thornton are useful tools for semi-quantitatively capturing and illustrating the expectations for structural evolution as a function of the process parameters, deposition temperature, and pressure. However, it is important to note that the such diagrams are developed for a specific material or class of materials (typically refractory bcc metals) and are based on assumptions about the deposition technique (typically sputter deposition) and specific processing conditions, such as deposition rates and background impurity gas pressures, both of which affect the purity of the deposited films. [45] While materials within the same class tend to have similar diffusivities at similar homologous temperatures, diffusivities for materials from different

materials classes can have widely varying diffusivities, even at the same homologous temperature [49].

We decided to work at room temperature throughout the project, thus increasing the relevance of pressure. The working pressure in the magnetron sputtering deposition technique has been classified into three regimes according to the mechanism of transport of the sputtered atoms. At low pressure the transport is ballistic so that the sputtered atoms have almost no collisions with gas atoms. At intermediate pressures (those used in this work) the lighter sputtered atoms (oxygen) suffer more the changing of momentum due to collisions than the heavier atoms (zinc and gold). In the third regime at high pressure the transport is a purely diffusive mechanism where all the sputtered species suffer collisions and lose their high kinetic energy leaving less energy for surface diffusion [50].

These three regimes are classified according to an approximation that uses the kinetic theory of gases and relates it to the source to substrate distance: if the pressure is increased so that the mean free path for elastic collisions between the sputtered atoms and sputtering gas is of the same order of magnitude of the target to substrate distance, then the oblique component of the flux increases due to the gas scattering. This leads to a more open structure. On the other hand, lowering the pressure reduces the oblique component and the transportation is more ballistic, which in turn creates a more dense coating. For the conditions used in this work (room temperature, pressure $\sim 10^{-2}$ mbar) the mean free path distances are of the same order of magnitude of the source to substrate distance.

The voided growth defects that define the *zone 1* structure are a consequence of atomic shadowing. Shadowing induces open boundaries because high points on the growing surface receive more coating flux than valleys, particularly when a significant oblique component is present in the flux [48] . [51] Substrate surface roughness, or step-like features commonly used in microcircuit fabrication, promote *zone 1* type behaviour by creating oblique deposition angles. The inert working gas pressure enters the problem because collisional scattering by the inert gas atoms enhances the oblique component in the deposition flux. This scattering effect has a much greater influence on the coating structure than the adatom mobility reduction associated with adsorbed inert gas species on the substrate surface [43].

The computer simulation studies have provided additional support for the proposition that the columnar *zone 1*/*zone* T structure is a fundamental consequence of low mobility deposition and the identification of the *zone* T structure as a *zone 1* structure on a smaller size scale, and as the internal structure of the *zone 1* units [52].

1.3 Optical and physical properties of metallic nanoparticles

The very different behaviour of materials at the nanoscale from that of the bulk state originates mainly from the dimensions alone. As the size of a material reduces, the number of atoms at the surface compared to the number of atoms in the material itself increases, leading to an important role of the surface properties in the physical and electronic properties of the materials. Bulk gold looks yellowish in reflected light, but thin Au films look

blue in transmitted light. This characteristic blue color steadily changes to orange, purple and red as the particle size is reduced down to ∼3 nm.

Studying metallic nanoparticles attracts great interest because of their unusual chemical and physical properties, which make them suitable for many technological applications such as catalysis, electronics, optics, and biotechnology. In particular, noble metal nanoparticles embedded in dielectric host presents a special class of materials with unique and tunable properties.

Metallic nanoparticles exhibit a strong UV-VIS absorption band that is not present in the spectrum of the bulk material. This absorption band is due to the collective excitation of the conduction electrons when the size of the metal particle decreases to scales smaller than the mean free path of the electron in the metal [53]. This is known as localized surface plasmon resonance (LSPR). A plasmon is a collective excitation of the electrons in a metal. Plasmons as well as phonons in solids are examples of collective excitations. The LSPR peak position can be shifted from visible to the near infra-red region of the electromagnetic spectrum by either varying the dielectric function of the surrounding medium or by engineering the shape, size and distribution of nanoparticles [54]. Consequently, films comprised of metal nanoparticles dispersed in oxide matrices are regarded as functional materials and exhibit characteristics that are not observed in bulk metals or oxides.

The optical properties of metal nanoparticles are dominated by the collective oscillation of the conduction electrons resulting from the interaction with electromagnetic radiation. Hence this properties are mainly observed in Au, Ag, and Cu in which plenty of free conduction electrons are available. The electric field of the incoming radiation induces a polarization of the free surface electrons with respect to the heavier ionic core of the particles. A restoring force in the nanoparticle tries to compensate for this, resulting in a collective oscillation of the electrons with a unique resonance wavelength which depends on a number of factors, among which particle size and shapes, as well as the nature of the surrounding medium, which are the most important factors [55].

An understanding of the optical properties of noble metal nanoparticles holds both fundamental and practical significance. Fundamentally, it is important to systematically explore nanostructure characteristics that cause variation of optical properties as well as provide access to regimes of predictable behaviour. Practically, the tuneable optical properties of nanostructures can be applied as materials for surface-enhanced spectroscopy [55] [56] [57], optical filters [58] [59], plasmonic devices [60] [61], and sensors [62].

Metals absorb light primarily through electronic transitions. In metal particles, three types of transition are possible:

1. Interband transitions (excitation of the electrons from the filled valence band to empty levels in the conduction band)

2. Intraband transitions (transition within the conduction band)

3. Plasmon excitation (a collective oscillation of the conduction electrons)

Therefore, embedded systems consisting of Au nanoparticles dispersed in ZnO matrix are expected to exhibit the combination of the unique characteristics of nanoparticles and transparent conducting oxides. These factors motivated us to study the optical properties of Au and Ag nanoparticles embedded ZnO thin films.

Doping with other materials was also possible. Matsubara et al. report of Al-, B- and Ga-doped ZnO films with a resistivity of $2.5 \cdot 10^4$ Ω cm and an average optical transmission of 91% for wavelengths between 400 and 1100 nm for the Al-doped film and $2.5 \cdot 10^4$ Ω cm and 81% for the Ga-doped ones [63].

Chapter 2

Experimental Techniques

In this chapter we will present the equipment and the conditions utilised to synthetize the samples.

2.1 Equipment

The ZnO thin films were grown in a vacuum chamber (see Fig.2.1), colloquially named *Caracol*, designed by Dr. Prof. L. Soriano de Arpe. The experimental set-up is composed of a high vacuum chamber, with a base pressure $< 5 \cdot 10^{-7}$ mbar and two radio frequency magnetron systems. The vacuum is achieved by means of a Turbo Molecular pump assisted by a Dry Scroll pump and monitored by two vacuometers: a Varian EYESYS MINI-IMG cold cathode Gauge controller for low pressure and a Pirani for high pressure. Although the molecular regime (pressure in the range $10^{-8} \div 10^{-4}$ mbar) is adequate for preserving the chamber in clean conditions before any sputter gas mixture, reactive magnetron sputtering technique requires working pressures in the viscosity range ($P > 5 \cdot 10^{-3}$ mbar). Pumping occurs through two different channels, both of which can be sealed with right angle valves that allow for fine adjustment of their conductance. In order to reach the viscosity range, the bigger channel is sealed and pumping is only possible through a right angle valve which dramatically reduces the conductance. This limitation in the pump helps to maintain the working pressure with high stability. The chamber has a gas mixture inlet system which provides the needed sputtering gas for the reactive plasma. Argon and oxygen are introduced through a variable leak valve by using two independent flow meters. The flow meter accuracy (Bronkhorst High-Tech) lies between 1% and 4% of his maximum conductance: 200 mlN/min (millilitres at normal conditions) [13]. By varying the percentage of gas with the flow meter a mixture of Argon and oxygen can be obtained.

The magnetrons are hosted in two vacancies in the lower part of the chamber and are positioned at a 24°angle with respect to the vertical axis (see Fig.2.3). This is the so-called *off-axis* geometry: the angle helps to produce nanostructured coatings with higher porosity due to the arriving of sputtered species with larger horizontal component. [64] The sputtering deposition rate decays as $1/r^2$ as it is a solid angle particle distribution coming

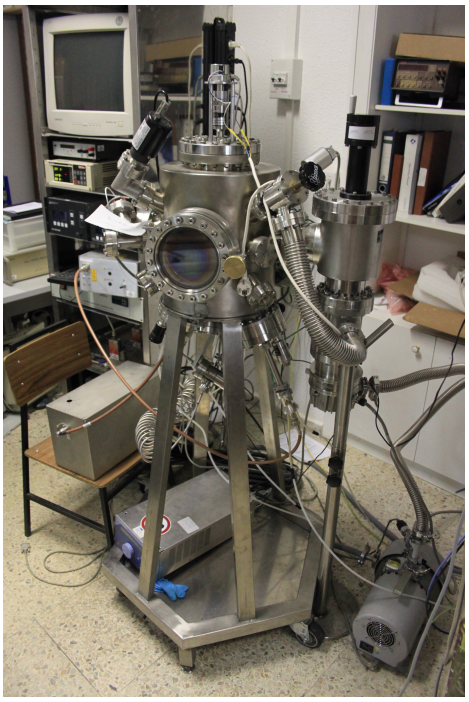

Figure 2.1: The High Vacuum Chamber *Caracol* with two off-axis magnetrons. The vacuum system is composed of a Turbo Molecular and a Dry Scroll pump, two pressure Gauges, and two magnetrons. The base pressure can reach 10^{-8} mbar.

from the target surface. Atoms sputtered from the target surface distribute primarily along the directions of the close packed planes in the crystal [38], however this is avoided by using polycrystalline targets, obtaining therefore more uniform deposits. The off-axis geometry reduces the irradiation of the substrate by high-energy particles sputtered from the target surface decreasing the stresses in the films originated from the ion impinging. [65]

The rotary sample holder is made of a stainless steel axis connected to a copper plate which rotates at a slow speed (about 10 rpm). This rotation is intended to grow isotropic coatings with no dependence of any planar direction due to the off-axis flux of material. Substrates are attached to the holder using screws or carbon-tape specifically designed for high vacuum to secure the stability. Above the substrates plate, and with no rotation, there are three halogen lamps (50 W power each) which provide the heating of the substrates through the plate, made of copper and rotating to ensure the temperature is uniform. Substrates can be heated to a temperature of 400°C. In Fig.2.2 a picture of the frontal view of the vacuum chamber is shown. A quick access door with a view port and a KF Viton o-ring seal is used to access the chamber and manipulate the sample holder. Through the viewport the magnetron heads (covered by shutters), the copper sample holder and the lamps can be seen.

The targets were 50.0±0.5 mm in diameter and 3.0±0.05 mm thick with a purity of 99.995% for the ZnO target and 99.999% for the Au one. The target is positioned on a copper disc for its good thermal conductivity which ensures that the target is well refrigerated by the water flowing beneath it. A silver epoxy is used to glue the target

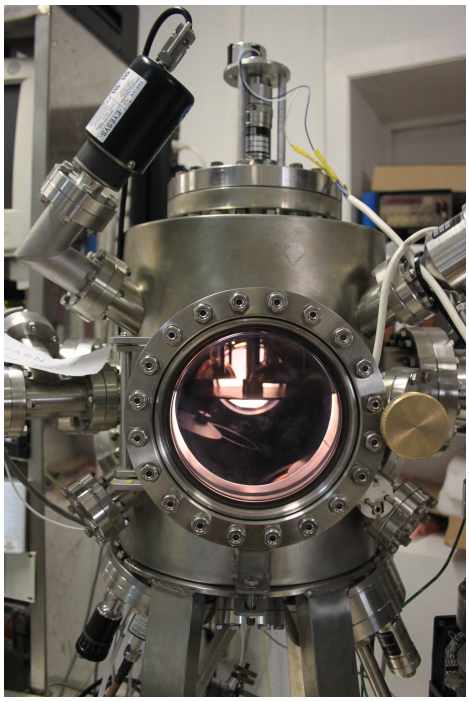

Figure 2.2: Frontal view of *Caracol*

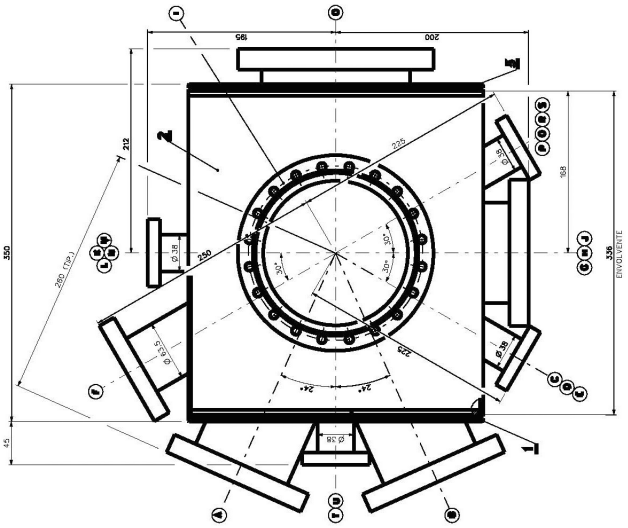

Figure 2.3: Original blueprint of the HV chamber *Caracol*

to the copper disc, again to ensure a good dissipation of the heat generated during the sputtering.

The magnetron heads are covered with a shutter to prevent the contamination of the samples while the plasma is being initiated and that can be opened when the plasma has stabilized. The ZnO target is installed on the left magnetron, which is equipped with a focusing cone to increase the deposition rate and limit contamination of the targets while both plasmas are activated; the Au target is installed on the magnetron on the right. The colour of the plasma depends both on gas mixture composition and target used. When the ZnO target is used, the plasma shows a pale violet colour, while the Au target originates a bright yellow plasma. The substrate-to-target distance was 20 cm for the first part (only ZnO sputtered) and then adjusted to 12 cm for both magnetrons in the second part of the experiment (ZnO-Au co-sputtering).

2.2 Sample Growth Procedure

The samples were grown by means of radio frequency (RF) magneto-sputtering with a controlled atmosphere of Ar and O_2. All samples were grown at room temperature.

The substrates used were chosen to best fulfil the needs of the various characterisation techniques.

- Thin silicon crystals with orientation (100) were selected for X-Ray Photoelectron Spectroscopy (XPS) and ultra-high resolution Scanning Electron Microscopy (SEM)

imaging;

- SEM imaging was also carried out on AAO/Al membranes (Anodic Aluminium oxide Membranes, AAM), which have a honeycomb pattern nanoholes (35 nm pore diameter, 100 nm interpore distance) on the Allumina side deposited on Al; the two sides, identical to the naked eye, can be told apart by the difference in electrical resistance (i.e. the Al side is conductive while the other is not);

- Two kinds of glasses were used: Menzel-gläser colourless borosilicate coverglass (18x18 mm, 0.13-0.16 mm thickness) for UV-VIS Spectroscopy and X-Ray Diffraction (XRD), and standard microscope slides for profilometry, four-point probe resistivity measurements and X-Ray Fluorescence;

- A 480Å thick amorphous SiO_2 layer obtained from thermal oxidation of a Si wafer was used for ellipsometry measures.

Before being put in the chamber, all the samples (except for the AAM) were cleaned with an ultrasound treatment for 5 minutes while immersed in acetone and then again in methanol. A 30 minutes mini-baking at $\sim$120°C for desorption is then applied once the pressure is below 10^{-6} mbar. The copper sample holder was scrubbed after every deposition and then cleaned with acetone and methanol before the fixation of the samples. To prevent any possible contamination of the samples, a pre-sputtering of 10-15 minutes was carried out before any deposition in order to clean the targets from impurities which might have contaminated them when the chamber was opened between different syntheses.

Once the base pressure was reached, the turbo molecular pump was put into *Low Speed* (700 Hz) mode and the big pumping channel was sealed. Then, the gas inlet valve was opened and the desired gas mixture was set on the software that regulates the flowmeter and ensures that flux is kept stable. The desired pressure is then reached by adjusting the valve on the right angle pumping channel. After the pre-sputtering, the growth process can begin.

2.2.1 ZnO series

The first series (denoted simply 'ZnO-0-100') investigates the effect of O_2 on the samples. The O_2 percentage was progressively increased in steps of 10% and was intended to contain 11 samples ranging from 0% to 100%.

The target-sample distance was kept at $\sim$ 20 cm.

As we can see in Fig.2.4, the deposition thickness is very uniform and the transparence of the coating is very clear. From the comparison of the two sets of substrates after deposition, it is instantly evident that oxygen has an influence on the thickness of the deposited coating. This will be discussed in greater detail in 3.1.

A very long growth time was required to have a sufficient film thickness so after this series we decided to modify the chamber so that the target-sample distance was reduced to about half (from $\sim$ 20 cm to $\sim$ 12 cm). After testing with 100W and 50W, we decided

Table 2.1: Growth parameters of series ZnO

Sample	Target	P_{O_2} [mbar]	P_{Ar}	Power [W]	Time [min]	Pressure [mbar]
ZnO-0	ZnO	0% ($< 10^{-7}$)	100%	150	120	$2.4 \cdot 10^{-02}$
ZnO-10	ZnO	10% ($1.8 \cdot 10^{-03}$)	90%	150	120	$1.8 \cdot 10^{-02}$
ZnO-20	ZnO	20% ($3.8 \cdot 10^{-03}$)	80%	150	120	$1.9 \cdot 10^{-02}$
ZnO-30	ZnO	30% ($4.5 \cdot 10^{-03}$)	70%	150	120	$1.5 \cdot 10^{-02}$
ZnO-50	ZnO	50% ($8.5 \cdot 10^{-03}$)	50%	150	120	$1.7 \cdot 10^{-02}$
ZnO-70	ZnO	70% ($9.8 \cdot 10^{-03}$)	30%	150	120	$1.4 \cdot 10^{-02}$
ZnO-100	ZnO	100% ($1.4 \cdot 10^{-02}$)	0%	150	120	$1.4 \cdot 10^{-02}$

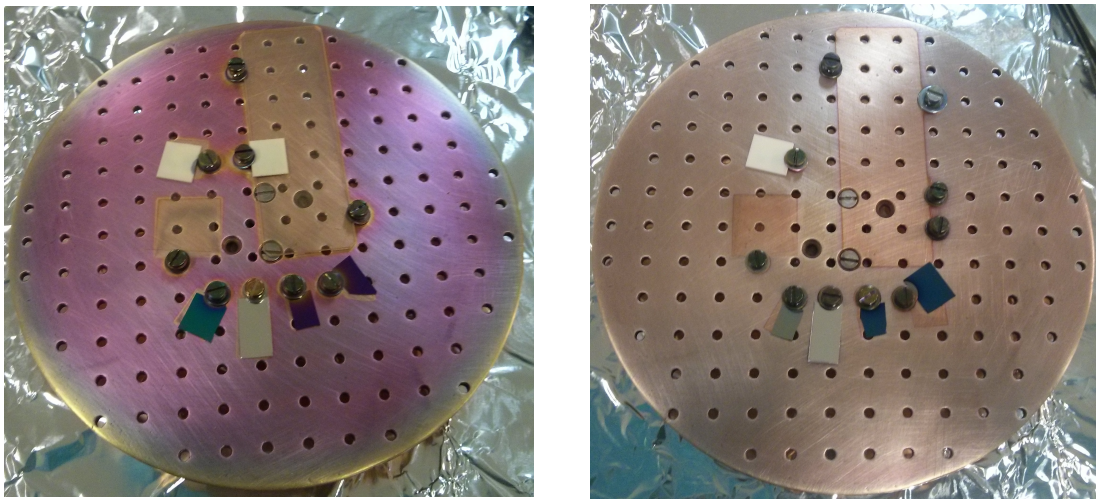

Sample ZnO-0 Sample ZnO-50

Figure 2.4: Sample holder and substrates after deposition for samples from the ZnO-0-100 series

lowered the power for the ZnO magnetron to the latter. This power still allowed us to obtain a higher deposition rate so that we could halve the growth time maintaining a comparable film thickness. Moreover, the lower power further reduced the risk of potentially damaging bombardment by energetic negative argon ions. However, the reduced distance worsened the thickness uniformity because the disc was now seen under a broader solid angle and the solid angle of maximum deposition included a smaller area. For this reason we had to change the disposition of the substrates on the disc to ensure that they all remained in the most densely coated central region. The difference in thickness is responsible for the different coloration of the coating (see Fig.2.5), which shows the whole iris across the sample holder for certain growth parameters.

While running the tests to decide the new ZnO magnetron power, we also measured the deposited coating thickness across the sample holder disc in order to understand which disposition better ensured thickness uniformity for the samples. The results are presented in Tab.2.2 We used a 100% Ar plasma at a pressure of $1.5 \cdot 10^{-2}$ mbar for the tests and

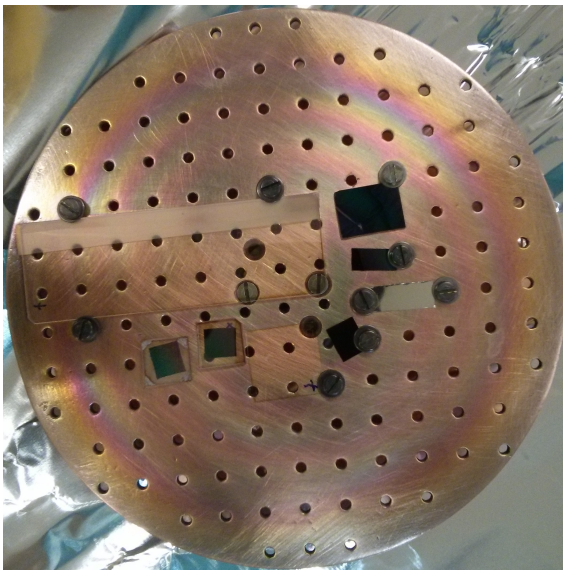

Figure 2.5: Sample holder and substrates after deposition for one of the testing samples

the new target-sample distance of 12 cm. The power is indicated in the sample name.

Table 2.2: Thickness of the deposited coating with respect to the distance from the center of the sample holder

ZnO-100W		ZnO-50W	
Distance [mm]	Thickness [nm]	Distance [mm]	Thickness [nm]
8.8 ± 0.1	700 ± 70	7.6 ± 0.1	230 ± 20
16.9 ± 0.1	690 ± 70	17.3 ± 0.1	230 ± 20
28.3 ± 0.1	625 ± 60	30.6 ± 0.1	220 ± 20
42.5 ± 0.1	510 ± 50	43.7 ± 0.1	185 ± 10
52.7 ± 0.1	400 ± 40	57.3 ± 0.1	130 ± 10
63.0 ± 0.1	200 ± 20	69.3 ± 0.1	75 ± 10
70.1 ± 0.1	130 ± 10		

A preliminary analysis of the grown samples showed that an increase of oxygen inhibits the electrical capabilities of the zinc oxide and therefore the series was aborted. With these information we then decided to try a co-sputtering technique in order to dope the ZnO with Au nanoparticles.

2.2.2 Au doped ZnO series

An atmosphere of pure Ar was used in order to maximise ZnO conductivity and deposition efficiency.

The shorter target-sample distance helped, in turn, to increase the effective ZnO sput-

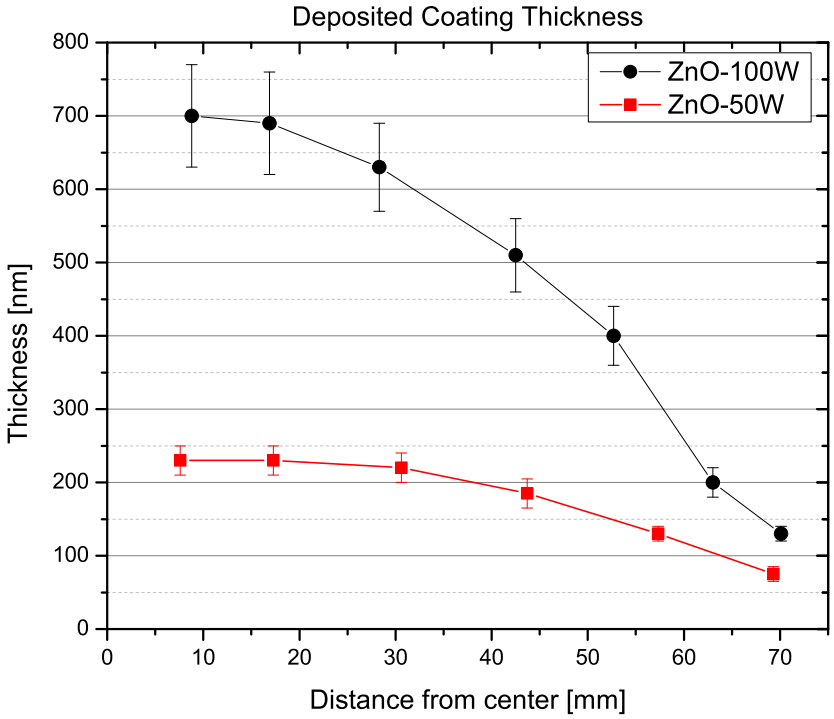

Figure 2.6: Thickness of the deposited coating with respect to the distance from the center of the sample holder

tering rate. This is very important because Au has a very high sputtering rate (8-fold that of ZnO) [66], so reducing the distance helps to space out the gold deposited and inhibits the formation of Au clusters.

The second part of this work focused on finding an appropriate growth method in order to have Au doped ZnO thin films that presented good characteristics of transmittance and conductivity.

This third series was denoted 'ZnOAu-manual' and the samples were labelled with the notation ZnOAu-*ZnO magnetron power(W)*.Au *up time(s)*.Au *down time(s)*. Tab.2.3 reports the growth parameters used in the series. All samples were grown at a pressure of $5.0 \cdot 10^{-2}$ mbar and with a target-sample distance of ~ 12 cm.

Table 2.3: Growth parameters of series ZnOAu-manual (Parameters are referred to Au magnetron unless specified)

Sample	Target	P [W]	Up Time	Down Time	Au:ZnO time ratio
All samples	ZnO	50	60 min	0 s	n.a.n.
ZnOAu-10.6.54	Au	10	6 s	54 s	1:10
ZnOAu-10.6.114	Au	10	6 s	114 s	1:20
ZnOAu-5.6.54	Au	5	6 s	54 s	1:10
ZnOAu-5.6.114	Au	5	6 s	114 s	1:20
ZnOAu-5.3.147	Au	5	6 s	147 s	1:50

Since the target-sample distance was reduced from the previous series, we lowered the power for the ZnO magnetron to 50W. This power still allowed us to obtain a higher deposition rate so that we could grow samples in one hour instead of two, while it further reduced the risk of potentially damaging bombardment by energetic negative argon ions.

To limit the otherwise overwhelming sputtering rate of gold (8 times higher than that of ZnO [66]), we used a power of only 5W on its magnetron (after an initial test with 10W). This power would not be enough to initiate a plasma on its own at our working pressure. However, the chamber was already filled with the Ar plasma created by the ZnO magnetron, so the avalanche threshold had lower requirements (due to the hysteresis of this phenomenon) and the Au flux was clearly visible to the naked eye.

The growth method was still embryonic at this stage, with the gold sputter regulated by hand opening and closing the magnetron shutter. This limited the possibilities of a selective growth and forced us to employ long growth time for gold, thus creating a relatively thick gold layer inside the film and favouring clusterization. Both of these formations deny spoil the transmittance properties of the samples.

We then set up the equipment so that a pulsed plasma could be obtained for the Au magnetron. This enabled us to have a much more controlled gold deposition on the samples. The gold nanoparticles deposition was now evenly spaced out, deposited for equal amount of times and of course much less affected by human error. Our RF source could induce a pulsed plasma of frequencies in a range of $1 - 1000$ Hz in 1 Hz steps and with a Duty Cycle (plasma deposition Up Time) ranging from 1 to 100% with steps of 1%.

This third series was denoted 'ZnOAu-pulsed' and the samples were labelled with the notation ZnOAu-*Frequency(Hz)*.Au *Up Time (%)*. Tab.2.4 reports the growth parameters used in the series. All samples were grown at a pressure of $5.0 \cdot 10^{-2}$ mbar and with a target-sample distance of ~ 12 cm. The magnetron power was kept at 50 W and 5 W for the ZnO and Au magnetrons respectively throughout the whole series.

2.3 X-Ray Diffraction (XRD)

Crystalline structure of the samples can be reconstructed through X-Ray Diffraction (XRD). This technique consists in shooting a monochromatic beam of X-Rays on the sample and collecting the diffracted X-Rays with a detector. Varying the incidence angle of the beam creates a series of peaks and valleys depending on the different kind of interference created by the diffracted rays. There is constructive interference when the atomic layer separation is a whole multiple of the wavelength used to investigate the sample. This happens for a definite series of angles determined by Bragg's law:

$$2d \sin\theta = n\lambda \tag{2.1}$$

When the X-rays beam arrives at low incidence angles to the sample surface, the technique is called *Grazing Incidence XRD*, which is more sensitive to the surface structure. This configuration is the most suitable to study thin films, since the effects of the substrate or support can be highly reduced or even avoided, and is the one used for our measurements.

Table 2.4: Growth parameters of series ZnOAu-pulsed. (Parameters are referred to Au magnetron unless specified)

Sample	Target	P [W]	f [Hz]	Up Time	Au:ZnO time ratio	Au pulse time
All samples	ZnO	50	Continuous	100%	n.a n.	n.a n.
ZnOAu-100.1	Au	5	100	1%	1:100	0.1 ms
ZnOAu-100.2	Au	5	100	2%	1:50	0.2 ms
ZnOAu-100.3	Au	5	100	3%	1:33.3	0.3 ms
ZnOAu-100.5	Au	5	100	5%	1:20	0.5 ms
ZnOAu-10.1	Au	5	10	1%	1:100	1 ms
ZnOAu-10.2	Au	5	10	2%	1:50	2 ms
ZnOAu-10.3	Au	5	10	3%	1:33.3	3 ms
ZnOAu-10.5	Au	5	10	5%	1:20	5 ms
ZnOAu-1.1	Au	5	1	1%	1:100	10 ms
ZnOAu-1.2	Au	5	1	2%	1:50	20 ms
ZnOAu-1.3	Au	5	1	3%	1:33.3	30 ms
ZnOAu-1.5	Au	5	1	5%	1:20	50 ms

XRD is a non destructive technique with a penetration depth of about 30 μm. Samples do not require special preparation, which make this a powerful technique routinely used in the field of material science. This technique can detect every kind of atoms provided that they are located in crystallographic planes, therefore amorphous materials cannot be detected. The signal measured greatly depends on the sample crystal quality.

An example of diffraction pattern is shown in Fig.**??**

Measurements were carried out in SIdI-UAM with a Siemens D-5000 diffractometer, Soller slits, and Si-Li detector SOL-X (Bruker). The diffraction patterns were acquired with Cu Kα radiation, which has a $\lambda = 0.154056$ nm. The incidence angle used was of 0.5°(*grazing incidence* condition), 2θ measurements were taken in the range 15-80°with a sampling step of 0.04°and 2 s acquisition time per point.

Measures were taken of films grown on Menzel-gläser, which has an amorphous structure and thus does not interfere with the measure. The presence of background noise is inevitable and it is due to a sum of various elements: inelastic interaction of the incident radiation, interaction of the radiation with air, X-Ray fluorescence, incomplete monochromatisation, detector noise... Noise was removed before fitting of the peaks.

Diffractions pattern were compared with the ones present in the *Crystallography Open Database* with the dedicated software *Match!*. The most relevant peaks in ZnO and Au diffraction patterns are presented in 2.5

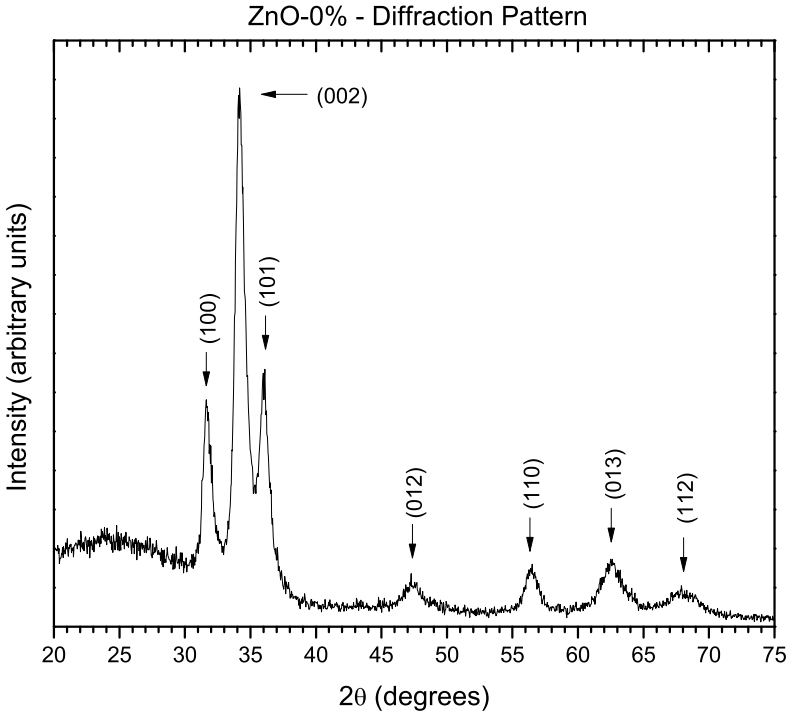

Figure 2.7: Example of XRD diffraction pattern (Sample ZnO-0)

Table 2.5: XRD pattern for ZnO [67] [68] and Au [69]

ZnO		Au	
2θ	Plane (h k l)	2θ	Plane (h k l)
31.77°	(1 0 0)	38.38°	(1 1 1)
34.50°	(0 0 2)	44.53°	(2 0 0)
47.62°	(1 0 2)	64.82°	(2 2 0)
56.67°	(1 1 0)	77.91°	(3 1 1)
62.90°	(0 1 3)		
68.10°	(1 1 2)		

2.3.1 Crystal domain size

According to the Scherrer equation [70], there is a relationship between the broadening of a peak in a diffraction pattern and the average size of sub-micrometric crystallites, τ

$$\tau = \frac{\kappa\lambda}{\beta\cos\theta} \tag{2.2}$$

where κ is a constant determined by the material (we used the value $\kappa = 0.89$ [71], λ is the incident radiation wavelength, β is the FWHM of the peak and θ is its position according to Bragg's law. Scherrer constant κ is usually taken to be 0.9, but its value depends greatly on the crystallite shape [72]. Note that β is an angular width, in terms of 2θ (not θ), and not a linear width.

However, this equation is a rough estimation valid only for crystallites smaller than half a micron of diameter and is based on the assumptions of a perfect crystal lattice and an incident beam composed of parallel and monochromatic radiation. The Scherrer formula provides a lower bound on the crystallite size and it should not be confused with grain size: a particle or a grain can be made up of one or more crystallites, therefore we cannot speak of grain size estimated by Scherrer but we can confirm the correlation between these two concepts. A variety of factors can contribute to the width of a diffraction peak besides instrumental effects and crystallite size; the most important of these are usually inhomogeneous strain and crystal lattice imperfections.

2.4 X-ray Photoelectron spectroscopy (XPS)

Surface analysis by XPS is accomplished by irradiating a sample with monoenergetic soft X-Rays and analysing the energy of the detected electrons.

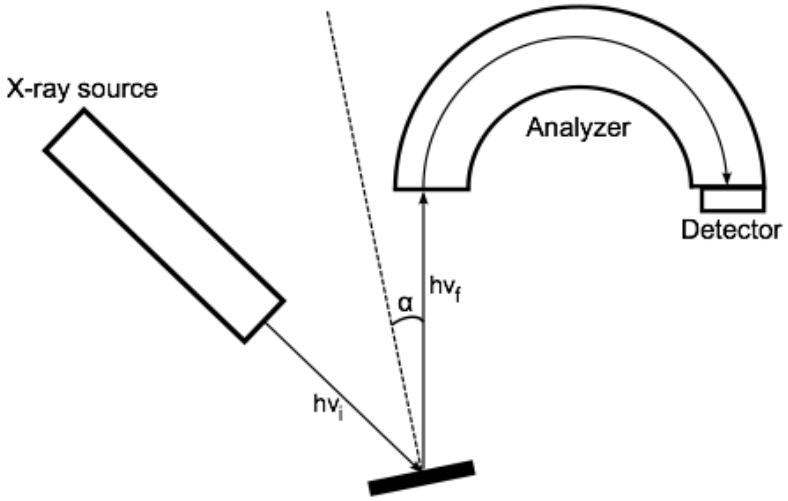

Figure 2.8: Scheme of a typical XPS experimental setup

A typical scheme of a XPS experimental setup can be seen in Fig.2.8. The X-rays from the source arrive at the sample and induce the emission of electrons from the surface

atoms, which are energetically separated by the analyzer (which usually is a capacitor with a determined geometry) and counted in the detector. The angle between the sample surface normal and the analyzer, labeled α on the scheme, is called the take-off angle, and it is important in determining the sampling depth of our measurement. [73] Ultra-high vacuum conditions ($\sim 10^{-10}$ mbar) are commonly used so the electrons does not interact with themselves or other molecules in their path towards the analyzer, but recent developments [74] [75] have allowed this technique to be used in near-ambient pressure conditions.

The photons interact with atoms in the surface region ($\sim$ 3-5 nm), causing electrons to be emitted by photoelectric effect. The emitted electrons have a measured kinetic energies given by:

$$KE = h\nu - BE - \phi_s$$

where $h\nu$ is the energy of the photon, BE is the binding energy of the atomic orbital from which the electron originated and ϕ_s is the spectrometer work function.

Because each element has a unique set of binding energies, XPS can be used to identify and determine the concentration of the elements in the surface. Variations in the elemental binding energies arise from differences in the chemical potential and polarisability of the compound.

The emitted electrons (photoelectrons) are detected by an electron spectrometer according to their kinetic energy. The analyzer is usually operated as an energy window, accepting only those electrons having an energy within the range of this window. To maintain a constant energy resolution, the pass energy is fixed. Scanning for different energies is accomplished by applying a variable electrostatic field before the analyzer. [76]

Probabilities of electron interaction with matter far exceed those of photons, so while the path length of the photons is of the order of micrometers, that of the electrons is of the order of tens of angstroms. Thus, while ionisation occurs to a depth of a few micrometers, only those electrons that originate within tens of angstroms below the solid surface can leave the surface without energy loss. These electrons which leave without energy loss produce the peaks in the spectra and are the most useful.

Electrons that come from a deeper region undergo inelastic scattering and experience energy loss before emerging from the solid. Therefore, they will appear as having a higher binding energy compared to the one of the level they come from, which will be reflected as an increase of intensity in the part of the spectrum above the binding energy of said peaks. This feature is usually referred as the spectrum background. It is continuous, since the scattering processes are random and multiple, and it also has a sizeable contribution from the Bremsstrahlung radiation from the X-ray source. [73]

Of the many types of lines that can be found in XPS spectra, we will only explain the most relevant for our work: Photoemission lines and Auger lines. These are the results of the two main electron-emitting processes that can occur after X-Ray ionization.

Even if the anode of the X-ray source is clean, its emission can be not entirely monochromatic, presenting minor components at higher photon energies than the main emission

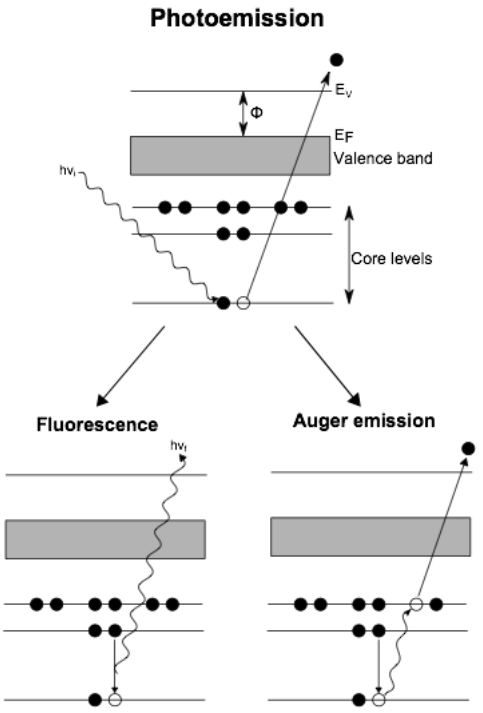

Figure 2.9: Scheme of the photoemission, fluorescence and Auger emission processes

peak. This produces replicas of the peaks produced by the main emission line with a relative position and intensity that depends on the anode material. These peaks are called *x-ray satellites*.

Photoemission lines

Photoemission lines come from a photoemission process (see Fig.**??**), they are usually narrower than the rest and constitute the most important feature of an XPS spectrum. The shape of the XPS photoemission peaks are a combination of the physics involved in the ionization process and the distortions introduced by the experimental equipment. They have complex shapes, and even though they are usually symmetrical, they can also be asymmetrical. Their height is determined primarily by the photoemission cross section (the probability of an electron to be emitted from an atom), which depends on the X-ray energy and flux, and the orbital which is implicated in the photoemission process. Their full width at half maximum (FWHM) depends on the analyzer resolution, on the X-ray source bandwidth, and the lifetime of the core level implicated in the photoemission process. [73]

Their position can change due to a great variety of factors. The most interesting is the chemical bonds between the elements of our sample (e.g., the binding energy of the Zn $2p_{3/2}$ peak is different for metallic Zn), but if the sample is an electrical insulator, the whole spectra is going to be displaced due to charge effects, even if it is connected to ground. This is easily corrected knowing the energy position of a well known peak of our spectra, and correcting the whole spectra until it matches the desired value.

Photoemission peaks are usually modelled by the convolution of Gaussian and Lorentzian

functions. The Gaussian curve is used to simulate any contribution made by the measurement process (such as x-ray line profile, Doppler and thermal broadening, or instrumental response, for example), while the Lorentzian shape simulates the lifetime broadening of the peak. The convolution of these two curves is called a Voigt profile, but since it does not have an analytical form, a Pseudo-Voigt is commonly used instead for simplicity. The Pseudo-Voigt profile is uses a linear combination of Gaussian and Lorentian curves instead of their convolution.

Auger lines

These groups of lines are detected when a Auger process occurs. The Auger emission occurs roughly 10^{-4} seconds after the photoelectric event. The competing emission of a fluorescent x-ray photon is a minor process in this energy range. In the Auger process (see Fig.2.9), an outer electron falls into the inner orbital vacancy, and a second electron is simultaneously emitted, carrying off the excess energy. The Auger electron possesses kinetic energy equal to the difference between the energy of the initial ion and the doubly charged ion, and is independent of the mode of initial ionization. Thus, photoionization normally leads to two emitted electrons: a photoelectron and an Auger electron. The sum of the kinetic energies of the electron cannot exceed the energy of the ionizing photons. [76]

Auger lines come in groups or in complex patterns and are identified by three letters, which indicate the level of initial ionization, the level where the second electron involved in the transition comes from, and the level from which the Auger electron is emitted (K, L, N, O or V, the latter used when the final vacancies are in the valence band). The four main Auger series observable in XPS are KLL, LMM, MNN and NOO. Because Auger lines have kinetic energies which are independent of the ionizing radiation, they appear at the same energy on a binding energy plot, even if the X-Ray source has been changed. [76]

2.5 Optical analysis

2.5.1 Tauc method for measuring band gap

The band gap of a semiconductor (or an insulator) is defined as the energy difference between the top of the valence band and the bottom of the conduction band

In materials with a large exciton binding energy, it is possible for a photon to have just barely enough energy to create an exciton (bound electron?hole pair), but not enough energy to separate the electron and hole (which are electrically attracted to each other) and allow them to participate in electrical transport. In this situation, there is a distinction between *optical bandgap* and *electrical band gap*. The optical band gap is lower in energy that the electrical band gap. However, for zinc oxide and many other semiconductors there is almost no difference between the optical and electrical band gap.

A widely used method to calculate the band gap of a semiconductor film was developed by J. Tauc et al. [77] in 1966. This method was developed for amorphous semiconductors

in which the electron transition is momentum conservative and relates the optical band gap to the absorption coefficient, allowing the gap to be determined by fitting the experimental absorption data. [78] The Tauc relation is defined as:

$$(\alpha\, h\nu)^n = A(h\nu - E_{\text{gap}}) \tag{2.3}$$

where h is the Plank constant, ν is the photon frequency, α is the absorption coefficient, A is a constant related to the band tail at higher energies and E_{gap} is the gap energy. The value of n depends on the nature of the transition: $n = 2$ for a direct allowed transition, $n = 1/2$ in a indirect allowed transition [79]. Zinc oxide has a direct band gap and therefore we used $n = 2$. The absorption of our samples is easily calculated, once the transmittance is measured, through the relation:

$$\alpha = -\frac{1}{d}\ln T \tag{2.4}$$

where d is the film thickness and T is the transmittance. The plot usually presents a sudden fall, which is the part corresponding to the band gap and is the part that we want to fit. The intersection between the fit and the $y = 0$ axis yields the band gap value.

2.6 Ellipsometry

Ellipsometry uses polarized light to characterize thin film and bulk materials. The light undergoes a change in polarization as it interacts with the sample structure. The measurement is typically expressed as two values: Psi (Ψ) and Delta (Δ). The data are then analyzed to determine material properties of interest.

Ψ and Δ represent the raw measurement from an ellipsometer. They describe the change in polarization that occurs when the measurement beam interacts with a sample surface. The incident light beam contains electric fields both parallel (p-) and perpendicular (s-) to the plane of incidence.

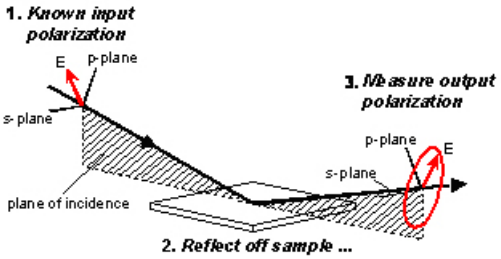

Figure 2.10: Scheme of the functioning of an ellipsometry measurment

The surface differentiates between the p- and s- light, causing a change in the outgoing polarization. This is represented by both an amplitude ratio ($\tan\Psi$) and phase difference (Δ):

$$\tan\Psi\; e^{i\Delta} = \frac{R_{\text{p}}}{R_{\text{s}}} \tag{2.5}$$

where R_{p} and R_{s} are the Fresnel reflection coefficients for the p- and s- polarized light, respectively.

By themselves, Ψ and Δ aren't very informative. We really want to determine film thickness, optical constants, refractive index, surface roughness, and other physical properties of the sample. These properties are found by using the measured values (Ψ and Δ) in various equations and algorithms to produce a model that describes the interaction of light with the sample.

Spectroscopic ellipsometry is very sensitive to the film thickness. As the film thickness increases, there is an increasing separation between the light reflected from the surface and the light that travels through the film, as shown below. This causes a phase delay that is related to both the physical thickness and the index of refraction. Thus, spectroscopic ellipsometry measurements contain the information to accurately measure both thickness and index.

2.7 Van der Pauw method for measuring resistivity

Resistivity was measured in a Van der Pauw four-probe set-up. Van der Pauw method measures the voltage drop across four small contacts located at the periphery of an arbitrary shape flat film. A current is driven across the film through two contacts, while the corresponding voltage drop is measured through the other pair. With this procedure, the film shape dependence of the result obtained can be neglected. [80]. This method applies for well located contacts (at the periphery, the most symmetrically located as possible) of a small area with respect to the total film area and with ohmic behaviour.

Our four-probe equipment is a Hall effect station which incorporates two permanent magnets of 0.58 T in order to measure carrier concentration, mobility, magnetoresistance and Hall effect. Unfortunately the carrier density of the ZnO films was so low that this value was not reliable and therefore the mobility, magnetoresistance and Hall effect parameters, which depend on this concentration, could not be quantified. The equipment used was a HMS-300 model from *Ecopia*, with resistivity range between $10^{-4} - 10^{7}(\Omega$ cm) and a current-source compliance voltage of 12 V, with current range 1 nA-20 mA.

Obtaining ohmic contacts is an important problem when measuring the resistivity. These contacts should occupy a small area with respect to that of the film, have mechanical stability and uniform ohmic behaviour. An ohmic contact should have a behaviour that follows Ohm's law when voltage is applied between its electrodes. The work function between the contact and the film should also be similar [81]. In this work we used a SnIn alloy of composition 95% Sn and 5% In without solder resin. We also tried using Ag contacts [82], but the results were not better than those we obtained with SnIn contacts so their use was discontinued because their creation was much more complicated. These contacts were soldered on square-planar glass substrates.

The way of checking a reasonable ohmic behaviour is by performing a I-V curve at each point probe as is shown in Fig.2.11. Fig.2.12 shows a logarithmic graph of resistivity versus current. Two distinct regions are visible: the plateau of constant resistivity and the negative linear trend. This plateau is directly related with the ohmic behaviour shown

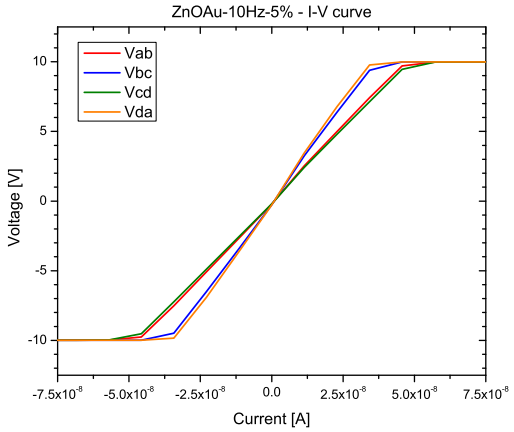

Figure 2.11: I-V curve for ohmic region

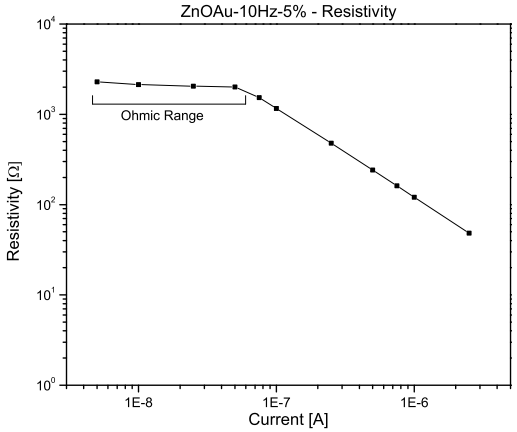

Figure 2.12: Resistivity vs. current

Ohmic contact: in the linear ohmic region of the contact SnIn-ZnO Fig.2.11 a good measurement gives a resistivity value independent of the input current Fig.fig:Hall-example for the same range of current.

in the upper panel, and corresponds to the region in which the compliance voltage of the source can flow current through the sample. The more the insulating behaviour of the sample the shortest the plateau region (the less ohmic contact). The linear points are an artefact of our Hall effect station. The compliance voltage of this apparatus is 12 V, therefore, in order to maintain that constant voltage at higher current values the resistivity measured will be lower. When measuring a highly resistive sample, as is our case for ZnO films, the voltage drop of 12 V is not enough to drive high current values (above 50 nA in Fig.2.12).

The DC resistivity is expected to be constant and independent of the current flowing through the material, therefore the reliable ρ values are those of the plateau for current values 5-50 nA, labelled as Ohmic region in the figure. In order to increase the accuracy of the measurements and reduce the data dispersion, all the values in the linear ohmic range were considered and an average of them was taken as the resistivity value. This was done for every measurement of the resistivity on each coating.

Measurements were carried out assuming a sheet thickness of 0.1 μm; results were then adjusted for the measured thickness according to the formula:

$$\rho_{\text{real}} = \rho_{\text{exp}} \frac{d_{\text{exp}}}{d_{\text{hyp}}} \tag{2.6}$$

The error is mostly due to inaccuracies in measuring the thickness of the samples ($\sim 10\%$), while the one electrical measure has an error of roughly 1%, so its contribution becomes negligible after propagation.

Chapter 3

Experimental Results

In this chapter we will present the results of the various analysis techniques used to characterise the samples. Film thickness was measured with a profilometer and with a Field Emission Scanning Electron Microscope (FESEM), which was also used to determine the morphology of the samples. Surface chemical composition was analysed via XPS while bulk composition was investigated via Total X-Ray Fluorescence. Optical properties were inspected through UV-VIS spectroscopy and Ellipsometry. Finally, electrical properties were evaluated with the Van der Pauw four-point probe method.

3.1 Morphology

To investigate the morphology of the samples grown, we took some pictures with a Field Emission Scanning Electron Microscope (SEM) present at SIDI (Servicio Interpartamental de Investigación). We utilized samples grown over a substrate of crystalline silicon (orientation (1 0 0)), which has a very low roughness, and a substrate of AAO/Al Nanotemplates (Anodic Aluminium oxide Membranes, AAM) membranes with a hexagonal 35 nm diameter nanohole pattern.

Samples were synthetized at room temperature, which corresponds to a low homologous temperature $T/T_m \sim 0.15$ (ZnO melting point 1.975°C). Using Thornton's zone model described in section 1.2.2 we expect a *zone 1* structure, i.e. a vertical columnar growth with grains separated by voids.

The cross section shown in Fig.3.1 on Si substrate reveals that each grain covers most of the film thickness. The grains are grown along the direction normal to the substrate in a columnar shape, but the density of the columns resembles more the transition structure (*zone T*) consisted of densely packed fibrous grains than the pure porous structure corresponding to *zone 1* of Thornton's zone model (See 1.2.2). The size and density of intercolumnar spaces depend on the atomic shadowing during deposition, which is enhanced by the oblique scattering that characterizes the off-axis magnetron geometry. The structure zone models relies not only on the substrate temperature but also on the physical processes that occur during film formation: shadowing, surface and bulk diffusion, and competition

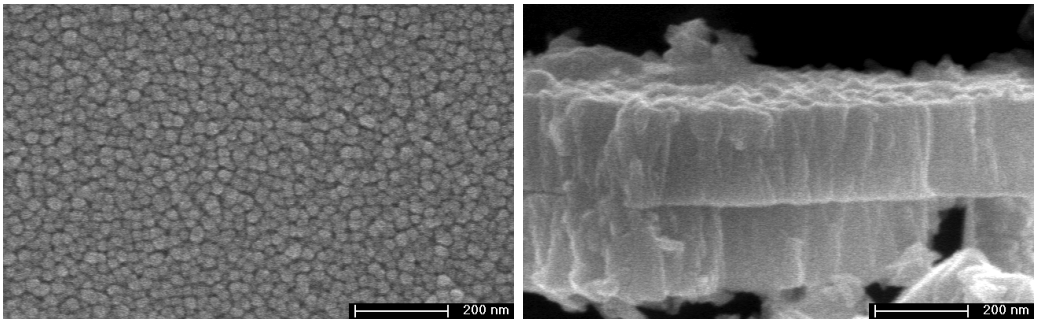

Figure 3.1: SEM front and cross-view images of the sample ZnO-30 grown on Si

of grains and texture. These factors might lead to a predominance of one crystallographic direction over the others, producing textured coatings.

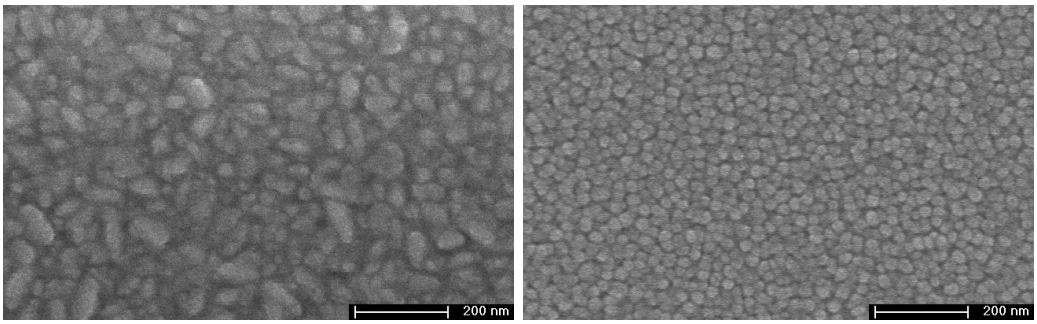

Figure 3.2: SEM front and cross-view images of samples ZnO-0 and ZnO-70 grown on Si

From these images it can be seen that grain size in sample ZnO-0 is very different from the others, which all resemble that of sample ZnO-70 reported as representative. According to these results, samples prepared in the presence of oxygen in the plasma present a considerable grain refinement. The low O_2 content produces larger grains than those observed in films grown with higher oxygen concentrations. We can also observe that oxygen addition not only generates smaller grains but smooths the edges of the grains as well. Grains in Fig.3.2a have much sharper edges than those present in Fig.3.1. These effects of oxygen on grain features have been observed previously by other research groups working on NiO [13] [83].

These features are present, clearly, even, in samples grown on AAM (Fig.3.3).

In Fig.3.3b-d we can see that the coating preserves the hexagonal pattern of pores distribution of the AAM substrate. In both cases it can be observed that ZnO deposits on the pore walls, and the lack of lateral growth keeps the columnar growth in the vertical direction, preserving the pores. This is due to the lower effectiveness of the sputtering caused by the introduction of oxygen.

On the basis of our SEM images we can interpret the growth of the sputtered films on the AAM substrate following the van der Drift competitive model (see 3.2.1) adapted to the roughness of the porous substrate. The first nucleation generation on top of the amorphous

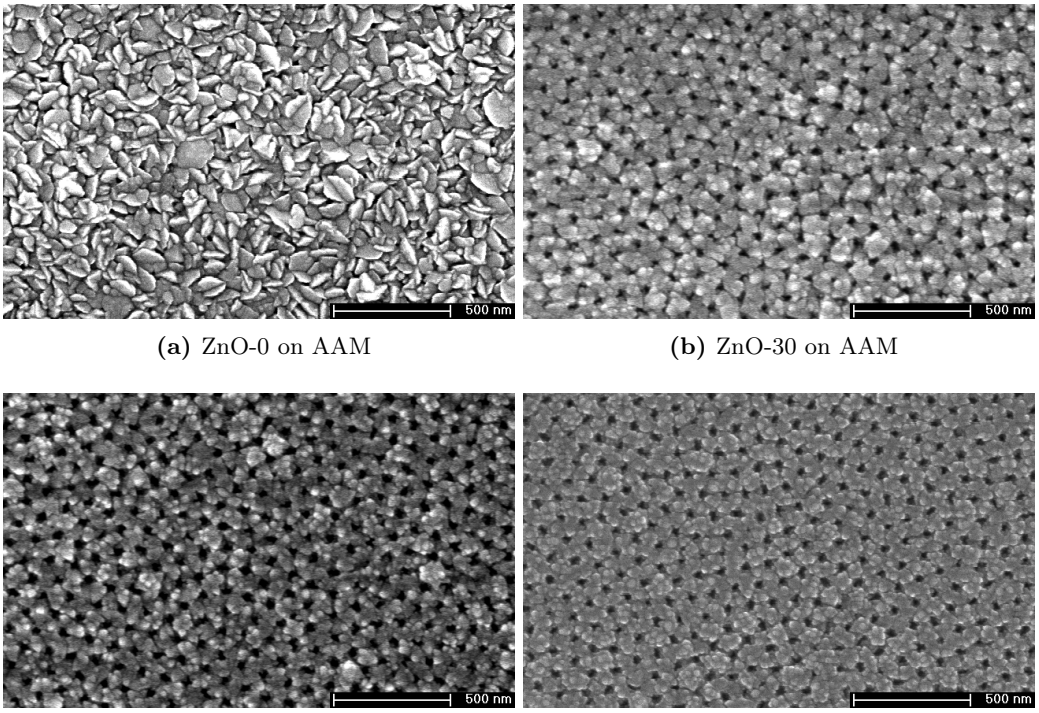

(a) ZnO-0 on AAM **(b)** ZnO-30 on AAM

(c) ZnO-70 on AAM **(d)** ZnO-100 on AAM

Figure 3.3: SEM front-view images of the series ZnO-0-100 grown on AAM

allumina between the pores occurs within grain competition. During this first stage the formed grains have a small size and no columnar shape but arrow shape. The grains cover the top of the column between each six pores and evolve with cylindrical symmetry: the axis of the allumina column is covered with grains from the centre to outside, as if they were arrow heads, producing a cauliflower like shape. A schematic of this growing phase can be seen on the right part of the Fig.3.4. When several layers of material cover the top of the column and the horizontal grain competition seems to be completed, the surviving grains have their faster grow faces oriented perpendicular to the surface substrate, which has high roughness, then they start to grow vertically. These grains of the second generation still have V-shaped form but with higher aspect ratio and thicken the film considerably. Finally when the growth of the V-shaped grains has reached a threshold height the total width of each independent column is high enough to occlude the pores, which were opened since the beginning of the growth. It can also be expected that small amounts of material are deposited through the pores on the internal lateral surface of the cylinder columns, close to the pore edges. The pore diameter is gradually blocked during the whole thickening until they are closed, as it is shown in the left part of the Fig.3.4. We consider this model for the case of rotating substrates and an off-axis incoming of the sputtered atoms, as indicated in Fig.3.4. The nature of this growth is based on several factors, highly correlated among them: deposition rate, obliqueness of the incoming flux of atoms, shadowing effect caused by the amorphous substrate and surface diffusivity of the adatoms.

Cross-view images of ZnO grown on AAM confirm this explanation (see Fig.3.5).

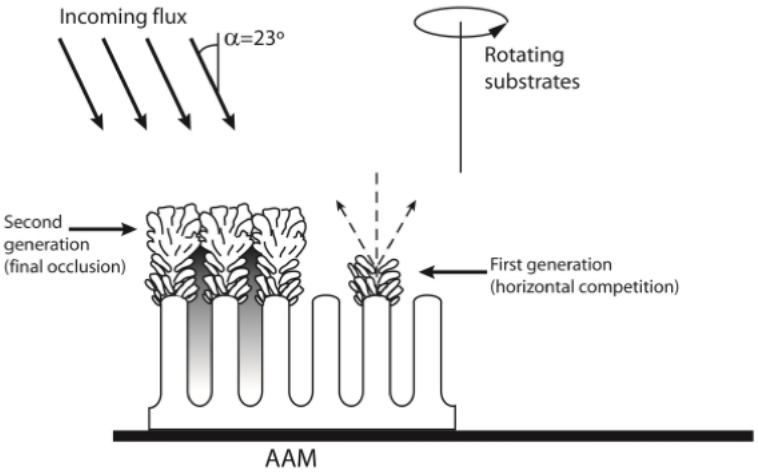

Figure 3.4: Schematic of the grain growth evolution on AAM. The first nuclei deposit on the top of the columns at the edge of the pores. The first generation of grains grow symmetrically respect to the axis of the column opening in V-shape. The second generation of grains, which develop with columnar structure and are survivors of the competitive horizontal grain growth, thickens the film vertically until finally occlusion of the pores.

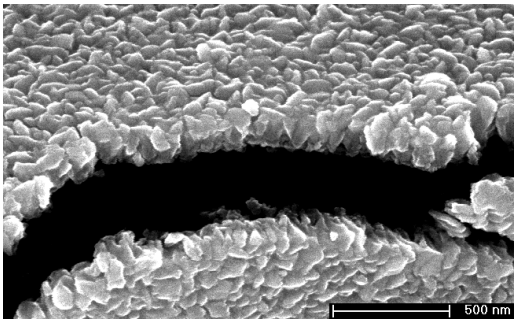

(a) ZnO-0 on AAM

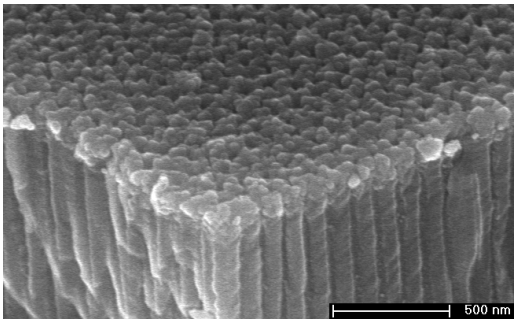

(b) ZnO-30 on AAM

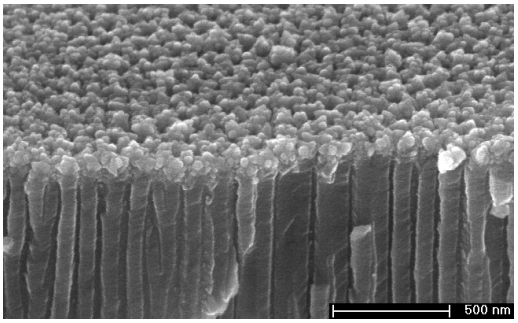

(c) ZnO-70 on AAM

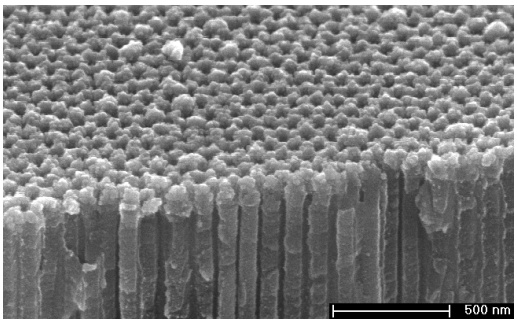

(d) ZnO-100 on AAM

Figure 3.5: SEM cross-view images of the series ZnO-0-100 grown on AAM

The shadowing effect occurs often in PVD processes when non smooth substrates are used. When sputtered atoms arrive at an elevated region of the substrate and nucleate there, they receive more flux than other atoms in more depressed regions, which receive less flux. During growth this flux inhomogeneity over the whole substrate area generate more irregularities and increase the roughness, which results in structures that grow oriented toward the incoming flux. Rough substrates and impurities enhance the shadowing effect, and when the flux of incoming atoms is not perpendicular to the substrate surface but has an oblique component, this effect is even more pronounced. Shadowing effect produces more porous films with voids between the grains [39]. Because of the continuous rotation of the substrates during the growth the coatings are more uniform, reducing the high impact of the shadowing effect. Although the voids and open boundaries can be avoided on smooth and planar substrates such as Si and glass, the AAM substrates present a high roughness and a columnar and porous pattern which raises the threshold at which the uniformity of the coating is achieved.

If the rotational sample holder were not used then the coating would have a preferred microscopical growth direction easily observed through SEM. Works on obliquely evaporated films reveal that the columns are oriented toward the sputtering or vapour source. The angle between the column axis and the substrate normal (β) is universally observed to be smaller than the angle between source and substrate normal (α), which in our off-axis magnetron geometry is $\alpha = 24°$. These angles are connected by the empirical relation $\tan\beta = 2\tan\alpha$, commonly known as the *tangent rule* [39]. Without rotation, we would observe inclined columns with an angle of approximately 12°, at least on smooth substrates. Angle impingement of sputtered Au films with inclined columnar structure have been presented recently in the literature [64].

The same explanation works well for films grown with gold nanoparticles. Fig.3.6 clearly shows the V-shape of the grains in the first stages of growth before the surviving grains grown until the final occlusion of the pores.

In Fig.3.7 we present front view SEM images of samples from the series ZnOAu-manual grown on Si substrates. The long growth time (3-6 seconds) allows gold to form clusters that are visible on the surface. We think that it is the formation of these clusters that affect negatively the transparence of these samples (see 3.4.1). To avoid the formation of clusters, we tried to space out the gold growth as much as possible, limiting its deposition time to better preserve one of the distinctive characteristics of ZnO: transparency.

On AAM the structure of samples from the series ZnOAu-manual (Fig.3.8) still presents clusters on the surface. The higher deposition rate of gold allows the film to obstruct the pores, although the underlying pattern is still visible in some samples.

SEM imaging of the ZnOAu-pulsed series can be found in Fig.3.9 and Fig.3.10. Only three samples showed gold in the chemical analysis conducted via XPS and X-Ray Fluorescence (see 3.3). These samples have been grown with a pulse frequency of 10Hz and clearly show gold deposition on the surface. The employment of a pulsed plasma deposition did not prevent the formation of clusters; in fact it seems to have favoured it. It is

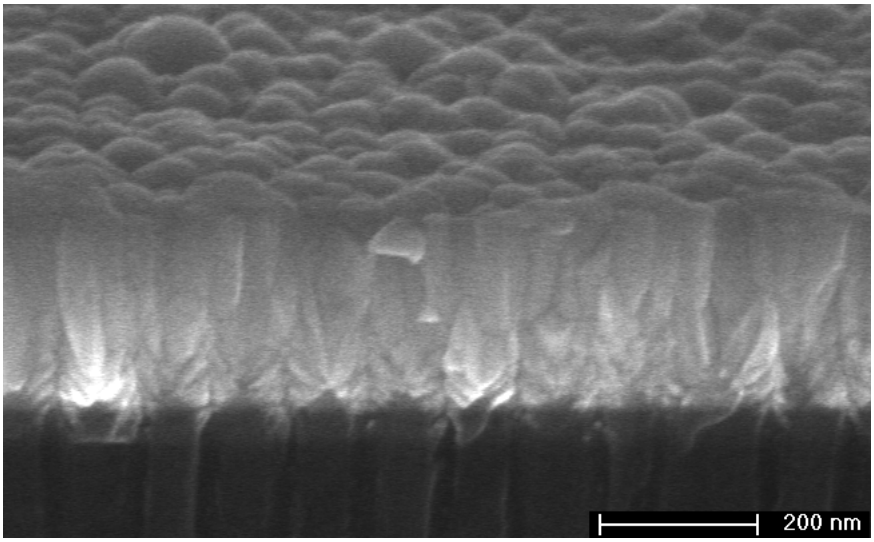

Figure 3.6: SEM cross-view images of sample ZnOAu-1.3 grown on AAM. The V-shape of the grains is clearly visible at the base of the columns.

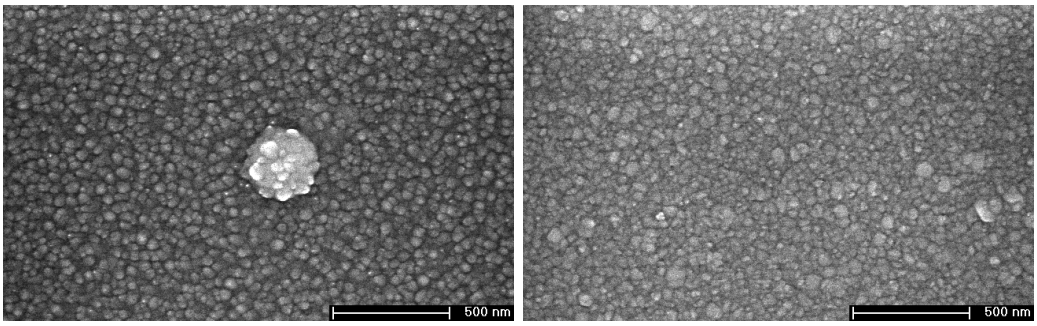

(a) ZnOAu-10.6.54 on AAM **(b)** ZnOAu-5.6.114 on AAM

Figure 3.7: SEM front-view images of the series ZnOAu-manual grown on Si

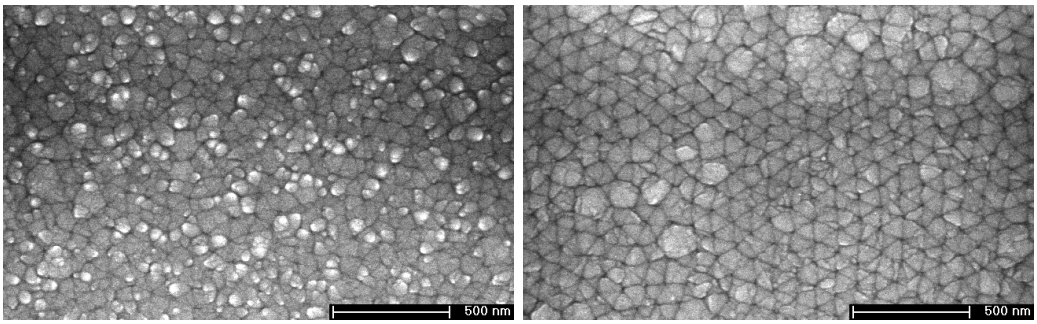

(a) ZnOAu-10.6.114 on AAM **(b)** ZnOAu-5.3.147 on AAM

Figure 3.8: SEM front-view images of the series ZnOAu-manual grown on Si

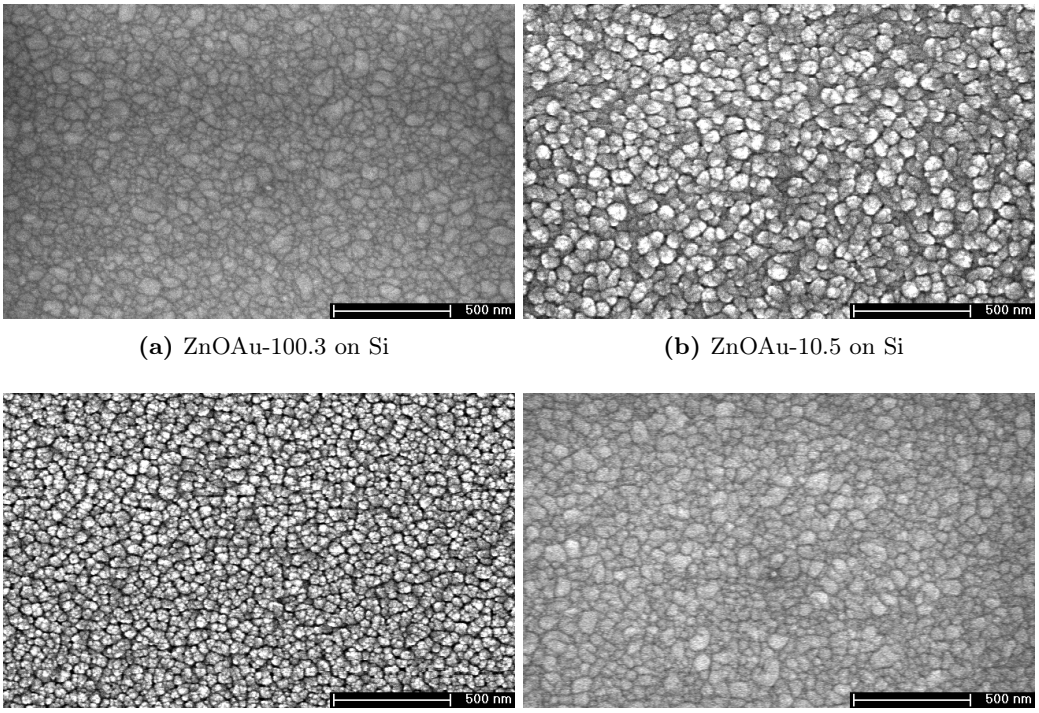

(a) ZnOAu-100.3 on Si **(b)** ZnOAu-10.5 on Si

(c) ZnOAu-10.2 on Si **(d)** ZnOAu-1.5 on Si

Figure 3.9: SEM front-view images of the series ZnOAu-pulsed grown on AAM

possible that the high frequency employed made it easier for the gold to reach the surface in a continuous-like way, allowing for a denser clusterization. All samples show a general increase in grain size and decrease of grain size uniformity with respect to the undoped series.

3.1.1 Thickness

The thickness of the samples was measured with a stylus profiler and via SEM imaging.

An Aluminium-Nickel tape was used to mask a part of the microscope slide glass sample in order to form a well-defined step between the clean glass and the film grown. This step was then used to measure the thickness of the film with Taylor-Hobson Talystep stylus profilometer. Aluminium-Nickel tape was chosen because of its good behaviour in high vacuum conditions.

The profilometer used employs an electromechanical method for measuring RMS roughness and thin film thickness. Vertical movement of the stylus is detected by an inductance transducer and the electrical signal is amplified. The stylus can be traversed at three different speeds and the vertical stylus force can be varied, usually kept at 1-2 mg. According to the manufacturer, this equipment, although outdated, could still reach a noise level of better than 0.7 nm RMS. [84] We could not reach that level of precision because of the irregularities of the grown film near the tape, moreover, film thickness is not uniform but varies with distance from the magnetron focal point, so glass positioning during

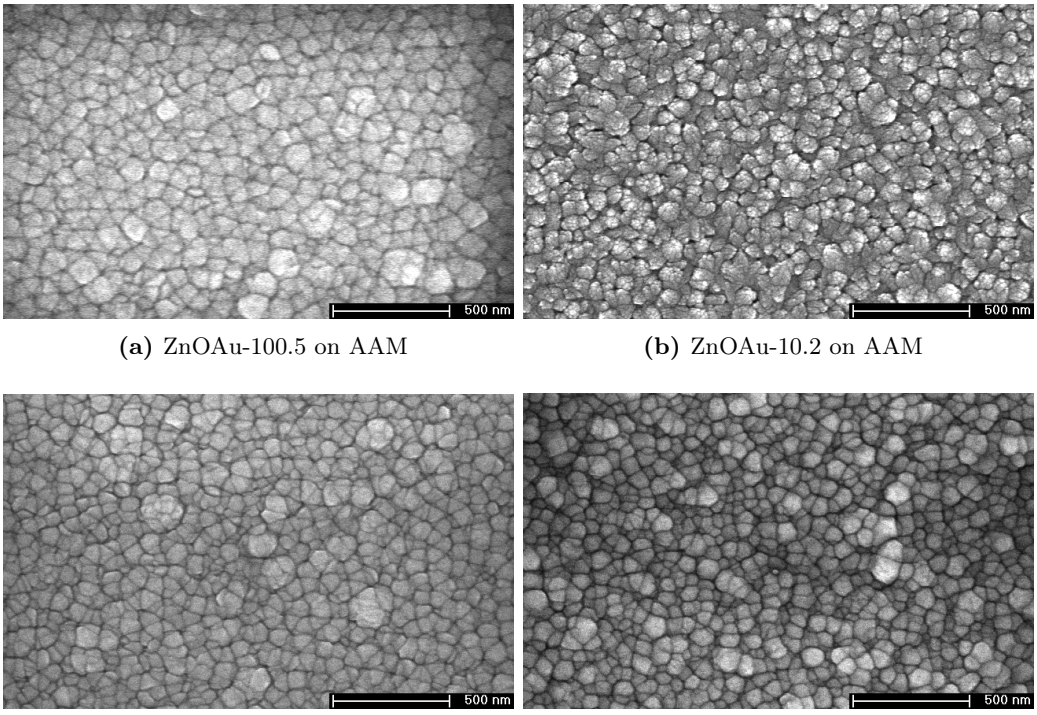

(a) ZnOAu-100.5 on AAM **(b)** ZnOAu-10.2 on AAM

(c) ZnOAu-10.1 on AAM **(d)** ZnOAu-1.1 on AAM

Figure 3.10: SEM front-view images of the series ZnOAu-pulsed grown on AAM

the growth, tape positioning and measurement point choice slightly modify the thickness measure result. Lastly, the sample holder plane horizontality cannot be assured with great precision due to the equipment age. It should be noted that although the measure is quite precise, the effective error on the film thickness is much harder to estimate, for reasons stated above. The standard procedure with this equipment is to give an approximate error of about 10% of the measure.

Additionally, Scanning Electron Microscopy measures allowed us to take pictures of the film. By scratching the sample we obtain small fragments of film with different orientations: if one of this fragments ends up sitting transversally, we can measure the layer thickness. For this operation, substrates of AAO/Al Nanotemplates membranes were employed because of the clearer distinction between substrate and film with respect to other substrates. The measurement process is still tricky and because it is limited to a very small portion of the sample, the result can only be an estimate of the actual film thickness. The error reported for SEM measures in Table **??** is the RMS of repeated measures but, for the reasons explained above, the precision can be estimated to be within ~ 20 nm.

Thickness - ZnO-0-100 series

For the first two samples grown, a ceramic tile was used instead of tape to create the step to be measured, this resulted in a not well defined step and a much less precise measure of layer thickness. The unreliability of the step made with the ceramic tile was the reason

Sample	Profilometry [nm]	SEM [nm]	Inter. [nm]
ZnO-0	220 ± 20*	209 ± 7	≥ 130
ZnO-10	160 ± 20	n.a.	
ZnO-20	110 ± 10	n.a.	
ZnO-30	100 ± 10	223 ± 4	≥ 100
ZnO-50	55 ± 10*	112 ± 5	
ZnO-70	75 ± 8	83 ± 3	
ZnO-100	60 ± 6	88 ± 6	$\simeq 70$

*Step made with ceramic tile.

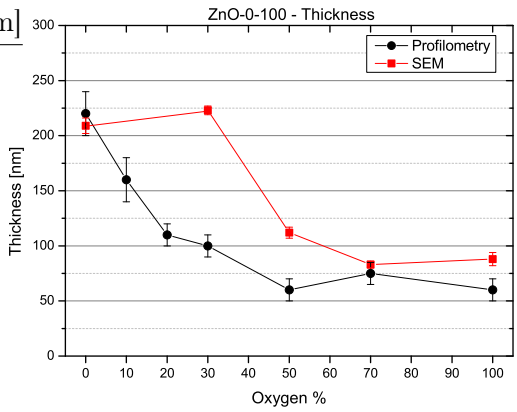

Figure 3.11: Thickness of series ZnO

for switching to tape.

For three of these samples we tried measuring the thickness with a home-built Fizeau interferometer.

We focused a laser ($\lambda = 550$ nm) on the edge between the deposited film and the part of the substrate that, being covered by the screw used to secure it to the sample holder, remained clean. When interference with the source light is observed, the interference patterns shows a phase shift due to the different path length caused by the coating. By measuring the fringes shift between the two diffraction patterns, the difference in path length can be calculated, which in turn yields the thickness of the deposited film. Under optimal conditions this interferometer can reach a precision of $\frac{1}{2}\frac{\lambda}{4} \sim 70$ nm, but was used in this case to give a lower limit to the thickness.

The only notable differences between the two measurement techniques appear for the ZnO-30 and ZnO-50 samples. In future calculations, we will use the values obtained with the profilometer for the former, and the SEM one for the latter. This decision arises both because the selected values are in good agreement with the general trend of the series and because there are reasons (mentioned above) to question the profilometer measure of the ZnO-50 sample. A possible explanation for the SEM measure of the ZnO-30 sample is that the measured film does not sit exactly on the focal plane of the microscope, hence introducing an error. The value obtained is still not entirely explainable with only this effect.

The general trend of the series shows a diminishing of thickness size with greater concentration of oxygen. Just a 10% oxygen in the plasma implies a reduction of the thickness of 30% of the value obtained with pure Ar plasma. This effect has a very simple and widely accepted explanation: oxygen ions have a much lower mass compared to argon ones, hence they reduce the efficiency of the sputtering process which then reflects on the film density and thickness.

Thickness - ZnOAu series

The thickness of the samples from the Au doped ZnO series were measured with the same methods explained earlier.

Sample	Profilometry [nm]	SEM [nm]
ZnOAu-10.6.54	210 ± 20	210 ± 6
ZnOAu-10.6.114	150 ± 20	205 ± 9
ZnOAu-5.6.54	190 ± 20	204 ± 6
ZnOAu-5.6.114	180 ± 20	190 ± 9
ZnOAu-5.3.147	165 ± 20	181 ± 9

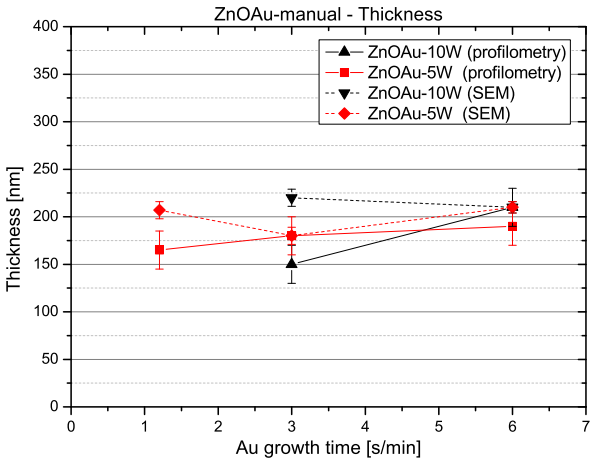

Figure 3.12: Thickness of series ZnO-manual

For this series, discrepancies are to be expected because of the nature of the growing method. For these samples, the Au magnetron was manually shut and opened to limit the gold flux. Manual managing of a magnetron is inherently flawed, especially when referred to something as delicate as microfabrication. Nonetheless, thickness is reasonably constant among these sample, especially if we take into account that the time of growth for gold particles varies considerably between samples. A higher sputtering yield was expected for samples grown with a 10 W power (for the Au magnetron). This prediction was respected by samples grown with 6 seconds of Au growth spaced over a minute, but not by those were the spacing is two minutes. However, the difference is within the error measurement for both techniques. The only significant deviation is noted in sample ZnOAu-10.6.114, and only in the measurements done with the stylus profilometer.

Please note that the two measurement techniques are carried out on different substrates (microscope glass and AAM). Therefore, thickness from the same growth is expected to vary slightly between the two samples because the positioning of the samples was different during deposition and because the film formation on AAM is influenced by the nanohole pattern.

Thickness varies considerably, especially for samples grown with 3% duty cycle, although differences are less remarkable when viewed on the scanning microscope. Overall gold growth time is the same for samples with the same duty cycle, but thickness is significantly different among same-duty-cycle samples grown with different frequencies.

Sample	Profilometry [nm]	SEM [nm]
ZnOAu-100.1	110 ± 10	182 ± 10
ZnOAu-100.2	150 ± 20	192 ± 7
ZnOAu-100.3	220 ± 20	265 ± 12
ZnOAu-100.5	150 ± 20	183 ± 12
ZnOAu-10.1	140 ± 10	251 ± 12
ZnOAu-10.2	260 ± 30	271 ± 8
ZnOAu-10.3	340 ± 30	320 ± 35
ZnOAu-10.5	290 ± 30	299 ± 13
ZnOAu-1.1	245 ± 30	241 ± 19
ZnOAu-1.2	230 ± 20	266 ± 8
ZnOAu-1.3	205 ± 20	251 ± 13
ZnOAu-1.5	240 ± 20	235 ± 9

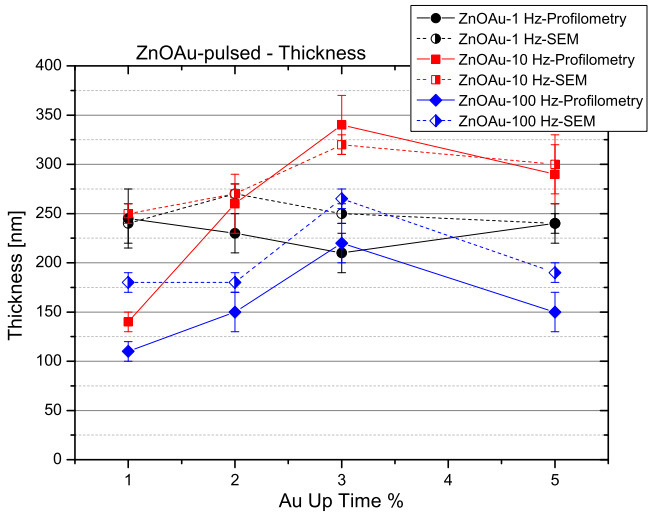

Figure 3.13: Thickness of series ZnOAu-pulsed

3.2 Crystal Analysis

3.2.1 XRD results

From the literature we know that the structure of the ZnO films as revealed by XRD depends strongly on the preparation conditions. Zinc oxide exhibits a very pronounced (0 0 1) texture, that means, the *c*-axis of almost all (hexagonal) zincite crystallites is perpendicular to the substrate surface. However, the extent of the texture, the grain size and the mechanical stress in the films depend significantly on the growth conditions.

Especially at low homologous temperature, crystal structure is strongly influenced by apparatus configuration, substrate surface morphology, and the working gas pressure. These determine the physical processes that occur during film formation and are relevant when the adatom mobility is very low: shadowing, surface and bulk diffusion, and competition of grains and texture. As stated above, the off-axis geometry of the magnetron geometry favours shadowing, which combined with the above factors might lead to a predominance of one crystallographic direction over the others, producing textured coatings.

This is our case, as we can see from Fig.3.14, 3.15 and 3.16 that our samples have a predominant peak in the (0 0 2) direction. The structure is therefore polycrystalline with a preferential direction along the *c*-axis.

The best correspondence of these diffraction patterns was found with references for Zincite (ZnO) with wurtzite structure (COD 96-9011662 [67] and COD 96-900-4180 [68]). All the peaks can be well indexed to the referenced values. It can be clearly seen that samples grown with some percentage of oxygen in the plasma experience a strongly predominant (0 0 2) orientation, while the sample grown at 0% oxygen content, although

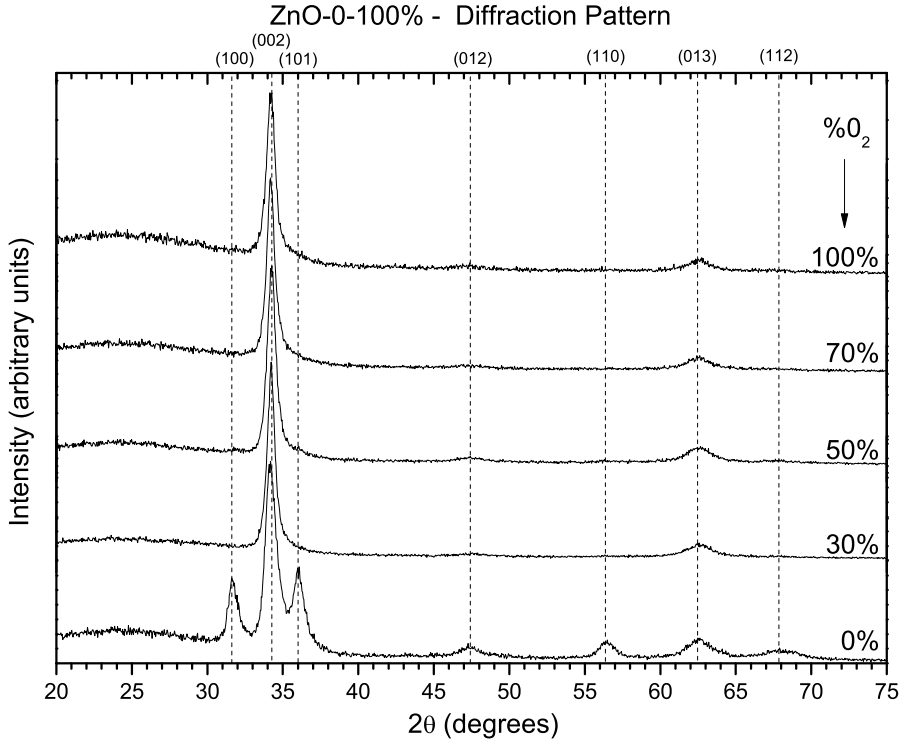

Figure 3.14: Comparison of XRD spectra of ZnO

presenting the same predominant (0 0 2) orientation, shows to other important peaks corresponding to the (1 0 0) and (1 0 1) orientations. Polycrystallinity of the ZnO-0 sample is evident as it is the only sample that clearly shows peaks for the (0 1 2), (1 1 0), (0 1 3) and (1 1 2) directions.

What we observe, however, is in contrast with is reported by Ellmer et al. [85]. They find that for increasing oxygen partial pressure the (0 0 2) peak intensity decreases, the width of the peak broadens and the peak location is shifted to smaller values compared to the reference peak of zincite powder. These variations are attributed to: different grain sizes (broadening, low intensity) and internal compressive strain (peak shift).

In the ZnOAu-manual series (Fig.3.15) the predominance of the (0 0 2) is still clear, although the peak corresponding to the direction (1 0 1) becomes more relevant, while the others become almost irrelevant or undetectable. The best correspondence is still found only with Zincite and no diffraction peak of metal Au or Au-related phase is detected.

Samples from the ZnOAu-pulsed series (Fig.3.16) present the same dominance of the (0 0 2) peak but also show a generally higher disorder in crystalline the structure. Although an arbitrary scale has been used to plot peaks with a similar aspect in order to emphasize their differences in width and position, the lower signal-to-noise ratio indicates a lower intensity of the peak in some of the samples. The lower intensity of the diffraction peaks points towards a lower crystal quality and higher grade of disorder in the structure. Both the decrease in intensity and the increase in width of the diffraction peaks suggest partial amorphization and grain refinement. The poor crystal quality can inhibit the electrical

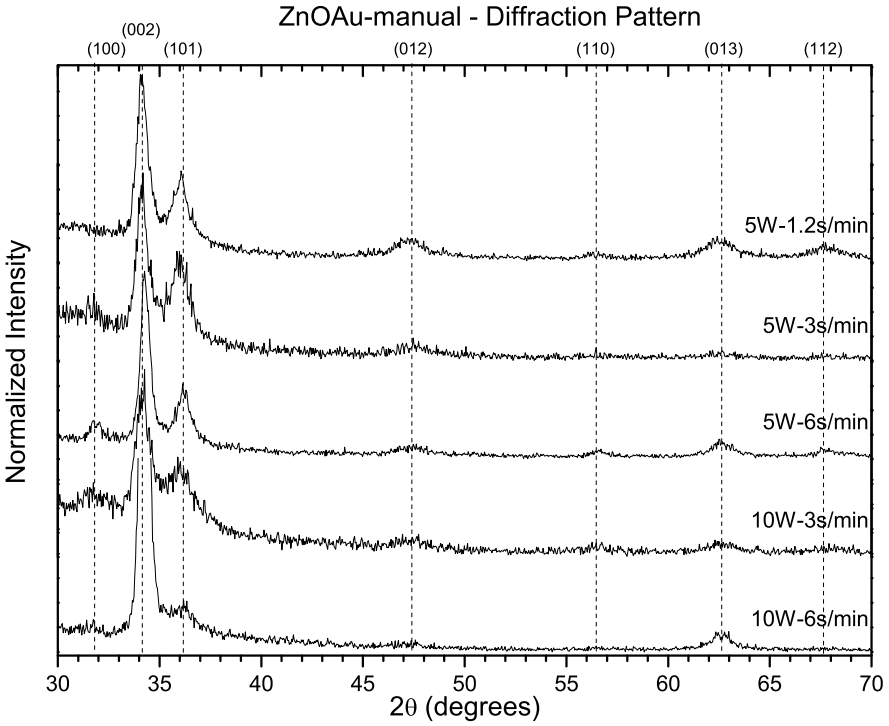

Figure 3.15: ZnOAu-manual series: Comparison of XRD spectra

properties of this samples, as evidenced in 3.5.

Diffraction patterns for all of our samples do not show any peak corresponding to that of metallic Au. The fact that gold nanostructures cannot be detected means that they are very small in size, remaining below ~ 1 nm.

The width of a Bragg peak is affected by the natural broadening, the experimental set-up, the crystal size and the disorder of the crystal structure. The width of the diffraction peaks can be associated to the mean crystal size in nanocrystalline materials: the larger the width, the smaller the crystal size. This will be investigated in 3.2.1.

Van der Drift model

All our samples have a predominant orientation along the *c*. The development of a preferential orientation has been well explained in 1967 by A. Van der Drift [86]. His model proposes that growth velocity anisotropies can lead to competition of grains: some grains grow faster than others because their faces are oriented in the directions favoured by the geometry of the system. For this reason, thickening will result in the eventual occlusion of the other crystals by the ones with favoured textures.

The result of this competition is the occlusion of many small grains at the beginning of the thickening, close to the substrate surface, while the surviving grains are the ones with favoured crystal orientations. Crystal orientations which are more prominent to grow are those that minimize the grain surface energy. This can result in the development of columnar grain structures with parallel boundaries and uniform surface texture, as shown

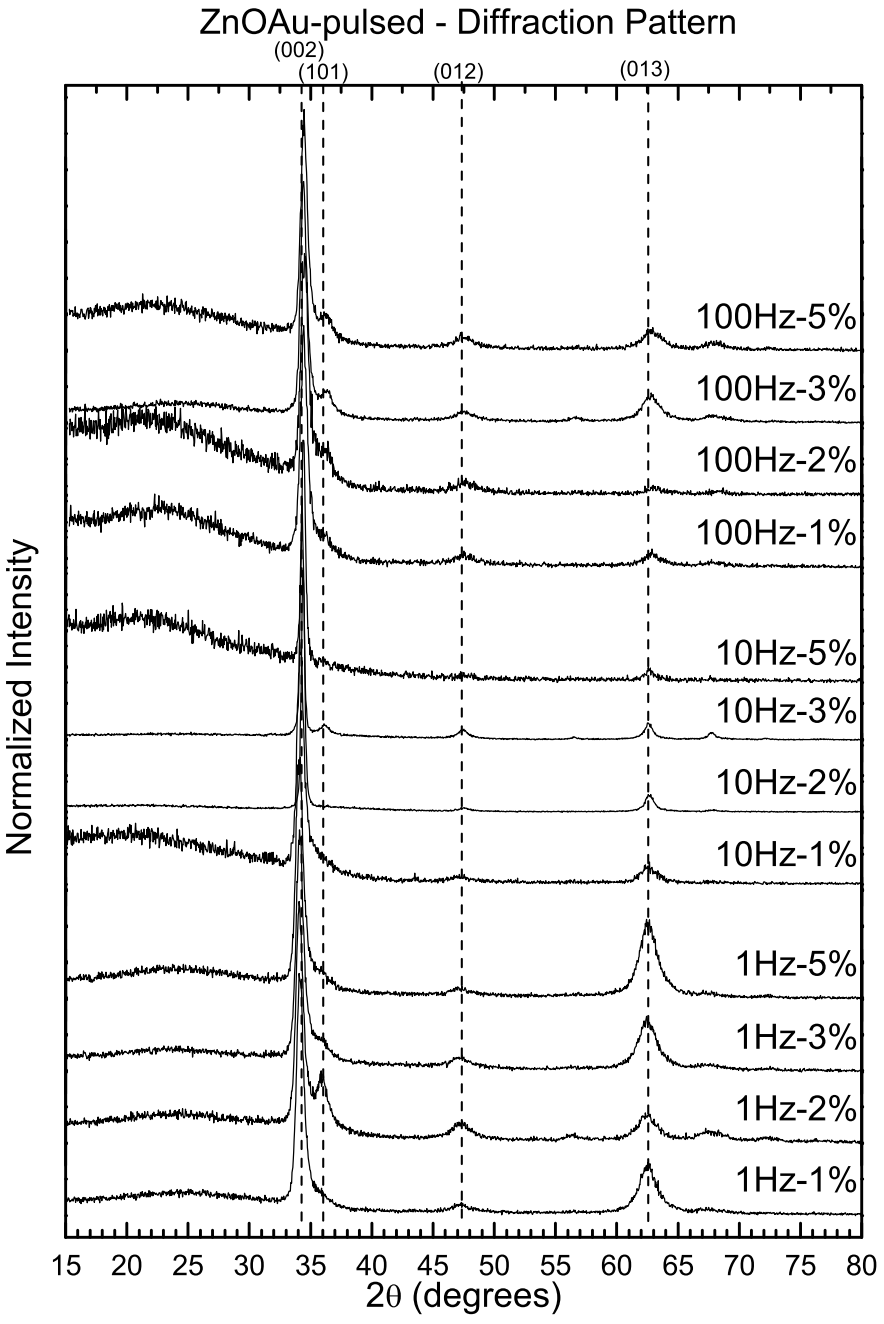

Figure 3.16: ZnOAu-pulsed series: Comparison of XRD spectra

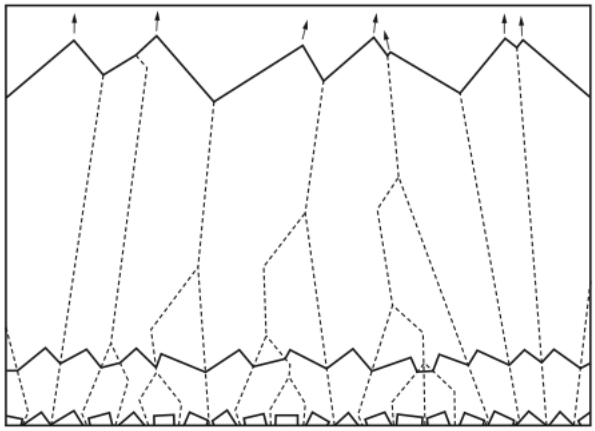

Figure 3.17: Schematic representation of Van der Drift's model: growth velocity anisotropies can lead to competition of grains at the surface of the thickening film and a through-thickness evolution of the in-plane grain size and the average crystallographic texture of the grains at the surface.

schematically in Fig.3.18 [45]

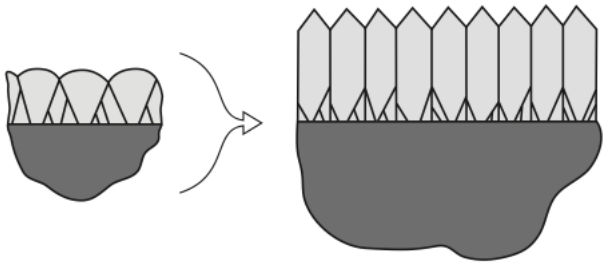

Figure 3.18: If surface grain growth during film thickening is driven by growth velocity, surface energy, or strain energy anisotropy, when all unfavored grains are occluded, further evolution may lead to grains with parallel boundaries, uniform through-thickness sizes, and uniform or restricted textures. (This could lead to *zone 2* structures in the Thornton model.) [45]

With the information obtained from the diffractive pattern we can determine the interplanar separation in the crystalline structure and the crystalline domain size, through Scherrer's equation.

Interplanar separation

The interplanar distance, as determined by the position of the Bragg peaks, is a discontinuous function of the Miller indices ($h\ k\ l$), which identify the crystallographic planes. This distance is related to the unit cell dimensions.

The diffraction pattern of our samples is that typical of a hexagonal wurtzite structure [6] with the following cell parameters [67]:

From these parameters we can obtain the planes separation thanks to eq.3.1 [87] [70]

Table 3.1: ZnO (Zincite) cell parameters

a	3.249 Å	α	90°
b	3.249 Å	β	90°
c	5.207 Å	γ	120°

[88]:

$$\frac{1}{d_{hkl}} = \sqrt{\frac{4}{3}\frac{h^2+hk+k^2}{a^2} + \frac{l^2}{c^2}} \tag{3.1}$$

which yields $d_{002} = 2.6035$ Å.

Crystal domain size

Diffraction patterns were fitted with a Pseudo-Voigt shape, with the understanding that the Gaussian line is due to strain and the Lorentzian is due to particle size effect [72]. The parameters obtained from the fit were used to estimate the crystalline domain size through Scherrer's equation 2.2 Only five samples were analysed because the series was then

Sample	τ [Å]	Fit model
ZnO-0	115 ± 1	Psd-Voigt
ZnO-30	130 ± 10	Psd-Voigt
ZnO-50	110 ± 40	Psd-Voigt
ZnO-70	110 ± 20	Psd-Voigt
ZnO-100	120 ± 30	Psd-Voigt

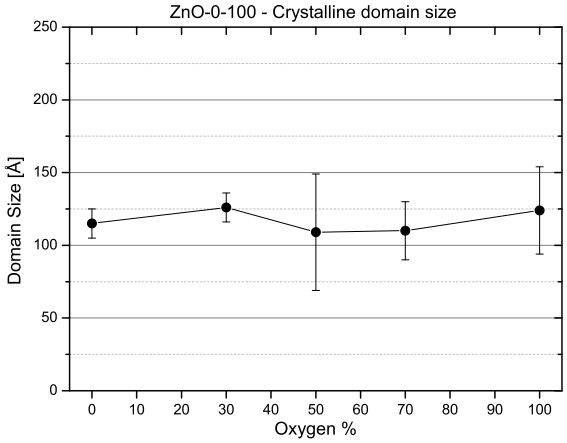

Figure 3.19: Crystalline domain size of series ZnO

interrupted. Nonetheless, we can observe that zinc oxide's grain size does not grows with the content of O_2 in the plasma. This behaviour is in contrast with that of, for example, NiO, whose domain size decreases the more O_2 is present in the plasma during sample fabrication by rf magnetron sputtering [89]. However, it should be noted that Scherrer's analysis relies on the assumption that the system is in ideal conditions and therefore this analysis should be only considered as an indication of a trend.

For ZnOAu-manual series (Fig.3.20) a Lorentzian curve was used to fit the peak instead of a Pseudo-Voigt because the latter yielded inconsistent results. The choice of Lorentzian over a Gaussian was driven by the fact that with samples for which the Pseudo-Voigt was the best fit, the Lorentzian gave results much closer to it than the Gaussian.

Crystalline domain size calculated with the Scherrer formula results much smaller than the average grain size observed with SEM imaging. This is not a concern as SEM reveals

Sample	τ [Å]	Fit model
ZnOAu-10.6.54	180 ± 10	Lorentz
ZnOAu-10.6.114	80 ± 20	Lorentz
ZnOAu-5.6.54	130 ± 10	Lorentz
ZnOAu-5.6.114	120 ± 20	Lorentz
ZnOAu-5.3.147	130 ± 20	Lorentz

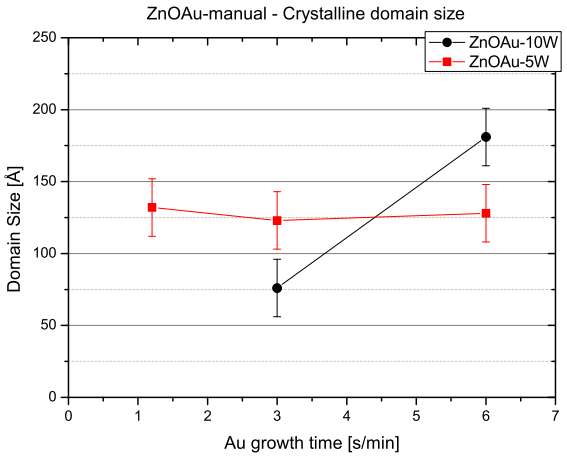

Figure 3.20: Crystalline domain size of series ZnOAu-manual

Sample	τ [Å]	Fit model
ZnOAu-100.1	100 ± 10	Lorentz
ZnOAu-100.2	90 ± 10	Lorentz
ZnOAu-100.3	130 ± 10	Lorentz
ZnOAu-100.5	110 ± 10	Lorentz
ZnOAu-10.1	150 ± 10	Psd-Voigt
ZnOAu-10.2	240 ± 20	Psd-Voigt
ZnOAu-10.3	240 ± 20	Psd-Voigt
ZnOAu-10.5	220 ± 20	Psd-Voigt
ZnOAu-1.1	100 ± 10	Lorentz
ZnOAu-1.2	80 ± 10	Lorentz
ZnOAu-1.3	95 ± 10	Lorentz
ZnOAu-1.5	75 ± 10	Lorentz

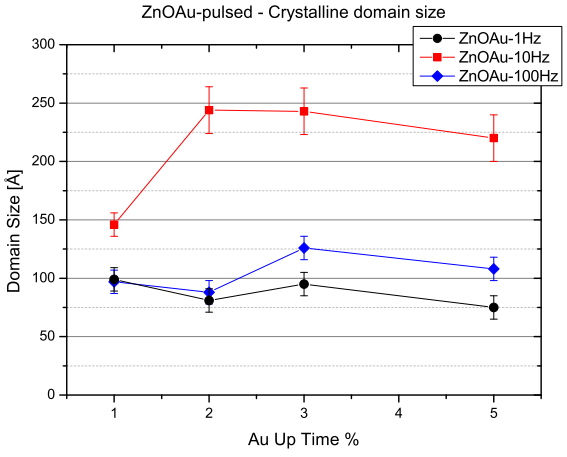

Figure 3.21: Crystalline domain size of series ZnOAu-pulsed

the physical particle size while XRD reveals the structural coherence length (crystallite length perpendicular to the reflecting plane). If film particles are polycrystalline then it is very common that Scherrer estimate results smaller than the size obtained by SEM measurements. Also, particle agglomeration may introduce difficulty in measuring particle size by SEM [90].

3.3 Chemical Analysis

Chemical composition of the samples was analysed with X-Ray Photoelectron Spectroscopy (XPS) and Total X-Ray Fluorescence (TXRF).

3.3.1 X-ray Photoelectron spectroscopy (XPS)

ZnO series - XPS results

The surveys were made with a 50 eV pass energy and a step of 1 eV, while the rest of the regions were made with a step of 0.1 eV and a 20 eV pass energy. This allowed us to obtain a chemical sensitivity in the parts per thousands range. [73] The source used is a twin-anode source (model number: XR3E2), with Mg and Al anodes (Mg Kα =1253.6 eV, Al Kα =1486.6 eV) radiations. The Mg anode was used for all the samples presented in this work. We operated mostly with a 0°take-off angle (x-ray incidence perpendicular to the sample surface). The charge correction has been made using the C 1s peak as reference (Binding energy: 284.50 eV [91]).

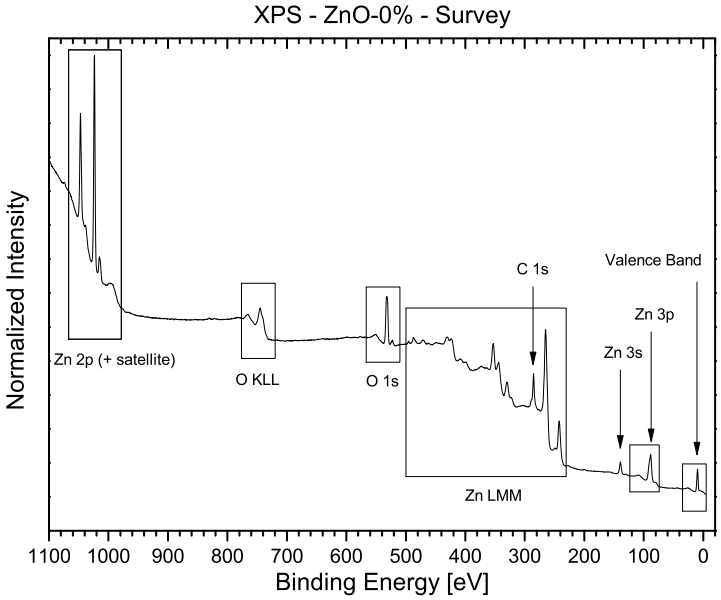

Figure 3.22: Typical XPS spectrum of ZnO

We present a typical XPS spectrum for our samples in Fig.3.22. All the peaks can be easily identified and have a good correspondence with the referenced values found with NIST XPS Database [92]. Spectra show no traces of impurities, the C 1s peak is originated by atmospheric contamination and is used as a reference for charge correction because its position is very stable.

The ratio between oxygen and zinc can be obtained by fitting the O 1s and Zn $2p_{3/2}$ peaks and calculating the ratio of their areas, after considering the different atomic sensitivity factors. The O 1s peak can have many sources and it is important to distinguish between that coming from ZnO and that due to atmospheric contamination, since consider-

ing the latter would give an inconsistent O:Zn ratio. Oxygen forming ZnO has a distinctive energy of 530.40 eV [93] and can therefore be told apart from the one due to atmospheric contamination, which usually forms compounds with carbon atoms.

In an interesting study, Carcia [6] reports that a stoichiometric ratio of O:Zn inhibits the electrical properties of ZnO (see 3.5). Our results corroborate this hypothesis, as we found that if some oxygen is present in the plasma during the growth, the O:Zn ratio is stoichiometric (or very close to it) and corresponds to non-conductive samples. The imbalance between oxygen and zinc suggests that for our samples the electrical conductivity is due to Zn ions [94].

Atomic Sensitivity Factor [95]	
O 1s	0.66
Zn $2p_{3/2}$	4.8

Sample	O:Zn ratio
ZnO-0	0.74 ± 0.1
ZnO-30	0.99 ± 0.1
ZnO-50	1.08 ± 0.1
ZnO-70	1.10 ± 0.1
ZnO-100	1.11 ± 0.1

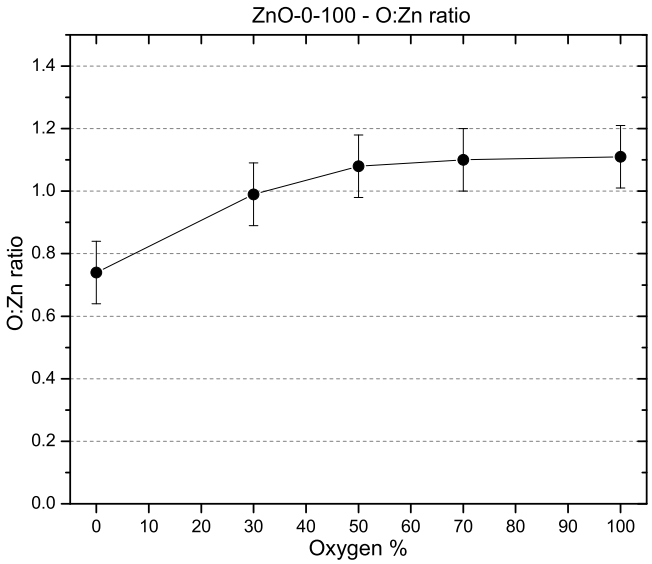

Figure 3.23: ZnO series: O:Zn ratio

It is interesting to notice how the O 1s peaks change in relative intensity if any oxygen is put into the chamber (Fig.3.24): the atmospheric O 1s peak is greatly reduced to only a quarter of the oxygen coming from ZnO. The fact that the increase in one peak with respect to the other is even more clear in the sample ZnO-10 and ZnO-20, which were analyzed with XPS several weeks after deposition. They have been excluded from the fit (Fig.3.25) because the difference with the other peaks makes them not comparable.

The characteristic regions of our samples are those that contain the Zn 2p and Zn 3p peaks. The Zn 2p region presents two distinct peaks which correspond to orbitals Zn $2p_{1/2}$ (BE=1046.5 eV) and Zn $2p_{3/2}$ (BE=1023 eV). The weak structure between these two peaks is the satellite of the Zn $2p_{1/2}$ peak. The Zn 3p region presents two peaks that overlap in the 84-96 eV range. Fitting these region we can see that the two peaks correspond to orbitals Zn $3p_{1/2}$ BE=91.3 eV and Zn $3p_{3/2}$ BE=88.6 eV. These values, that are slightly different from those of metallic Zn, correspond to the Zn^{2+} ion.

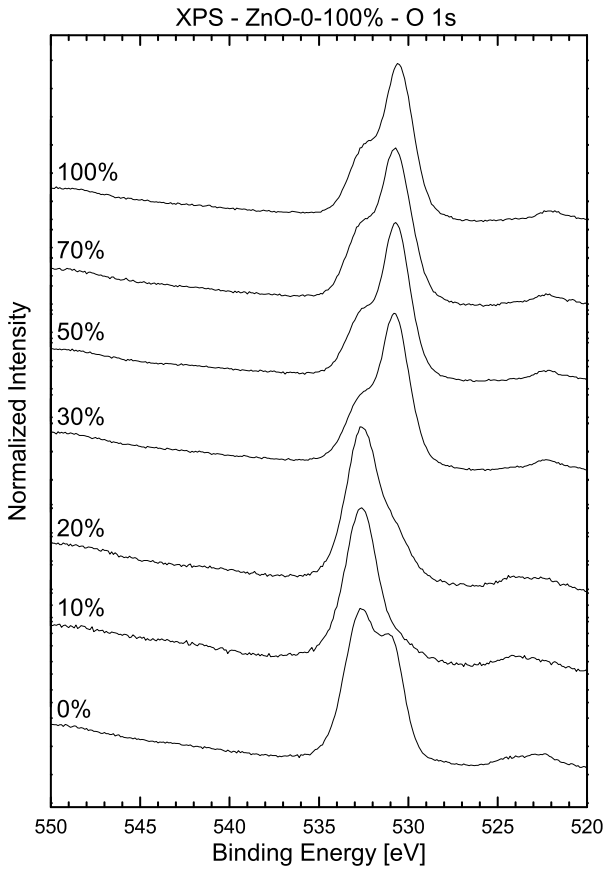

Figure 3.24: ZnO series: O 1s XPS spectra

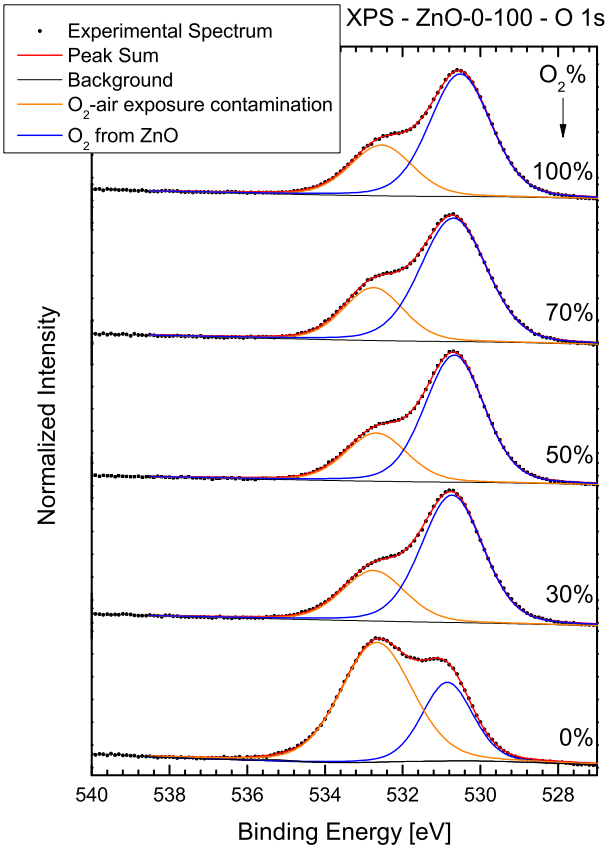

Figure 3.25: Fitting of the O 1s XPS spectra

ZnOAu series - XPS results

Experimental conditions were preserved from the precedent series and can be found in 3.3.1. A typical XPS spectrum of Au doped ZnO is presented in Fig.3.28. Again, the spectrum shows no trace of impurities apart from the carbon due to the atmospheric contamination that is inevitable as samples have to be exposed to open air while being transferred from the deposition chamber to the XPS apparatus (*ex-situ* measurements). At first glance, ZnO and doped ZnO present very similar survey spectrum. That is because photoelectron peaks from the Zn 3p and Au 4f lines have similar energies, and the Au 4d peaks fall into the Auger LMM group of zinc oxide. The peak present at $\sim$ 1014 eV is not one from the gold ANN Auger group because it's too narrow. It is a satellite peak of the Zn 2p group. Therefore, data for these samples are not require fitting for proper interpretation. Fits can be found in Fig.3.29 and Fig.3.30

Fitting the peaks in the 100-80 eV area reveals the presence of gold in all samples from the manual series, on the contrary, only three samples from the pulsed series present gold, and only for a frequency of 10 Hz. An example of these can be seen in Fig.3.31. Peaks Zn $3p_3/2$ and Au $4f_5/2$ overlap to form a higher peak. On the right (lower binding energy) of the main structure we can see the satellite structure due to Kα_3 and Kα_4 of our Mg source. Fitting this region locates the Au $4f_{5/2}$ peak at 87.2 eV and the Au $4f_{7/2}$ at 83.8

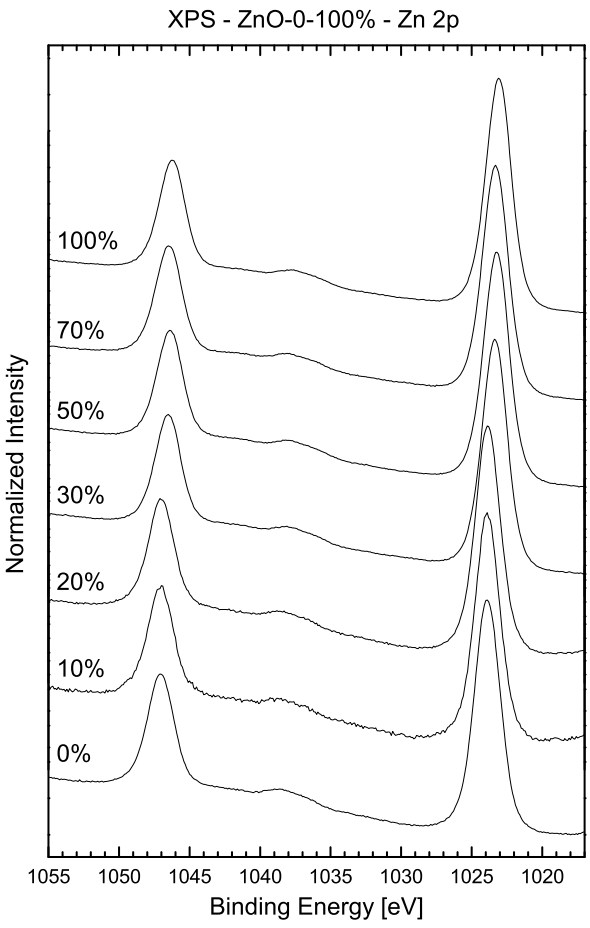

Figure 3.26: ZnO series: Comparison of Zn 2p peaks

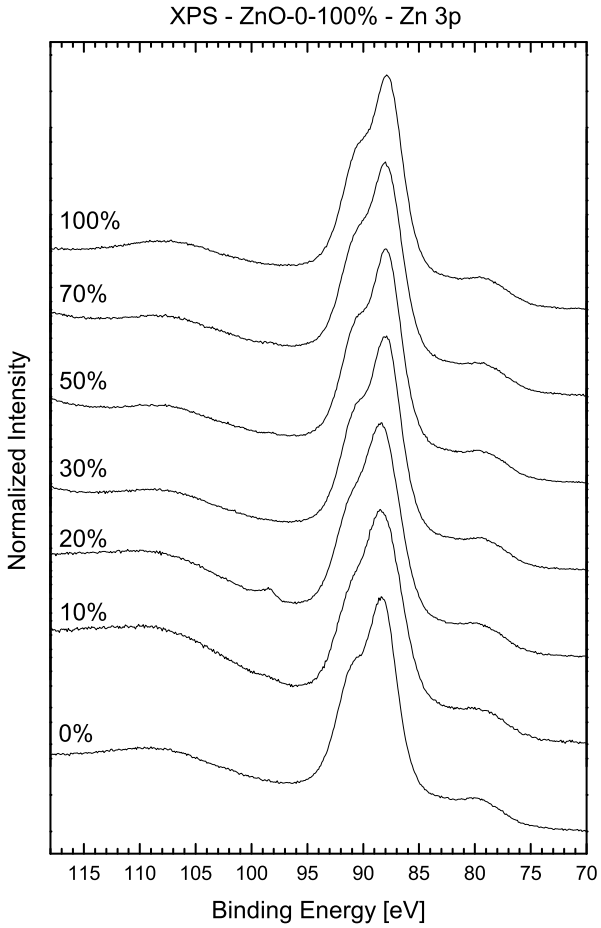

Figure 3.27: ZnO series: Fit comparison of Zn 3p peaks

eV, which correspond to the Au^{1+} ion, suggesting that Au exists in the univalent state and substitute for Zn in the structure [96] [97].

Another interesting feature is observed in the comparison between the valence band of samples of the doped series (Fig.fig:ZnOAuM-XPS-VB and Fig.fig:ZnOAuP-XPS-VB). We can observe that all samples from the ZnOAu-manual series show a peak in the 2-5 eV region, while most of the one from the ZnOAu-pulsed series do not. The only samples from this series that do show this peak are the ones for which we have registered the presence of gold (ZnOAu-10.2-5). This peak shows that there are some electrons close to the Fermi level, and are therefore available for electrical conduction. Therefore, we expect these samples to have better electrical properties than the others, but we will see in 3.5 that this is not our case.

By fitting the Zn 3p and Au 4f peaks, we can calculate the relative ratio between gold and zinc. Taking into account the different cross section to the X-Rays emitted by our source, we can weight the peak intensity to yield an estimate of the quantity of the element detected. The results are presented in Tab.3.2 and confirm that no gold could be detected on the vast majority of the samples. Absence of gold from these samples is confirmed by

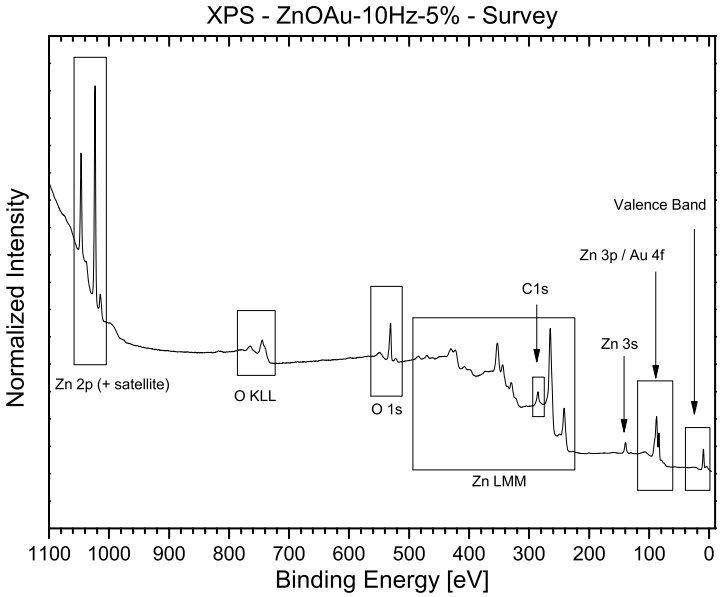

Figure 3.28: Typical XPS spectrum of Au doped ZnO

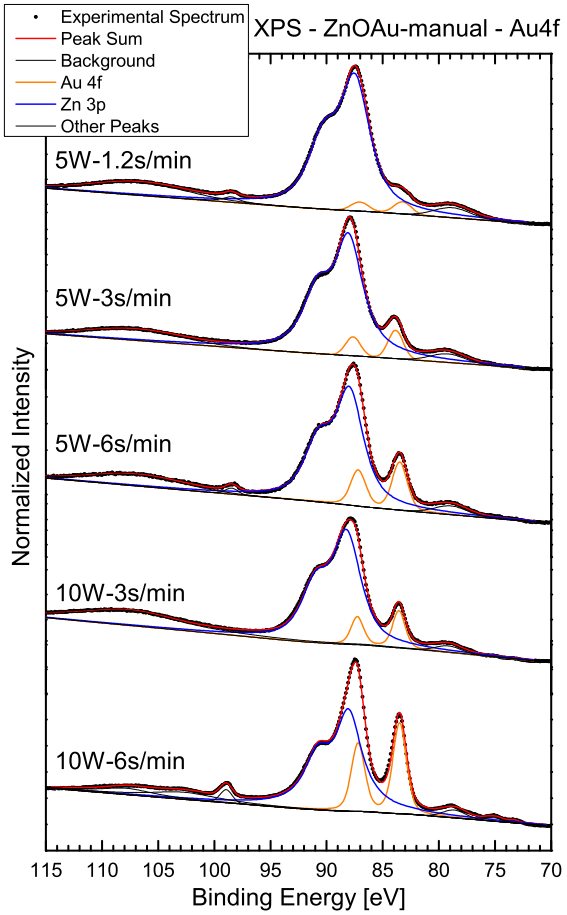

Figure 3.29: ZnOAu-manual series:Au4f fit

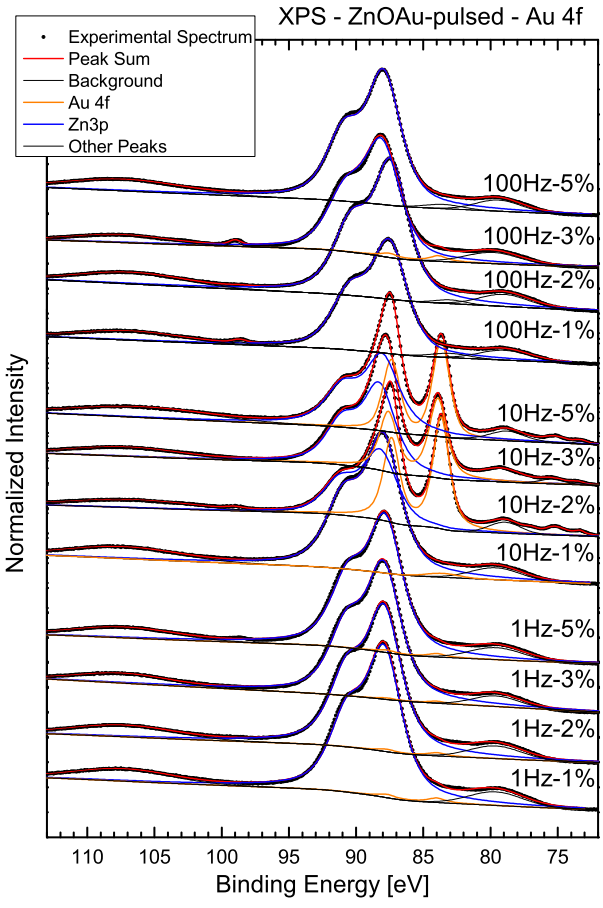

Figure 3.30: ZnOAu-pulsed series:Au4f fit

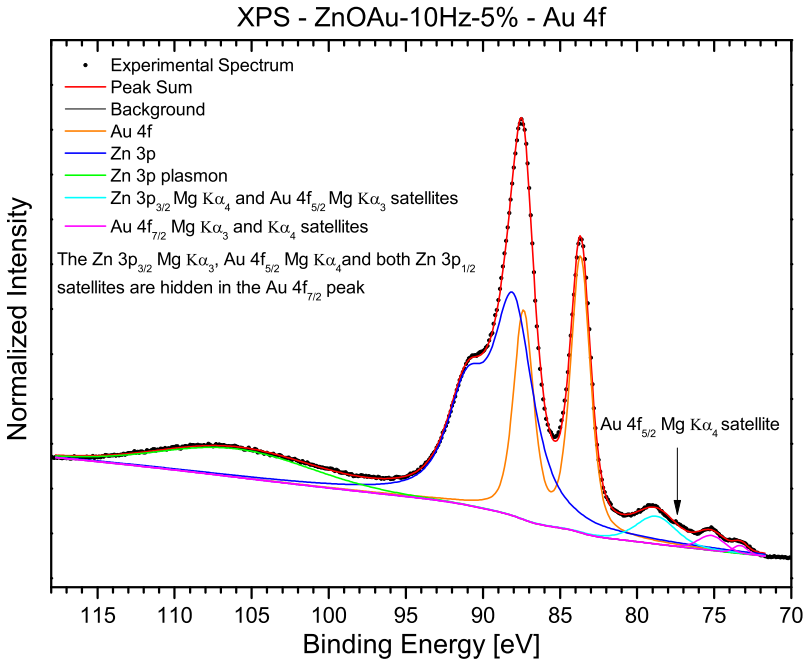

Figure 3.31: Typical XPS spectrum of fitted Au4f peak

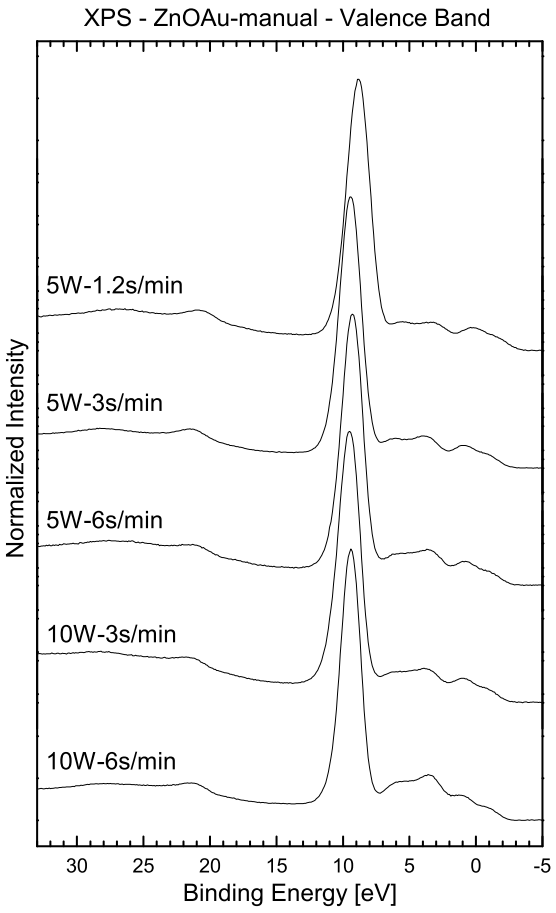

Figure 3.32: ZnOAu-manual series: Valence Band

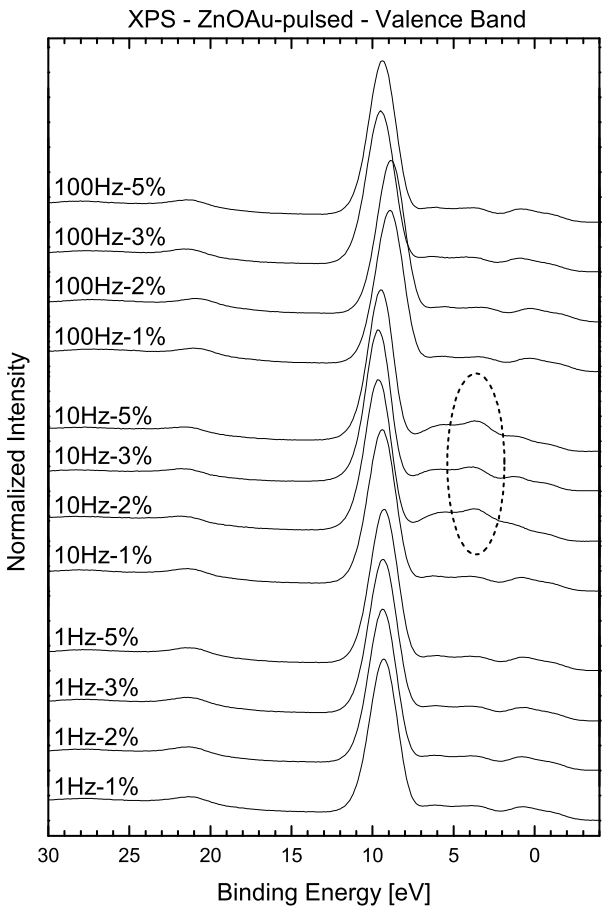

Figure 3.33: ZnOAu-pulsed series: Valence Band

Table 3.2: ZnOAu series: Au:Zn ratio measured with XPS

Atomic Sensitivity Factor [95]			
Au 4f	4.95		
Zn 3p	0.75		
Sample	Au:Zn ratio	Sample	Au:Zn ratio
ZnOAu-10.6.54	0.07 ± 0.01	ZnOAu-10.2	0.16 ± 0.01
ZnOAu-10.6.114	0.02 ± 0.01	ZnOAu-10.3	0.10 ± 0.01
ZnOAu-5.6.54	0.04 ± 0.01	ZnOAu-10.5	0.10 ± 0.01
ZnOAu-5.6.114	0.02 ± 0.01		
ZnOAu-5.3.147	0.01 ± 0.01		

the distinct difference in transmittance (see 3.4.1), but not by the electrical properties (see 3.5).

3.3.2 X-Ray Fluorescence

Au doped ZnO samples from both the ZnOAu-manual and ZnOAu-pulsed series were analyzed with x-ray fluorescence. Films deposited on microscope glass were dissolved with hydrochloric acid which is then eliminated through evaporation on a quartz substrate. The resulting solution was analyzed with the K radiation of a Mo x-ray source.

Results confirm the absence of any relevant contamination in our samples already noted with XPS. With little calculation we can obtain the relative concentration of gold with respect to zinc. Results are in good agreement with those obtained from XPS measurements,

Table 3.3: ZnOAu series: Au:Zn ratio measured with x-ray fluorescence

Sample	Au:Zn ratio	Sample	Au:Zn ratio
ZnOAu-10.6.54	0.057 ± 0.01	ZnOAu-10.2	0.087 ± 0.01
ZnOAu-10.6.114	0.028 ± 0.01	ZnOAu-10.3	0.066 ± 0.01
ZnOAu-5.6.54	0.081 ± 0.01	ZnOAu-10.5	0.051 ± 0.01
ZnOAu-5.6.114	0.010 ± 0.01		
ZnOAu-5.3.147	0.004 ± 0.01		

showing the same trend of gold concentration for the ZnOAu-manual series. However, for the ZnOAu-pulsed series, Au concentration seems to be increasing with the diminishing of the duty time, which is counterintuitive and should need further investigation. Comparison of chemical results obtained with TXRF and XPS is showed in Fig.3.34.

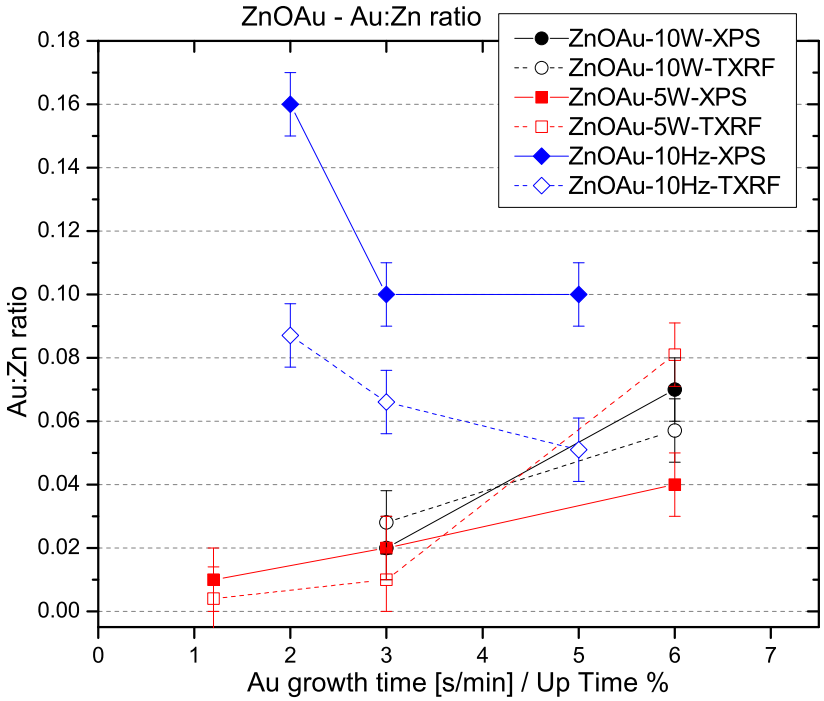

Figure 3.34: ZnOAu series: Au:Zn ratio

3.4 Optical Properties

We used two different techniques to investigate the optical properties of our samples. UV-VIS spectrophotometry was used to measure the transmittance values and the band gap of our samples. Ellipsometry was used to obtain the refractive index n and the extinction coefficient k, as well as confirm other measures.

3.4.1 UV-VIS Spectrophotometry

In optics and spectroscopy, transmittance is the fraction of incident light at a specified wavelength that passes through a sample. In thin film physics optical properties change rapidly, especially if metal nanoparticles are involved. Substrates were analyzed in the UV-VIS range (250-800 nm) with a *Jasco V-560* UV-VIS spectrophotometer.

Transmittance

Transmittance results of samples from the ZnO-0-100 series are presented in Fig.3.35. All samples show good transmittance in the visible region as the registered value is above 80% across the whole region. The sharp cut in transmittance due to the glass (present in the graph as a reference) happens at ∼330 nm and does not influence the validity of the measurement as the loss of transparence of ZnO happens at higher wavelengths. The only sample that stands out is ZnO-100, which shows a constant negative trend from 800 to 400 nm and crosses the 80% transmittance level at 550 nm. A similar transmittance has previously been obtained in an analogous work by A. Patra [98]. However, we notice

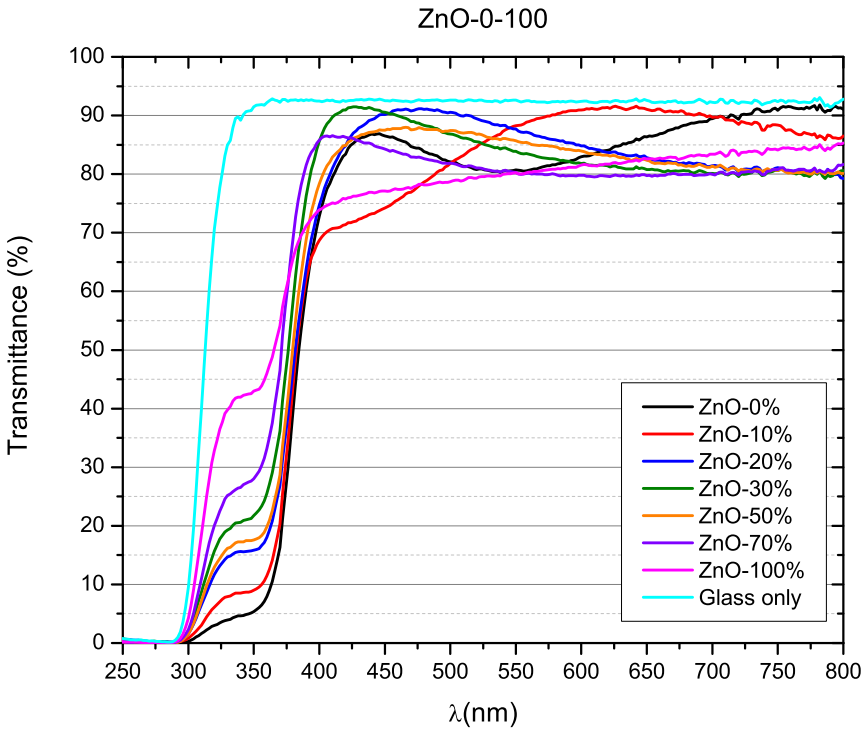

Figure 3.35: UV-VIS spectra for the ZnOAu series

a significant difference between our samples in the near infrared region of the spectrum. Samples grown with more oxygen in the plasma show higher transmittance in the 370-330 nm region and the transmittance is higher the more oxygen was present in the plasma. While transmittance in this region is only $\sim 5\%$ for the ZnO-0 sample, the one grown with a 100% oxygen plasma shows a transmittance of $\sim 40\%$.

The introduction of gold nanoparticles greatly modifies the transmittance of the samples from series ZnOAu-manual (Fig.3.36). Only the two samples with the least amount of gold (ZnOAu-5.6.114 and ZnOAu-5.3.147) show a transmittance pattern that resembles that of undoped samples, the transmittance, however, is higher than 75-80% only for wavelengths greater than 600 nm. The other samples show a very steep decay across the whole spectrum and struggle to reach a transmittance of 60%, with one sample not reaching even 30%.

Transmittance measurements for the ZnOAu-pulsed series (3.37) seems to confirm the absence of gold resulting from chemical measurements 3.3. The three samples that present gold have a transmittance comparable with that of samples from the ZnOAu-manual series, i.e. a negative trend across the whole spectrum and a top value registered at 800 nm that in only one sample reaches 70% but is otherwise below 50%. The ZnOAu-10.1 sample, that does not present gold with chemical analysis, has a completely different transmittance pattern that is similar to that of samples grown with a frequency of 100 Hz for the Au magnetron. Among this series, though, sample ZnOAu-100.5 shows a pattern that follows

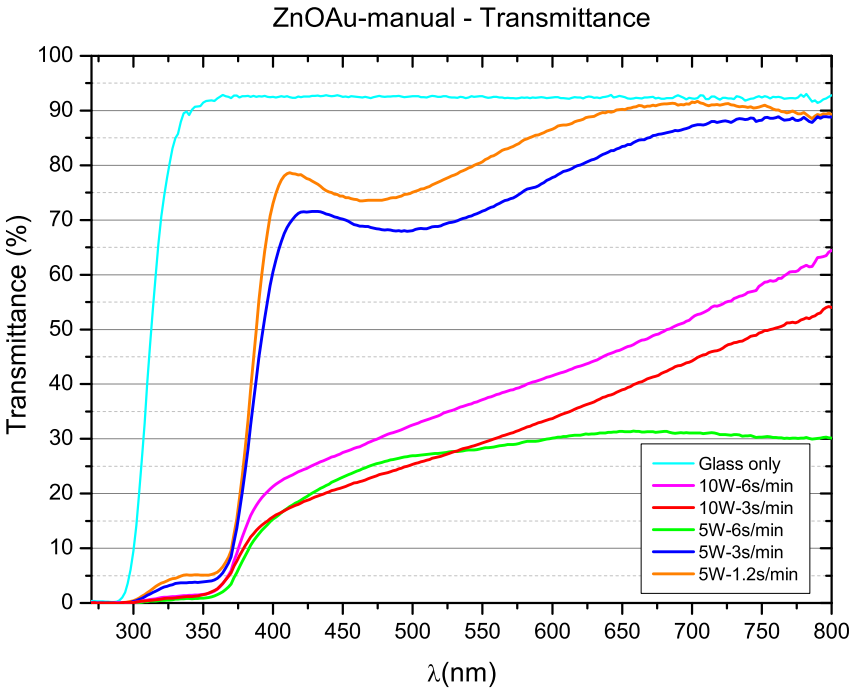

Figure 3.36: UV-VIS spectra for the ZnOAu-manual series

that of samples grown at 1Hz frequency. The reason for these outliers in the series is not clear and cannot be explained by difference in crystal size or in the structure observed through SEM imaging.

Determination of Band Gap

From the transmittance of our samples we calculated their absorbance at each wavelength and built the correspondent Tauc Plot. These plots present a sudden fall, which is the part corresponding to the band gap and is the part that we fitted. The intersection between the fit and the $y = 0$ axis yields the band gap value. A representative Tauc plot is presented in Fig.3.38. Results are presented in Tab.3.39.

The band gap of our samples does not vary a lot within the same series. We notice a small difference between the undoped series and the ZnOAu-manual series, which suggests that Au doping would lower the band gap. In fact, under similar conditions, Xu et al. [99] observe that the band edge of the ZnO:Au is smaller than that of the ZnO at the same preparation conditions, and attribute this to the dopant effect of Au. The explanation they give is that when an Au atom occupies a Zn site, a strong p-d coupling between Au and O occurs that moves the O 2p level up and narrows the direct fundamental band gap. Therefore, the band-gap of the ZnO:Au they find is smaller than that of the ZnO. However, we cannot assert the same as the variation is very small and our measures rely on the precision of the measurement of the film thickness, which we already showed is tied to about 10% of the layer thickness itself. A direct measurement of absorbance, instead of transmittance, might improve this measurement. Moreover, the samples with reported Au

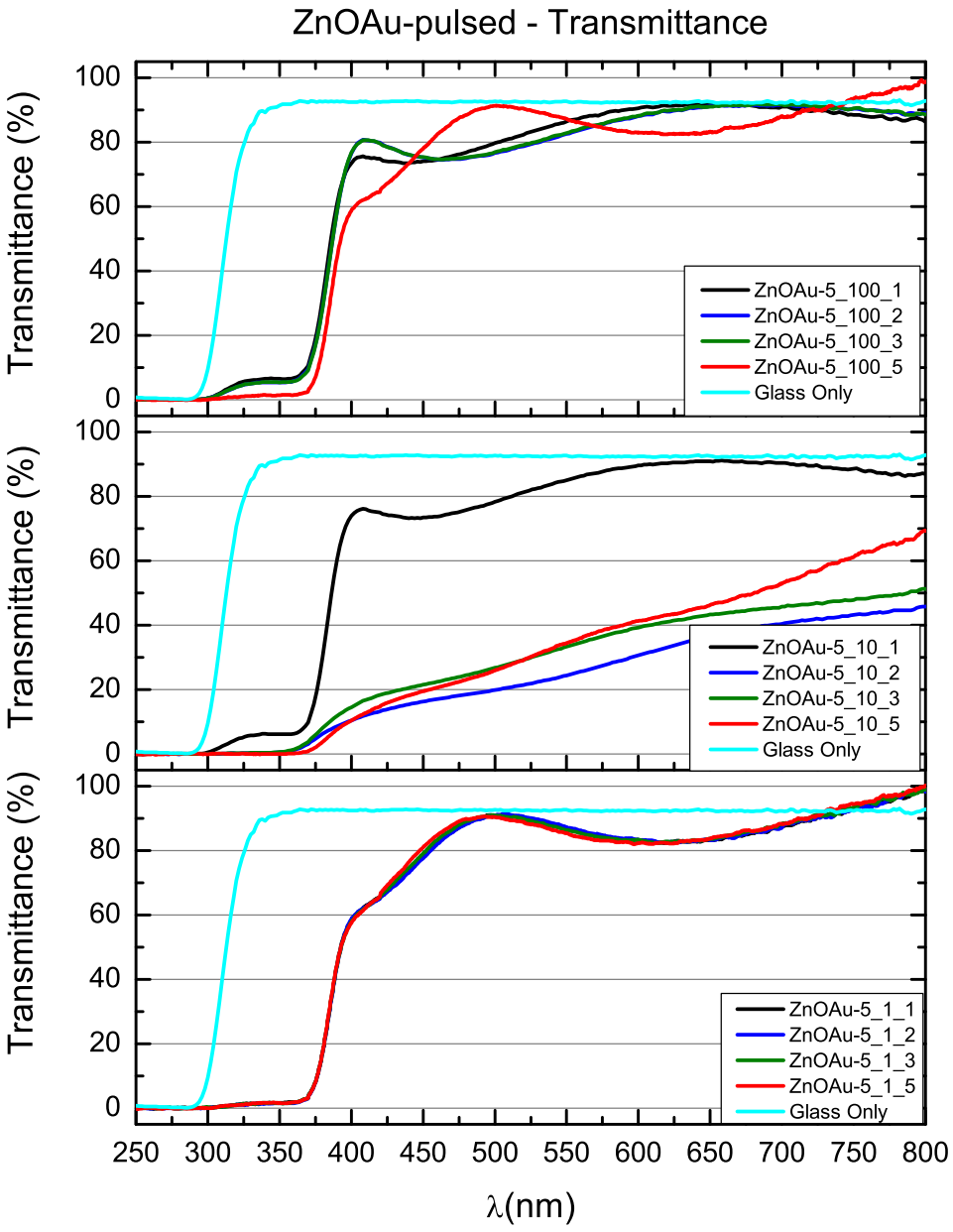

Figure 3.37: UV-VIS spectra for the ZnOAu-pulsed series

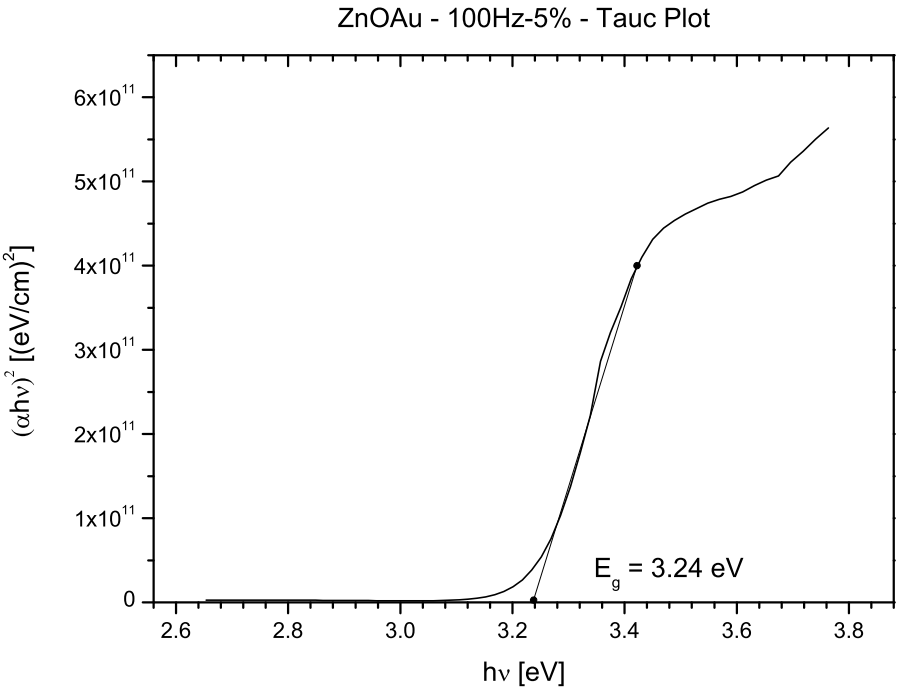

Figure 3.38: Example of Tauc Plot (Sample ZnOAu-100.5)

Sample	E_{gap}
ZnO-0	3.28 ± 0.03
ZnO-10	3.27 ± 0.03
ZnO-20	3.25 ± 0.03
ZnO-30	3.26 ± 0.03
ZnO-50	3.25 ± 0.03
ZnO-70	3.28 ± 0.03
ZnO-100	3.23 ± 0.03

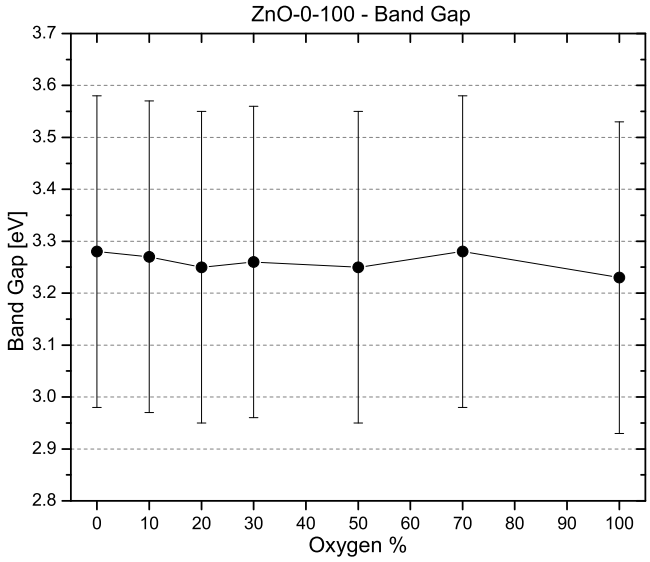

Figure 3.39: ZnO series: Band Gap

Sample	E_{gap}
ZnOAu-10.6.54	3.24 ± 0.03
ZnOAu-10.6.114	3.22 ± 0.03
ZnOAu-5.6.54	3.22 ± 0.03
ZnOAu-5.6.114	3.24 ± 0.03
ZnOAu-5.3.147	3.24 ± 0.03

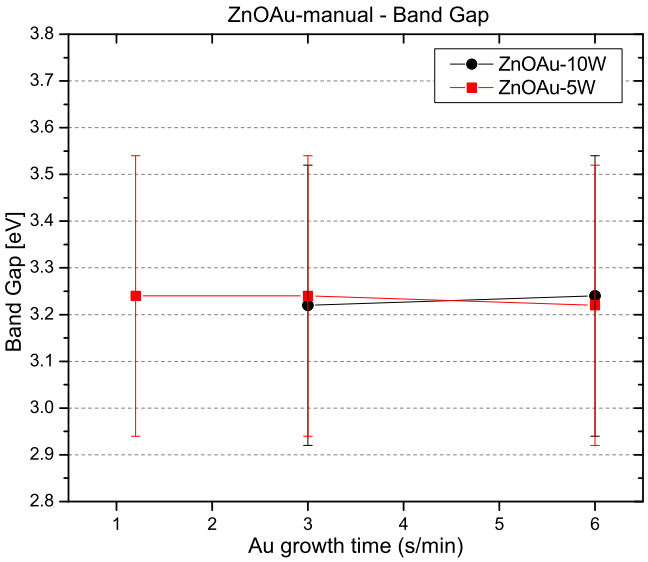

Figure 3.40: ZnOAu-manual series: Band Gap

deposition from the ZnOAu.10Hz series show a band gap almost identical to the undoped ones, while the ones that do not appear to have gold with chemical analysis have band gaps comparable to those of the ZnOAu-manual series.

In the same paper [99], Xu et al. report the presence of a small absorption peak at 2.0-2.4 eV in the absorption spectra of the ZnO:Au annealed at a temperature range of 600-800 °C, and see that its intensity increases with increasing annealing temperature. They explain the small peak as an effect of the local surface plasmon resonance (LSPR) absorption of Au deposited on ZnO. However, we do not observe such a peak as our samples were not annealed.

3.4.2 Ellipsometry - Experimental results

Ellipsometry measures were carried out on three different substrates: Menzel-gläser glass, Si, SiO_2. Four different models were tested for each sample: absorbing/transparent film with/without back reflection. We report only the best model for each series, as different model give consistent but slightly different results. There is usually little differences between models that consider the presence of back reflection and those that do not, but former is usually better. The best fits were obtained assuming only one reflection on the back, with fitted intensity. Thickness was generally left as a fitted parameter and can be used as a confirmation of other measurement techniques. In some cases thickness had to be imposed to obtain the best fit. A realistic model of thin film structure is required to determine the optical constants of the film material. During the investigation, we found that the model containing a roughness layer could significantly improve the fitting result, so the three-layer structure model shown in Fig.3.42 were finally chosen.

Measurement were taken with the J.A. Woollam α-SE ellipsometer, fitting was carried out with the dedicate software *Complete EASE*. By minimizing the RMSE, we obtained

Sample	E_{gap}
ZnOAu-100.1	3.24 ± 0.03
ZnOAu-100.2	3.24 ± 0.03
ZnOAu-100.3	3.25 ± 0.03
ZnOAu-100.5	3.24 ± 0.03
ZnOAu-10.1	3.27 ± 0.03
ZnOAu-10.2	3.26 ± 0.03
ZnOAu-10.3	3.30 ± 0.03
ZnOAu-10.5	3.27 ± 0.03
ZnOAu-1.1	3.24 ± 0.03
ZnOAu-1.2	3.24 ± 0.03
ZnOAu-1.3	3.25 ± 0.03
ZnOAu-1.5	3.25 ± 0.03

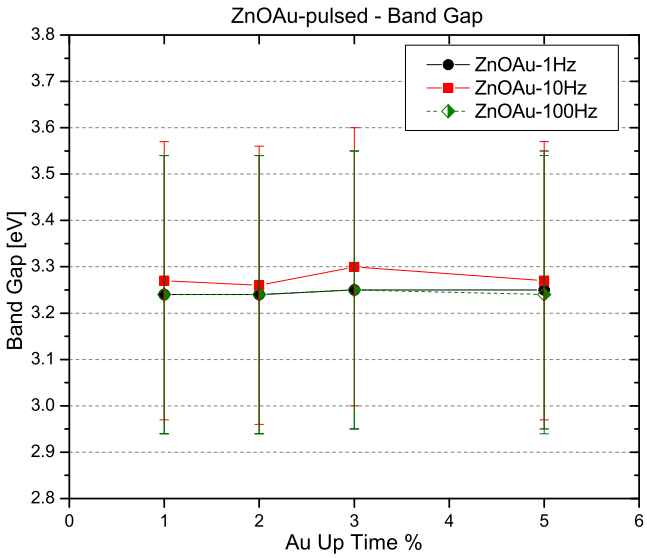

Figure 3.41: Band gap of series ZnOAu-pulsed

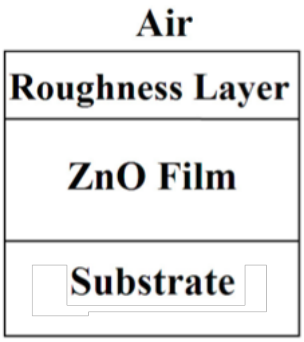

Figure 3.42: Multilayer model of the structure for ellipsometry fitting.

the fitted parameters summarized in Tab.3.4 and Fig.3.43. Of the three substrate types, SiO_2 substrates produced the worst results and will be omitted from this report. For the ZnO-0-100 series, measurements on Si substrates could not be carried out. n and k are reported for $\lambda = 632.8$ nm.

The thickness obtained with this fit is in good agreement with the results presented above, which points towards a good reliability of this fit (Fig.3.44). Roughness levels are on par with those visible in SEM images. The values we obtain for n are close to those reported in literature [100] and k is very close to zero, which shows that our films are in fact transparent. We also notice that n diminishes slightly with the increase of oxygen percentage in the plasma during deposition. This behaviour has already been noticed for Co_3O_4 [14] and could be related to the higher porosity observed in substrates grown with higher percentages of oxygen. It has been found that for SiO_2, porosity influences n: higher porosity corresponded to lower n [101].

In Tab.3.5 and Fig.3.45 we report the results of the fit for the ZnOAu-manual series.

In Tab.3.6 and Fig.3.46 and 3.47 we report the results of the fit for the ZnOAu-pulsed

Table 3.4: Ellipsometry results for the ZnO-0-100 series

Sample	Substrate	Model	MSE	n	k	Thickness [nm]	Roughness [nm]
ZnO-0	Glass	Abs. w/ BR	12.4	1.98	0.089	197.3 ± 0.6	10.0 ± 0.3
ZnO-10	Glass	Abs. w/ BR	4.3	1.95	0.016	157.0 ± 0.3	8.5 ± 0.2
ZnO-20	Glass	Abs. w/ BR	5.4	1.96	0.034	111.8 ± 0.2	6.9 ± 0.2
ZnO-30	Glass	Abs. w/ BR	3.0	1.94	0.007	99.5 ± 0.1	10.0 ± 0.1
ZnO-50	Glass	Abs. w/ BR	3.7	1.95	0.030	110.5 ± 0.1	16.7 ± 0.2
ZnO-70	Glass	Abs. w/ BR	2.1	1.94	0.010	82.9 ± 0.1	14.08 ± 0.07
ZnO-100	Glass	Abs. w/ BR	3.6	1.93	0.039	57.7 ± 0.3	4.7 ± 0.5

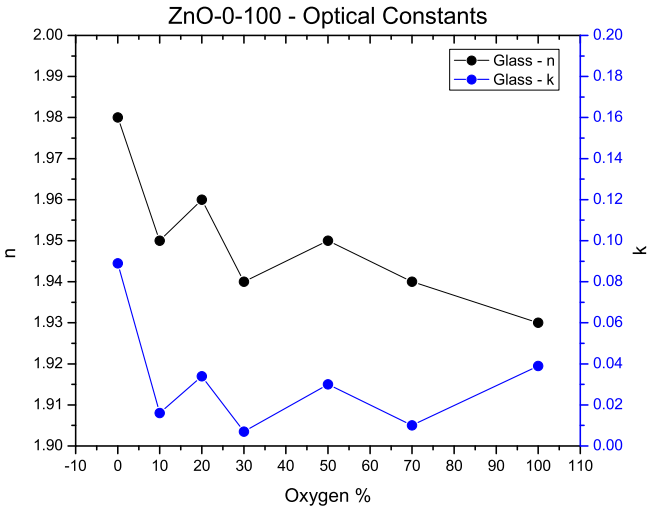

Figure 3.43: Ellipsometry results for the ZnO-0-100 series

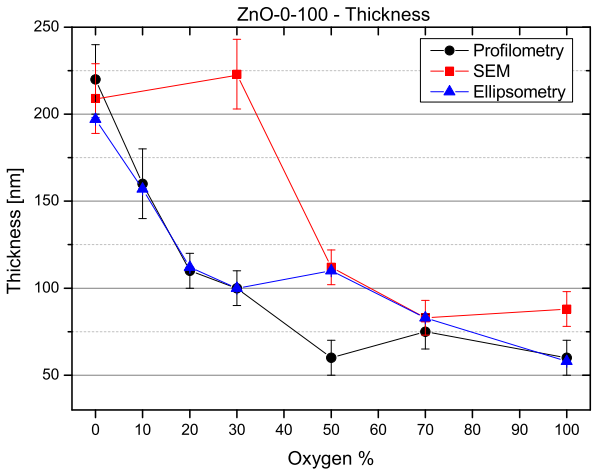

Figure 3.44: Comparison of thickness measured with different techniques

Table 3.5: Ellipsometry results for the ZnOAu-manual series

Sample	Substrate	Model	MSE	n	k	Thickness [nm]	Roughness [nm]
ZnOAu-10.6.54	Glass	Abs. w/ BR	2.4	2.13	0.13	213.6 ± 0.1	17.7 ± 0.1
ZnOAu-10.6.114	Glass	Abs. w/ BR	4.5	2.23	0.17	187.0 ± 0.3	12.4 ± 0.1
ZnOAu-5.6.54	Glass	Abs. w/ BR	14.3	2.18	0.04	146.0 ± 1.4	14 ± 1
ZnOAu-5.6.114	Glass	Abs. w/ BR	6.7	2.02	0.02	189.4 ± 0.4	8.9 ± 0.2
ZnOAu-5.3.147	Glass	Abs. w/ BR	6.5	1.99	0.01	181.0 ± 0.4	8.7 ± 0.2
ZnOAu-10.6.54	Si	Abs. no BR	2.1	2.17	0.10	222.9 ± 0.4	19.5 ± 0.1
ZnOAu-10.6.114	Si	Abs. no BR	2.8	1.85	0.08	202.6 ± 1.0	1.2 ± 0.5
ZnOAu-5.6.54	Si	Abs. no BR	1.3	2.02	0.12	258.6 ± 0.2	6.0 ± 0.1
ZnOAu-5.6.114	Si	Abs. no BR	6.3	2.23	0.01	180.9 ± 1.1	3.7 ± 0.3
ZnOAu-5.3.147	Si	Abs. no BR	2.8	1.85	0.08	202.6 ± 1.0	1.2 ± 0.5

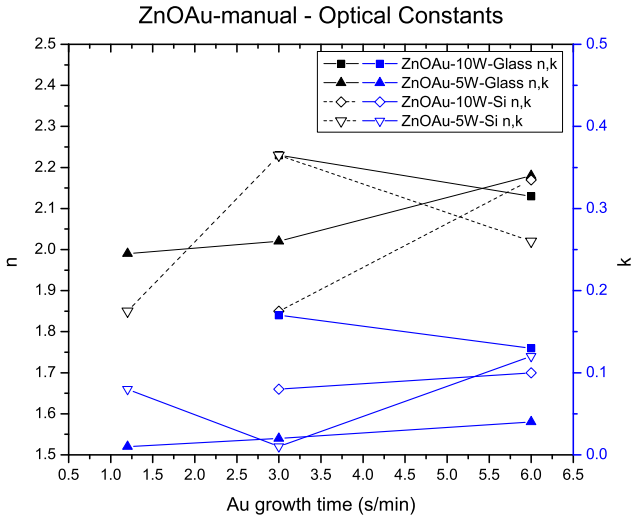

Figure 3.45: Ellipsometry results for the ZnOAu-manual series

series.

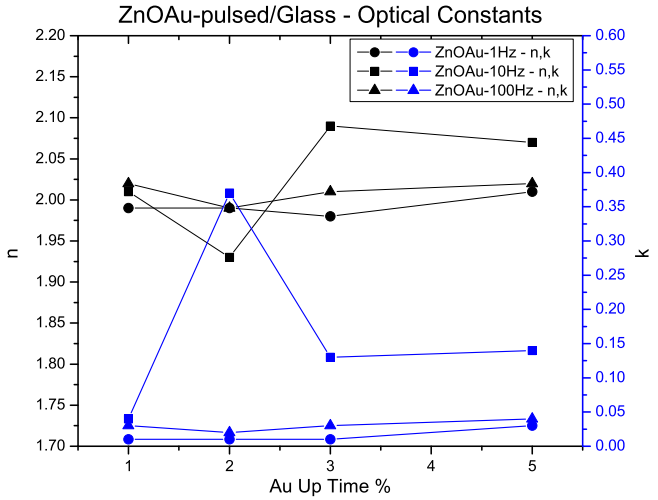

Figure 3.46: Ellipsometry results for the ZnOAu-pulsed series deposited on glass substrates

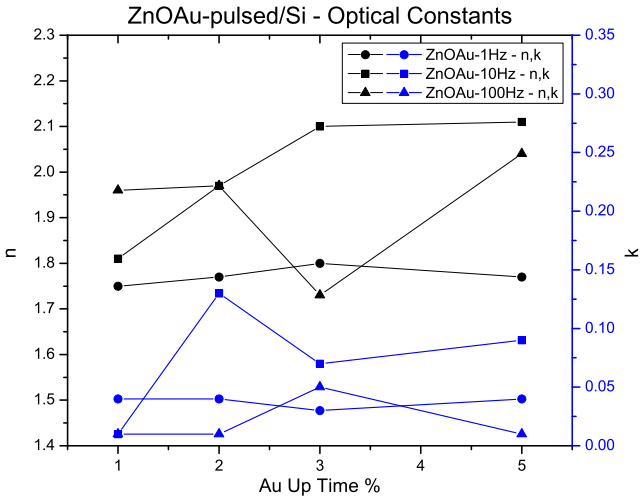

Figure 3.47: Ellipsometry results for the ZnOAu-pulsed series deposited on Si substrates

Values of n for the doped series result a little higher with respect to the undoped series, but still oscillate around $n \simeq 1.9 - 2.0$. The only difference is observed in the ZnOAu-1Hz series, where a significant drop to values of ~ 1.77 is registered on Si substrates, but not on glass. It should be noted, however that MSE for these fits is relatively high, so we should be careful when considering these results. From the values of n and k obtained for the Au doped series, no real trend emerges. The noticeable differences in values obtained from different substrates make us doubt the validity of this analysis.

Table 3.6: Ellipsometry results for the ZnOAu-pulsed series

Sample	Substrate	Model	MSE	n	k	Thickness [nm]	Roughness [nm]
ZnOAu-5.100.1	Glass	Abs. w/ BR	7.0	2.02	0.03	168.9 ± 0.4	5.6 ± 0.2
ZnOAu-5.100.2	Glass	Abs. w/ BR	5.8	1.99	0.02	166.8 ± 0.3	5.2 ± 0.1
ZnOAu-5.100.3	Glass	Abs. w/ BR	6.3	2.01	0.03	242.1 ± 0.4	4.2 ± 0.1
ZnOAu-5.100.5	Glass	Abs. w/ BR	7.1	2.02	0.04	165.3 ± 0.3	5.0 ± 0.2
ZnOAu-5.10.1	Glass	Abs. w/ BR	6.4	2.01	0.04	161.2 ± 0.3	3.1 ± 0.1
ZnOAu-5.10.2	Glass	Abs. w/ BR	7.5	1.93	0.37	143.0 ± 0.8	6.3 ± 0.7
ZnOAu-5.10.3	Glass	Abs. w/ BR	5.9	2.09	0.13	393.0 ± 0.5	19.4 ± 0.1
ZnOAu-5.10.5	Glass	Abs. w/ BR	3.9	2.07	0.14	264.5 ± 0.3	25.6 ± 0.1
ZnOAu-5.1.1	Glass	Abs. w/ BR	5.1	1.99	0.01	242.0 ± 0.4	5.0 ± 0.1
ZnOAu-5.1.2	Glass	Abs. w/ BR	5.6	1.99	0.01	241.9 ± 0.4	5.7 ± 0.2
ZnOAu-5.1.3	Glass	Abs. w/ BR	6.0	1.98	0.01	241.4 ± 0.5	5.0 ± 0.2
ZnOAu-5.1.5	Glass	Abs. w/ BR	7.6	2.01	0.03	233.8 ± 0.5	2.9 ± 0.2
ZnOAu-5.100.1	Si	Abs. no BR	11	1.96	0.01	200.1 ± 3.4	3.9 ± 0.9
ZnOAu-5.100.2	Si	Abs. no BR	14.5	1.97	0.01	206.1 ± 5.2	4.9 ± 1.5
ZnOAu-5.100.3	Si	Abs. no BR	15.9	1.73	0.05	307.8 ± 3.1	6.2 ± 0.9
ZnOAu-5.100.5	Si	Abs. no BR	7.6	2.04	0.01	189.0 ± 1.7	7.4 ± 0.5
ZnOAu-5.10.1	Si	Abs. no BR	8	1.81	0	210.1 ± 2.0	14.7 ± 0.6
ZnOAu-5.10.2	Si	Abs. no BR	1.9	1.97	0.13	333.2 ± 0.5	16.6 ± 0.2
ZnOAu-5.10.3	Si	Abs. no BR	3.1	2.1	0.07	393.4 ± 0.4	10.7 ± 0.1
ZnOAu-5.10.5	Si	Abs. no BR	4	2.11	0.09	293.9 ± 1.2	24.1 ± 0.4
ZnOAu-5.1.1	Si	Abs. no BR	14.2	1.75	0.04	313.9 ± 2.8	7.6 ± 0.8
ZnOAu-5.1.2	Si	Abs. no BR	13.2	1.77	0.04	311.2 ± 2.6	7.8 ± 0.7
ZnOAu-5.1.3	Si	Abs. no BR	15.8	1.8	0.03	299.2 ± 3.2	3.5 ± 0.9
ZnOAu-5.1.5	Si	Abs. no BR	16.4	1.77	0.04	304.5 ± 3.4	1.0 ± 1.0

3.5 Electrical Properties

Resistivity measurements were carried out with an *Ecopia* Hall effect station using the four-probe point method presented in 2.7. Ohmic SnIn contacts were soldered on our samples before deposition to facilitate measurements. Resistivity values obtained for the ZnO series are presented in Tab.3.7. Other oxides presented an increase in conductivity

Table 3.7: Resistivity of series ZnO

Sample	Resistivity [Ω·cm]
ZnO-0	770 ± 80
ZnO-10	$> 1.2 \pm 0.1 \cdot 10^6$
ZnO-20	$> 8.3 \pm 0.8 \cdot 10^5$
ZnO-30	$> 7.5 \pm 0.8 \cdot 10^5$
ZnO-50	$> 4.1 \pm 0.4 \cdot 10^5$
ZnO-70	$> 5.6 \pm 0.6 \cdot 10^5$
ZnO-100	$> 4.5 \pm 0.5 \cdot 10^5$

with the percentage of O_2 in the plasma during growth [11] [12] [13] [14]. What we found with ZnO is the opposite: the only sample that presented a measurable resistivity was the one grown with an atmosphere of pure argon ($\rho \simeq 770$ Ω·cm). We estimate a resistivity in the range of $\rho > 0.5 - 1.2 \cdot 10^6$ Ω· cm for the samples grown with oxygen. This was calculated from the knowledge that the maximum voltage drop our equipment can sustain is of 12V. We found that the lowest reliable current was of 5 nA, which yields a maximum detectable resistance of $2.4 \cdot 10^9$ Ω. In Tab.3.7 we reported the correspondent resistivity value after film thickness is taken into account. The lower limit of the resistivity decreases with higher P_{O_2} simply because the resistance limit is fixed while sample thickness is decreasing, limiting our investigating capabilities.

This results corroborate what was found in other experiments [6]. It was found that the resistivity underwent an abrupt transition from semiconducting ($\rho \sim 10^{-2}$ Ω cm) at low oxygen partial pressure to semi-insulating ($\rho \sim 10^6 - 10^8$ Ω cm) at higher P_{O_2}, starting approximately from $P_{O_2} \simeq 10^{-5}$ mbar. In the transition region the dependence of resistivity is exponential-like.

During our synthesis, we sputtered at low power (150 W) to mitigate potentially damaging bombardment of the growing ZnO film by energetic negative oxygen ions. For the same reasons, we also sputtered at a relatively high total gas pressure ~ 2 mbar, for which more energy dissipating collisions occur. These conditions did not allow us to investigate the transition region because our smallest step is of a 10% increase in oxygen partial pressure (see Tab:2.1), which under our conditions corresponds to $\sim 2 \cdot 10^{-3}$ mbar. In our case the sample grown with a complete Ar plasma is still found to have insulating properties. The easiest explanation is that the O_2 pressure was higher than 10^{-5} mbar at the moment of growth, but this possibility has to be ruled out since our base pressure has always been lower (more precisely, in the range of 10^{-7} mbar) than that and no oxygen was added to

the chamber before the synthesis. The low conductivity can be explained by poor crystal quality, as suggested by Xu et al. [99].

In undoped ZnO, excess, interstitial Zn ions [94] or oxygen vacancies [102] can contribute free electrons for electrical conduction. For growth above the critical $P_{O_2}(\simeq 10^{-5}$ mbar), we believe that films became close to stoichiometric with fewer structural defects and, consequently, much higher resistivity. [6] This possibility was investigated further by means of X-Ray photoelectron spectroscopy (see 3.3.1) and it was found that high resistivity samples corresponded to stoichiometric or close to stoichiometric ratios of O:Zn.

Sample	Resistivity [Ω·cm]
ZnOAu-10.6.54	31 ± 3
ZnOAu-10.6.114	0.089 ± 0.009
ZnOAu-5.6.54	1.1 ± 0.1
ZnOAu-5.6.114	7200 ± 700
ZnOAu-5.3.147	4600 ± 500

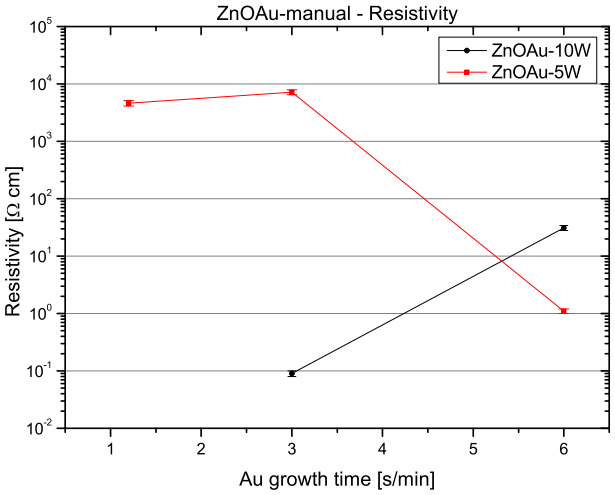

Figure 3.48: Resistivity of series ZnOAu-manual

Resistivity for the ZnOAu-manual series show unexpected results. The samples grown at high power (10 W) show very low resistivity but are also very opaque. Of the samples grown at low power only one has good conductibility, but is also the only one that is opaque. The two transparent samples of the series (ZnOAu-5.6.114 and ZnOAu-5.3.147) have a very distinct insulating property.

Samples were preserved in vacuum because it was found with other oxydes that air contamination influenced resistivity [13] This is even more important in our case, as we have found that the presence of oxygen inhibits conducibility of our samples in the case of pure ZnO. Oxygen contamination is unavoidable and could explain a little loss in conductivity as some of our samples were not measured immediately after the deposition. In fact, for some of the sample a long time had to be waited from deposition to measurements because of a failure in the Hall apparatus.

As we can see from the results presented in 3.49, resistivity varies a lot between samples grown with different Au pulsing frequency, and also inside the same-frequency series. This could be related to the higher disorder in the crystal structure [99] that characterizes, for example, the samples grown with 10 Hz Au frequency except for ZnOAu-10.3, which presents a much clearer diffraction pattern (see 3.16) and also has the best conductivity of the series despite not having the highest Au percentage. SEM observations made by Gao et al. [103] suggest that the conductivity of the films may be affected by their microstructure.

Sample	Resistivity [Ω·cm]
ZnOAu-100.1	130 ± 10
ZnOAu-100.2	380 ± 40
ZnOAu-100.3	4.6 ± 0.5
ZnOAu-100.5	320 ± 30
ZnOAu-10.1	560 ± 60
ZnOAu-10.2	7600 ± 800
ZnOAu-10.3	140 ± 10
ZnOAu-10.5	6200 ± 600
ZnOAu-1.1	14 ± 1
ZnOAu-1.2	16 ± 2
ZnOAu-1.3	1.5 ± 0.2
ZnOAu-1.5	1.4 ± 0.1

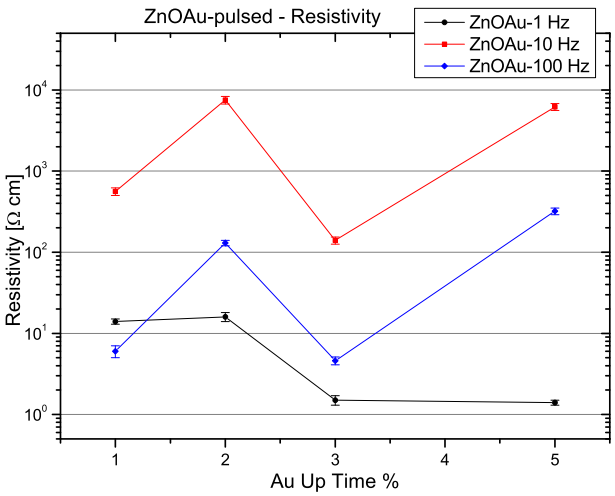

Figure 3.49: Resistivity of series ZnOAu-pulsed

In particular, they observe that grains that grains that grow along the *c*-axis with a not pronounced columnar structure, diverse orientations and denser feature seem helpful to electron conduction.

Contrary to expectations, samples that present Au through chemical analysis do not have the best conductivity, especially for the ZnOAu-pulsed series. Of these only series that shows gold deposition is that grown at 10 Hz, but these samples have some of the highest resistivities measured. Surprisingly, the most conductive samples are those from the ZnOAu-1 series. If we assume that some gold has in fact been absorbed in the crystal structure, it would seem that a low frequency favours conductivity. However neither XPS nor x-ray fluorescence revealed any gold in these samples, so Au concentration should be less than the parts per thousand range. Incidentally, these samples also show very good transparency so there is a chance that no gold was deposited at all and these samples are just better ordered ZnO films and for this reason show good conductivity. However, no sign of this comes from SEM imaging or XRD analysis, so any assertion would be far-fetched.

Chapter 4

Conclusions

We presented a preliminary work of growth and characterisation of thin ZnO films grown by rf magnetron sputtering and doped with Au nanoparticles. Three main series of samples were made: in the first only ZnO was deposited with different oxygen content in the plasma (serie ZnO-0-100), the second and third ones used co-sputtering techniques to embed gold nanoparticles in the ZnO film. These two series employed different methods to limit the exposition to the Au flux. In the first of the two a shutter was used to prevent the Au flux from reaching the substrates (series ZnOAu-manual), while in the second a pulsed source was used to automatically turn on and off the magnetron where the gold target was installed (series ZnOAu-pulsed: ZnOAu-100Hz, ZnOAu-10Hz, ZnOAu-1Hz).

Samples were grown in a high vacuum chamber at a working pressure of $\sim 10^{-}2$ mbar after a base pressure of $\sim 10^{-}7$ mbar had been reached to ensure the purity of the conditions during deposition. Low magnetron power was used to to mitigate potentially damaging bombardment of the growing ZnO film by energetic negative oxygen ions. Films were deposited on substrates of crystalline Si, anodic aluminium oxide membranes, two types of glass with different thickness (Menzel-gläser coverglass and standard microscope slides) and SiO_2 wavers.

The thickness was measured with two different techniques: a stylus profiler and SEM imaging. The results obtained with the two methods were in good agreement and showed a thickness that ranged within $\sim 50 - 400$ nm. One of the effects of oxygen presence in the plasma was found to be the reduction of the film thickness. This was explained with the lower sputtering efficiency that the lighter oxygen ions imply with respect to the heavier Ar ones. This result is shared with other oxides like NiO and Co_3O_4 [11] [12] [13] [14].

With (FE)SEM imaging, it was also observed that the presence of oxygen in the plasma produces a considerable grain refinement and a reduction in grain size. The columnar feature of the structure was explained with the Thornton model which describes how the structure of the coating changes with temperature and pressure. In particular, for low homologous temperatures the adatom mobility is low and the growth is dominated by the shadowing effect and by the geometry of the system. The resulting structure is columnar with grain boundaries replaced by walls of low density or voided material. The off-axis

geometry of our magnetrons favours shadowing and *c*-axis structures, creating growth velocity anisotropies that lead to competition of grains during thickening and finally to textured crystals. A good explanation of the microscopic process behind this comes from Van der Drift's model. This models also explains efficiently the growth of ZnO on porous AAM.

The crystalline structure was investigated with x-ray diffraction, which showed that all our samples have a preferential orientation along the (0 0 2) axis. The absence of oxygen in the plasma allows for a more diverse crystalline population. This result is however in contrast with what has been found in other researches [85]. The characteristic diffraction pattern of metallic gold was not observed, which means that gold particles have very small sizes (less than $\sim$ 1 nm). Overall, Au doping seemed to make the crystalline structure less ordered. Analysis of the crystalline domain size was carried out with the Scherrer method. The average domain size is considerably smaller than the average grain size, which reinforces the statement that our films have polycrystalline features. The precision of our measures do not allow us to make any definitive statement on the variation of the domain size with deposition conditions. No significative dependence was found between grain size and Au concentration.

Chemical analysis was carried out with XPS and x-ray fluorescence. With the former it was found that Zn appears in the crystalline structure in the form of Zn^{2+}, while gold is found as a Au^{1+} ion. When oxygen is present in the plasma, even at very low relative pressure, ZnO is found to be stoichiometric and is reported to lose is conductibility characteristics [6]. Of the Au doped samples, it was possible to detect gold nanoparticles only on three of the samples grown with the pulsed deposition method. All samples from the ZnOAu-manual series presented gold nanoparticles. Chemical analysis made with x-ray fluorescence confirms this finding.

All samples where gold is detected show poor transmittance in the visible region, while all others have a transmittance of $\sim$ 80%. In the near infrared region a significant trend is observed for the ZnO-0-100 series. Samples grown with higher oxygen percentage in the plasma show a much better transmittance, going from $\sim$ 5% to $\sim$ 40%. The band gap was also measured yielding results that are in general agreement with what is found in the literature for ZnO, placing it at $\sim$ 3.24 eV. We also notice a small decrease in the band gap with higher oxygen percentages during deposition: the measured gap of 3.28 eV for 0% oxygen percentage becomes 3.23 eV for the 100% oxygen plasma. However, we could not confirm the proposition found in other researches that Au doping reduces the gap [99]. We observed no significative difference from the undoped samples, except for the ZnOAu-10Hz series, which shows a higher gap.

Ellipsometry measures on glass and Si were used to estimate the refraction and extinction indexes. The best model for fitting the pattern was found to be that of an absorbing film with surface roughness. Results obtained from the two substrates are not in good agreement, especially for the ZnOAu-100Hz series. n is found to be in the range 1.7-2.2, while k is found to be very small (< 0.1), confirming the generally good transparence of

the films. Film thickness calculated with this model yields results comparable to those obtained with other methods, although there are some variations. The average surface roughness is 9 nm, which is in agreement with what can be observed with SEM imaging. Overall, ellipsometry measurements can be considered reliable only for the ZnO-0-100 series, where a distinct trend is observed. With the increasing percentage of oxygen in the plasma during deposition, n diminishes from an initial value of 1.98 to 1.93. This trend is very interesting and encourages further research on the matter.

XPS analysis of the valence band of our samples predicts that samples where gold is found should be more conductive, but our electrical measurements do not show this. The low conductibility of our samples can be explained by the low order in the crystalline structure, but no satisfactory explanation was found for the good conductivity of other samples, especially if we compare their various analysis with those of other samples that show poor electrical properties.

In conclusion, we can say that we have established a method for the creation of thin ZnO films, but further research is needed to optimise the growth procedure in order to synthetize Au doped ZnO films that preserve the characterizes transparency of zinc oxide. Interesting optical features are observed in ZnO films when oxygen is present in the chamber during deposition and suggest further study of the matter.

Bibliography

[1] Gregory N. Parsons, Chien-Sheng Yang, Tonya M. Klein, and Laura Smith. Reaction processes for low temperature plasma enhanced deposition of hydrogenated amorphous silicon thin film transistors on transparent plastic substrates. In *Symposium A Ð Amorphous and Microcrystalline Silicon Technology 1998*, volume 507 of *MRS Proceedings*, 1 1998.

[2] AR Brown, CP Jarrett, DM De Leeuw, and M Matters. Field-effect transistors made from solution-processed organic semiconductors. *Synthetic metals*, 88(1):37–55, 1997.

[3] HE Katz. Organic molecular solids as thin film transistorsemiconductors. *J. Mater. Chem.*, 7(3):369–376, 1997.

[4] Zhenan Bao, Andrew J Lovinger, and Janelle Brown. New air-stable n-channel organic thin film transistors. *Journal of the American Chemical Society*, 120(1):207–208, 1998.

[5] Yutaka Ohya, Tsukasa Niwa, Takayuki Ban, and Yasutaka Takahashi. Thin film transistor of zno fabricated by chemical solution deposition. *Japanese Journal of Applied Physics*, 40:297, 2001.

[6] PF Carcia, RS McLean, MH Reilly, and G Nunes Jr. Transparent zno thin-film transistor fabricated by rf magnetron sputtering. *Applied Physics Letters*, 82(7):1117–1119, 2003.

[7] P. P. Edwards, A. Porch, M. O. Jones, D. V. Morgan, and R. M. Perks. Basic materials physics of transparent conducting oxides. *Dalton Trans.*, pages 2995–3002, 2004.

[8] Klaus Ellmer and Rainald Mientus. Carrier transport in polycrystalline ito and zno: Al ii: the influence of grain barriers and boundaries. *Thin Solid Films*, 516(17):5829–5835, 2008.

[9] Klaus Ellmer, Andreas Klein, and Bernd Rech. *Transparent conductive zinc oxide: basics and applications in thin film solar cells*, volume 104. Springer, 2007.

[10] K. J. Saji, R. Manoj, R. S. Ajimsha, and M. K. Jayaraj. Growth of zinc oxide thin films for optoelectronic application by pulsed laser deposition. *Proc. SPIE*, 6286:62860D–62860D–12, 2006.

[11] RJO Mossanek, G Domínguez-Cañizares, A Gutiérrez, M Abbate, D Díaz-Fernández, and L Soriano. Effects of ni vacancies and crystallite size on the o 1s and ni 2p x-ray absorption spectra of nanocrystalline nio. *Journal of Physics: Condensed Matter*, 25(49):495506, 2013.

[12] A Gutiérrez, G Domínguez-Cañizares, José Antonio Jiménez, I Preda, D Díaz-Fernández, Félix Jiménez-Villacorta, GR Castro, Jesús Chaboy, and L Soriano. Hexagonally-arranged-nanoporous and continuous nio films with varying electrical conductivity. *Applied Surface Science*, 276:832–837, 2013.

[13] G Domìnguez-Cañizares. *Nanostructured Nickel Oxide thin films grown by Reactive RF Magnetron Sputtering*. PhD thesis, Universidad Autònoma de Madrid, 2014.

[14] Carlos Morales Sànchez. Characterization of ultra-thin films of cobalt oxide grown with rf magnetron sputtering. Bachelor Thesis in Advanced Materials and Nanotechnology, Universidad Autònoma de Madrid, 2014.

[15] Lori E Greene, Matt Law, Joshua Goldberger, Franklin Kim, Justin C Johnson, Yanfeng Zhang, Richard J Saykally, and Peidong Yang. Low-temperature wafer-scale production of zno nanowire arrays. *Angewandte Chemie International Edition*, 42(26):3031–3034, 2003.

[16] RJ Lad, PD Funkenbusch, and CR Aita. Postdeposition annealing behavior of rf sputtered zno films. *Journal of Vacuum Science and Technology*, 17(4):808–811, 1980.

[17] MK Ryu, SH Lee, MS Jang, GN Panin, and TW Kang. Postgrowth annealing effect on structural and optical properties of zno films grown on gaas substrates by the radio frequency magnetron sputtering technique. *Journal of applied physics*, 92(1):154–158, 2002.

[18] Kenichi Ozaki and Manabu Gomi. Strong ultraviolet photoluminescence in polycrystalline zno sputtered films. *Japanese journal of applied physics*, 41(9R):5614, 2002.

[19] U Ozgur, A Teke, C Liu, S-J Cho, H Morkoc, and HO Everitt. Stimulated emission and time-resolved photoluminescence in rf-sputtered zno thin films. *Applied physics letters*, 84(17):3223–3225, 2004.

[20] RBM Cross, MM De Souza, and EM Sankara Narayanan. A low temperature combination method for the production of zno nanowires. *Nanotechnology*, 16(10):2188, 2005.

[21] Hadis Morkoç and Ümit Özgür. *Zinc oxide: fundamentals, materials and device technology*. John Wiley & Sons, 2008.

[22] K Ellmer, K Diesner, R Wendt, and S Fiechter. Relations between texture and electrical parameters of thin polycrystalline zinc oxide films. *Solid State Phenomena*, 51:541–546, 1996.

[23] Kazunori Minegishi, Yasushi Koiwai, Yukinobu Kikuchi, Koji Yano, Masanobu Kasuga, and Azuma Shimizu. Growth of p-type zinc oxide films by chemical vapor deposition. *Japanese Journal of Applied Physics*, 36(11A):L1453, 1997.

[24] YR Ryu, S Zhu, David C Look, JM Wrobel, HM Jeong, and HW White. Synthesis of p-type zno films. *Journal of Crystal Growth*, 216(1):330–334, 2000.

[25] David C Look, DC Reynolds, CW Litton, RL Jones, DB Eason, and G Cantwell. Characterization of homoepitaxial p-type zno grown by molecular beam epitaxy. *Applied physics letters*, 81(10):1830–1832, 2002.

[26] Kyoung-Kook Kim, Hyun-Sik Kim, Dae-Kue Hwang, Jae-Hong Lim, and Seong-Ju Park. Realization of p-type zno thin films via phosphorus doping and thermal activation of the dopant. *Applied physics letters*, 83(1):63–65, 2003.

[27] M Joseph, H Tabata, H Saeki, K Ueda, and T Kawai. Fabrication of the low-resistive p-type zno by codoping method. *Physica B: Condensed Matter*, 302:140–148, 2001.

[28] Xin-Li Guo, Hitoshi Tabata, and Tomoji Kawai. Pulsed laser reactive deposition of p-type zno film enhanced by an electron cyclotron resonance source. *Journal of Crystal Growth*, 223(1):135–139, 2001.

[29] Teresa M Barnes, Kyle Olson, and Colin A Wolden. On the formation and stability of p-type conductivity in nitrogen-doped zinc oxide. *Applied Physics Letters*, 86(11):112112–112112, 2005.

[30] PJ Kelly and RD Arnell. Magnetron sputtering: a review of recent developments and applications. *Vacuum*, 56(3):159–172, 2000.

[31] André Anders. Metal plasmas for the fabrication of nanostructures. *Journal of Physics D: Applied Physics*, 40(8):2272, 2007.

[32] Chi Kwan Lau, Shiban K Tiku, and KM Lakin. Growth of epitaxial zno thin films by organometallic chemical vapor deposition. *Journal of The Electrochemical Society*, 127(8):1843–1847, 1980.

[33] SK Tiku, CK Lau, and KM Lakin. Chemical vapor deposition of zno epitaxial films on sapphire. *Applied Physics Letters*, 36(4):318–320, 1980.

[34] Masanobu Kasuga and Masami Mochizuki. Orientation relationships of zinc oxide on sapphire in heteroepitaxial chemical vapor deposition. *Journal of Crystal Growth*, 54(2):185–194, 1981.

[35] V Srikant, Valter Sergo, and David R Clarke. Epitaxial aluminum-doped zinc oxide thin films on sapphire: I, effect of substrate orientation. *Journal of the American Ceramic Society*, 78(7):1931–1934, 1995.

[36] Kyoung-Kook Kim, Jae-Hoon Song, Hyung-Jin Jung, Won-Kook Choi, Seong-Ju Park, and Jong-Han Song. The grain size effects on the photoluminescence of zno/α-al2o3 grown by radio-frequency magnetron sputtering. *Journal of Applied Physics*, 87(7):3573–3575, 2000.

[37] JL Vossen. Transparent conducting films. *Physics of Thin Films*, 9(1), 1977.

[38] Donald M Mattox. *Handbook of physical vapor deposition (PVD) processing*. William Andrew, 2010.

[39] Milton Ohring. *Materials science of thin films*. Academic press, 2001.

[40] T Muramoto and Y Yamamura. {MD} simulation of cluster ejection due to sputtering by polyatomic projectiles. *Applied Surface Science*, 203Ð204(0):143 – 147, 2003. Secondary ion mass spectrometry {SIMS} {XIII}.

[41] Rainer Behrisch and Wolfgang Eckstein. *Sputtering by particle bombardment: experiments and computer calculations from threshold to MeV energies*, volume 110. Springer, 2007.

[42] Th J Colla, HM Urbassek, A Wucher, C Staudt, R Heinrich, BJ Garrison, C Dandachi, and G Betz. Experiment and simulation of cluster emission from 5 kev ar-> cu. *Nuclear Instruments and Methods in Physics Research Section B: Beam Interactions with Materials and Atoms*, 143(3):284–297, 1998.

[43] John A Thornton. The microstructure of sputter-deposited coatings. *Journal of Vacuum Science & Technology A*, 4(6):3059–3065, 1986.

[44] I Petrov, PB Barna, Lars Hultman, and JE Greene. Microstructural evolution during film growth. *Journal of Vacuum Science & Technology A*, 21(5):S117–S128, 2003.

[45] CV Thompson. Structure evolution during processing of polycrystalline films. *Annual review of materials science*, 30(1):159–190, 2000.

[46] GS Bales and A Zangwill. Macroscopic model for columnar growth of amorphous films by sputter deposition. *Journal of Vacuum Science & Technology A*, 9(1):145–149, 1991.

[47] BA Movchan and AV Demchishin. Structure and properties of thick condensates of nickel, titanium, tungsten, aluminum oxides, and zirconium dioxide in vacuum. *Fiz. Metal. Metalloved. 28: 653-60 (Oct 1969).*, 1969.

[48] John A Thornton. Influence of apparatus geometry and deposition conditions on the structure and topography of thick sputtered coatings. *Journal of Vacuum Science & Technology*, 11(4):666–670, 1974.

[49] A.M. Brown and M.F. Ashby. Correlations for diffusion constants. *Acta Metallurgica*, 28(8):1085 – 1101, 1980.

[50] SM Rossnagel, I Yang, and JJ Cuomo. Compositional changes during magnetron sputtering of alloys. *Thin Solid Films*, 199(1):59–69, 1991.

[51] John A Thornton. High rate thick film growth. *Annual review of materials science*, 7(1):239–260, 1977.

[52] HJ Leamy and AG Dirks. Microstructure and magnetism in amorphous rare-earth–transition-metal thin films. i. microstructure. *Journal of Applied Physics*, 49(6):3430–3438, 1978.

[53] Uwe Kreibig and Michael Vollmer. *Optical properties of metal clusters*. Springer-Verlag, 1995.

[54] Matthew Rycenga, Claire M Cobley, Jie Zeng, Weiyang Li, Christine H Moran, Qiang Zhang, Dong Qin, and Younan Xia. Controlling the synthesis and assembly of silver nanostructures for plasmonic applications. *Chemical reviews*, 111(6):3669–3712, 2011.

[55] Paul Mulvaney. Surface plasmon spectroscopy of nanosized metal particles. *Langmuir*, 12(3):788–800, 1996.

[56] R. Griffith Freeman, Katherine C. Grabar, Keith J. Allison, Robin M. Bright, Jennifer A. Davis, Andrea P. Guthrie, Michael B. Hommer, Michael A. Jackson, Patrick C. Smith, Daniel G. Walter, and Michael J. Natan. Self-assembled metal colloid monolayers: An approach to sers substrates. *Science*, 267(5204):1629–1632, 1995.

[57] M. Kahl, E. Voges, S. Kostrewa, C. Viets, and W. Hill. Periodically structured metallic substrates for {SERS}. *Sensors and Actuators B: Chemical*, 51(1Ð3):285 – 291, 1998.

[58] Yvo Dirix, Cees Bastiaansen, Walter Caseri, and Paul Smith. Oriented pearl-necklace arrays of metallic nanoparticles in polymers: A new route toward polarization-dependent color filters. *Advanced Materials*, 11(3):223–227, 1999.

[59] Andrea Alù, Michael E Young, and Nader Engheta. Design of nanofilters for optical nanocircuits. *Physical Review B*, 77(14):144107, 2008.

[60] S. A. Maier, M. L. Brongersma, P. G. Kik, S. Meltzer, A. A. G. Requicha, and H. A. Atwater. Plasmonics - a route to nanoscale optical devices. *Advanced Materials*, 13(19):1501–1505, 2001.

[61] Stefan A Maier, Pieter G Kik, Harry A Atwater, Sheffer Meltzer, Elad Harel, Bruce E Koel, and Ari AG Requicha. Local detection of electromagnetic energy transport below the diffraction limit in metal nanoparticle plasmon waveguides. *Nature materials*, 2(4):229–232, 2003.

[62] Amanda J Haes and Richard P Van Duyne. A nanoscale optical biosensor: sensitivity and selectivity of an approach based on the localized surface plasmon resonance spectroscopy of triangular silver nanoparticles. *Journal of the American Chemical Society*, 124(35):10596–10604, 2002.

[63] K. Matsubara, P. Fons, K. Iwata, A. Yamada, K. Sakurai, H. Tampo, and S. Niki. Zno transparent conducting films deposited by pulsed laser deposition for solar cell applications. *Thin Solid Films*, 431Ð432:369 – 372, 2003. Proceedings of Symposium B, Thin Film Chalcogenide Photovoltaic Materials, E-MRS Spring Meeting.

[64] R Alvarez, JM García-Martín, M Macías-Montero, L Gonzalez-Garcia, JC González, V Rico, J Perlich, J Cotrino, AR González-Elipe, and A Palmero. Growth regimes of porous gold thin films deposited by magnetron sputtering at oblique incidence: from compact to columnar microstructures. *Nanotechnology*, 24(4):045604, 2013.

[65] Kiyotaka Wasa, Makoto Kitabatake, and Hideaki Adachi. *Thin film materials technology: sputtering of control compound materials*. Springer, 2004.

[66] Semicore Equipment Inc. Sputtering yield rates.

[67] Yong-Nian Xu and WY Ching. Electronic, optical, and structural properties of some wurtzite crystals. *Physical Review B*, 48(7):4335, 1993.

[68] Kuniaki Kiharai and Gabrielle Donnay. Anharmonic thermal vibrations in zno. *Canadian Mineralogist*, 23:647–654, 1985.

[69] In-Kook Suh, H Ohta, and Y Waseda. High-temperature thermal expansion of six metallic elements measured by dilatation method and x-ray diffraction. *Journal of materials science*, 23(2):757–760, 1988.

[70] BD Cullity. *Elements of X-Ray Diffraction*. Addison-Wesley Pub. Co., 1978.

[71] ChangChun Chen, Ping Liu, and ChunHua Lu. Synthesis and characterization of nano-sized zno powders by direct precipitation method. *Chemical Engineering Journal*, 144(3):509 – 513, 2008.

[72] J. I. Langford and A. J. C. Wilson. Scherrer after sixty years: A survey and some new results in the determination of crystallite size. *Journal of Applied Crystallography*, 11(2):102–113, Apr 1978.

[73] D Dìaz Fernàndez. *Study of the Growth and Interaction of Cobalt Oxides on HOPG and other Oxides*. PhD thesis, Universidad Autònoma de Madrid, 2014.

[74] Miquel Salmeron and R Schlögl. Ambient pressure photoelectron spectroscopy: A new tool for surface science and nanotechnology. *Surface Science Reports*, 63(4):169–199, 2008.

[75] A Jürgensen, N Esser, and R Hergenröder. Near ambient pressure xps with a conventional x-ray source. *Surface and Interface Analysis*, 44(8):1100–1103, 2012.

[76] John F Moulder, William F Stickle, Peter E Sobol, and Kenneth D Bomben. *Handbook of X-ray photoelectron spectroscopy*, volume 40. Perkin Elmer Eden Prairie, MN, 1992.

[77] J Tauc, R Grigorovici, and A Vancu. Optical properties and electronic structure of amorphous germanium. *physica status solidi (b)*, 15(2):627–637, 1966.

[78] Olaf Stenzel. *The physics of thin film optical spectra: an introduction*, volume 44. Springer, 2005.

[79] Jacques I Pankove. *Optical processes in semiconductors*. Courier Dover Publications, 2012.

[80] LJ Van der Pauw. Determination of resistivity tensor and hall tensor of anisotropic conductors. *Philips Research Reports*, 16:187–195, 1961.

[81] Simon M Sze and Kwok K Ng. *Physics of semiconductor devices*. John Wiley & Sons, 2006.

[82] N Koteeswara Reddy, Q Ahsanulhaq, JH Kim, M Devika, and YB Hahn. Selection of non-alloyed ohmic contacts for zno nanostructure based devices. *Nanotechnology*, 18(44):445710, 2007.

[83] HW Ryu, GP Choi, WS Lee, and JS Park. Preferred orientations of nio thin films prepared by rf magnetron sputtering. *Journal of materials science*, 39(13):4375–4377, 2004.

[84] Taylor Hobson Ltd. Taylor hobson ltd history.

[85] Klaus Ellmer. Magnetron sputtering of transparent conductive zinc oxide: relation between the sputtering parameters and the electronic properties. *Journal of Physics D: Applied Physics*, 33(4):R17, 2000.

[86] A Van der Drift. Evolutionary selection, a principle governing growth orientation in vapour-deposited layers. *Philips Res. Rep*, 22(3):267–88, 1967.

[87] Hanno zur Loye. X-ray diffraction. Lesson, 2013.

[88] Vitalij Pecharsky and Peter Zavalij. *Fundamentals of powder diffraction and structural characterization of materials*. Springer, 2008.

[89] G Domínguez-Cañizares, A Gutiérrez, Jesús Chaboy, D Díaz-Fernández, GR Castro, and L Soriano. Effects of grain refinement and disorder on the electronic properties of nanocrystalline nio. *Journal of Materials Science*, 49(7):2773–2780, 2014.

[90] Sami Mahmood.

[91] KL Smith and KM Black. Characterization of the treated surfaces of silicon alloyed pyrolytic carbon and sic. *Journal of Vacuum Science & Technology A*, 2(2):744–747, 1984.

[92] Alexander V. Naumkin, Anna Kraut-Vass, Stephen W. Gaarenstroom, and Cedric J. Powell. Nist x-ray photoelectron spectroscopy database.

[93] VI Nefedov, Ya V Salyn, G Leonhardt, and R Scheibe. A comparison of different spectrometers and charge corrections used in x-ray photoelectron spectroscopy. *Journal of Electron Spectroscopy and Related Phenomena*, 10(2):121–124, 1977.

[94] RA Swalin. *Thermodynamics of Solids*. Wiley, New York, 1972.

[95] Martin P Seah and David Briggs. *Practical Surface Analysis: Auger and X-ray Photoelectron Spectroscopy*. John Wiley & Sons, 1990.

[96] Eric Irissou, Marie-Chantal Denis, Mohammed Chaker, and Daniel Guay. Gold oxide thin film grown by pulsed laser deposition in an {O2} atmosphere. *Thin Solid Films*, 472(1Ð2):49 – 57, 2005.

[97] D. W. Langer and C. J. Vesely. Electronic core levels of zinc chalcogenides. *Phys. Rev. B*, 2:4885–4892, Dec 1970.

[98] Anuradha Patra. *Studies on Au nanoparticles embedded ZnO thin films and ZnO covered Ag nanoparticles thin films*. PhD thesis, Indian Institute of Technology Madras, 2011.

[99] Y Xu, B Yao, YF Li, ZH Ding, JC Li, HZ Wang, ZZ Zhang, LG Zhang, HF Zhao, and DZ Shen. Chemical states of gold doped in zno films and its effect on electrical and optical properties. *Journal of Alloys and Compounds*, 585:479–484, 2014.

[100] R Ondo-Ndong, F Pascal-Delannoy, A Boyer, A Giani, and A Foucaran. Structural properties of zinc oxide thin films prepared by r.f. magnetron sputtering. *Materials Science and Engineering: B*, 97(1):68 – 73, 2003.

[101] E.V. Astrova and V.A. Tolmachev. Effective refractive index and composition of oxidized porous silicon films. *Materials Science and Engineering: B*, 69Ð70(0):142 – 148, 2000.

[102] K-S Weißenrieder and J Müller. Conductivity model for sputtered zno-thin film gas sensors. *Thin Solid Films*, 300(1):30–41, 1997.

[103] Wei Gao and Zhengwei Li. Zno thin films produced by magnetron sputtering. *Ceramics International*, 30(7):1155 – 1159, 2004. 3rd Asian Meeting on Electroceramics.